Modelling and Fabrication of Proteotronic Devices for Various Electrical and Optical Applications

Thesis submitted for the Degree of Doctor of Philosophy (Science)
Of
Jadavpur University

by

Shrabani Guhathakurata

Condensed Matter Physics Research Centre
Department of Physics
Jadavpur University
Kolkata – 700 032

2023

I dedicate this thesis to my loving parents

Mr. Ashoke Guhathakurata

&

Mrs. Bharati Guhathakurata

who inspired me to pursue my dreams.

Declaration by the Author

I do hereby declare that the work embodied in this thesis entitled "**Modelling and Fabrication of Proteotronic Devices for Various Electrical and Optical Applications**", which is being submitted for the Degree of Doctor of Philosophy (Science), is my own work, and that, to the best of my knowledge and belief, neither the thesis nor any part thereof has been accepted for the award of any other degree in this university or in other institutes, except where true acknowledgement has been made.
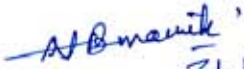
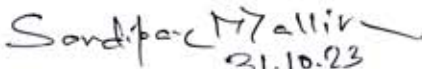Date: (Shrabani Guhathakurata)

Place:

CERTIFICATE FROM THE SUPERVISORS

This is to certify that the thesis entitled "**Modelling and Fabrication of Proteotronic Devices for Various Electrical and Optical Applications**", submitted by Smt. Shrabani Guhathakurata who got her name registered on 17th March, 2021 for the award of PhD (Science) Degree of Jadavpur University, is absolutely based upon her own work under the supervision of **Prof. Nabin Baran Manik** (Supervisor) and **Dr. Sandipan Mallik** (Co-supervisor), and that neither this thesis nor any part of it has been submitted for either any degree/diploma or any other academic award anywhere before.

ABmanik
31.10.2023

Prof. Nabin Baran Manik (Supervisor)
Professor,
Condensed Matter Physics Research Centre
Department of Physics
Jadavpur University
Kolkata – 700032

Dr. NABIN BARAN MANIK
Professor
Department of Physics
Jadavpur University
Kolkata - 700 032
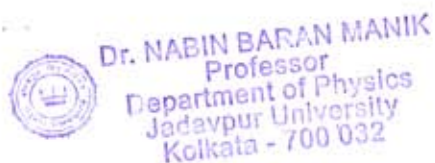
Sandipan Mallik
31.10.23

Dr. Sandipan Mallik (Co-Supervisor)
Associate Professor,
Department of Electronics &
Communication Engineering (ECE)
NIST Institute of Science and Technology
(Autonomous), Berhampur,
Odisha, India 761008

Associate Professor (ECE) and Head of Research
NIST (Autonomous), Institute-Park
Pallur Hills Berhampur, Odisa, INDIA-761008

<u>Acknowledgement</u>

List of Figures

List of Tables

Abbreviations

List of Acronyms (unless otherwise specified)

AC	Alternating Current
AFM	Atomic Force Microscope
Al	Aluminium
ASTM	American Society for Testing and Materials
Au	Gold
BPS	Biopolymer substrate
BSA	Bovine Serum Albumin
CV	Capacitance Voltage
CVS	Constant Voltage Stressing
DC	Direct Current
DC	Drop casting
DF	Dissipation Factor
DI	De-ionised
DIC	Dip coating
ESR	Equivalent Series Resistance
FESEM	Field Emission Scanning Electron Microscope
FTIR-ATR	Fourier Transform Infrared Attenuated Total Reflectance Spectroscopy
HCl	Hydrogen Chloride
HOMO	Highest occupied molecular orbital
HRS	High resistance state
HV	High Voltage
IDEs	Interdigitated electrodes
IDL	Ionic double layers
IETS	Inelastic Electron Tunnelling Spectroscopy
ITO	Indium Tin Oxide
ITRS	The International Technology Roadmap for Semiconductors
IV	Current Voltage
LASER	Light amplification by simulated emission of radiation
LRS	Low resistance state

LUMO	Lowest unoccupied molecular orbital
LV	Low Voltage
MIM	Metal-Insulator-Metal
NaOH	Sodium Hydroxide
PET	Polyethylene terephthalate
PF	Poole–Frenkel
PL	Photoluminescence
PoP	Pencil writing on Paper
Ppm	Parts per million
Pt	Platinum
Q	Quality Factor
RS	Resistive switching
SC	Spin coating
SCLC	Space charge limited current
SPRC	Spray coating
SR	Schottky–Richardson
TC-SCLC	Trap-controlled space-charge-limited current
UTM	Universal testing machine
UV-Vis	Ultraviolet-Visible
VCC	Voltage coefficients of capacitance
XPS	X-ray photoelectron spectroscopy
E_g	Bandgap
N_{PD}	Number of dipoles
μ_0	Permanent dipole moment

Physical constants (unless otherwise specified)

h	Planck's constant (6.626×10^{-34} J·Hz^{-1})
ε_o	Permittivity of free space (8.85×10^{-12} F/m)
q	Electronic charge (1.6×10^{-19} C)
k	Boltzmann constant (1.38×10^{-23} J·K^{-1})

Contents

Chapter 3
Fabrication and Characterization Methods   **40-71**

Chapter 4

Chapter 5

Preface

Inventions in electrical transport mediated by protein macromolecules have contributed to the emergence of organic electronics over the past few decades. Proteins can serve as an interface between biological entities and electronic devices, and they are expanding the field of organic materials research. A new subject called "Proteotronics" has emerged as a result of the converging attention of several fields of science, from biology to electronics. Proteotronics' main goal is to create and put forth cutting-edge electronic devices depending on the specific properties of certain proteins.

Proteins and peptides with nanostructures are good materials for bioelectronic devices. Supramolecular protein and peptide nanostructures show extraordinary electronic characteristics in recent examples. They have a lot of the characteristics needed for biocompatibility, from enzymatic to organismal scales. However, a general understanding of their structure, made of amino acids and peptide bonds, does not clearly explain how such natural and manmade protein materials may conduct electrons at length scales spanning from micrometers to centimeters. The configuration of protein-based electronics and a complete understanding of protein function depend on protein-mediated charge transport.

The experimental work on the investigation of charge storage in proteins as well as application of protein as UV photoactive material are presented in this dissertation, together with a conceptual framework for understanding the experimental findings. This discovery should be helpful for those investigating the electrical properties of biocompatible materials and the creation of innovative protein-based molecular devices, such as the next-generation nanometric biological sensors.

The dissertation begins with a discussion of protein fundamentals, electron transfer, and transport within and across proteins. The current state of protein-based molecular electronics is then examined. Following is a concise

explanation of the various characterization methodologies used in this thesis. The principal content of the thesis is composed of three sections. In the first two sections, the structural, chemical, and morphological properties of bovine serum albumin and papain films, as well as their applications as MIM, Memristor, and UV photoactive materials are investigated. Analytical modelling is used to elucidate the dielectric properties of the proteins obtained experimentally. Different parameters of BSA based UV photoactive device were extracted from the photo-response obtained. In the third section, the process to fabricate and characterize a novel transient, soluble biopolymer gelatin substrate is demonstrated, and its application in an electronic device is reported. Finally, a summary of current research and the scope of 'Proteotronic' devices in the future are discussed.

Chapter 1: Motivation and Outline

1.1. Background and theory

In our present world of cell phones, laptops, tablets, and electric cars, charge storage devices are of significant importance in providing reliable and efficient sources of energy [1]. With the increasing demand of energy storage, future availability of raw materials to fabricate such devices is of utmost concern. Lithium-ion materials that comprises of most of the charge storage devices can face a dearth of production, which in turn may slow down the growth of energy manufacturing. Owing to the rapid advancement of the charge storage technology, storage devices require regular upgrades, therefore leading to shorter lifetime. These not-so-old unused devices results into electronic garbage (e-waste), that has been reported to exceed 50 million tons a year [1,2]. The present electronic world is much more concerned about the disposal of such a huge amount of e-trash [3,4]. The only way to ensure availability of future resources of charge storage devices, and to minimize the end-of-life impacts, is to move towards renewable, recyclable organic materials. The environmental challenge of growing e-wastes can only be curbed by relying on organic electronics that is known to generate minimal waste compared to inorganic electronic devices. Organic electronics have advantages such as flexibility, bio-compatibility, non-toxicity, ionic and electronic conductivity, that can be easily used to interface electronics in biological systems. Moreover, the processing of organic materials are easy, cost-effective and suitable for high manufacturing throughput [5]. Organic electronics has its applications in human-friendly device fabrication [6,7], specifically with significant interaction with live tissue [8-10].

1.1.1. Charge Storage Devices

Various kind of charge storage devices are present in modern electronics. Metal Insulator Metal (MIM) structures are of significant interest in this

dissertation. MIM structures has its applications as capacitors as well as memristors. Their fundamental theories are discussed briefly below:

1.1.1.1. Metal Insulator Metal (MIM) capacitors

FIG. 1.1. Lateral schematic of a MIM structure.

MIM structure as seen in FIG. 1.1, contains top and bottom metal electrodes and an insulator in between. The insulator is a material that has relatively wide bandgap between conduction and valence band, while metals exhibit overlapping conduction and valence bands. The structure acts as a parallel plate capacitor that shows capacitance equivalent to,

$$C = \frac{\kappa \varepsilon_0 A}{t} \qquad (1.1)$$

Here, the insulator thickness is denoted as 't', the area of the capacitor is 'A', the relative permittivity of the insulator is κ, the permittivity of free space is denoted as ε_0. It can be seen that the capacitance of a MIM device depends on dielectric thickness, relative permittivity of the insulator, and area of the device. The electrodes also influence the capacitance value as well as its nature, for example high metal work function is said to be a contributing factor for capacitance non-linearities. A DC bias voltage (V_{dc}) is applied, over which a small AC signal is superimposed, the cumulative capacitance (C), and parallel conductance (G) is measured as function of applied voltage and frequency of the AC current. The capacitance for MIM structure can be measured with the circuit models shown in FIG. 1.2.
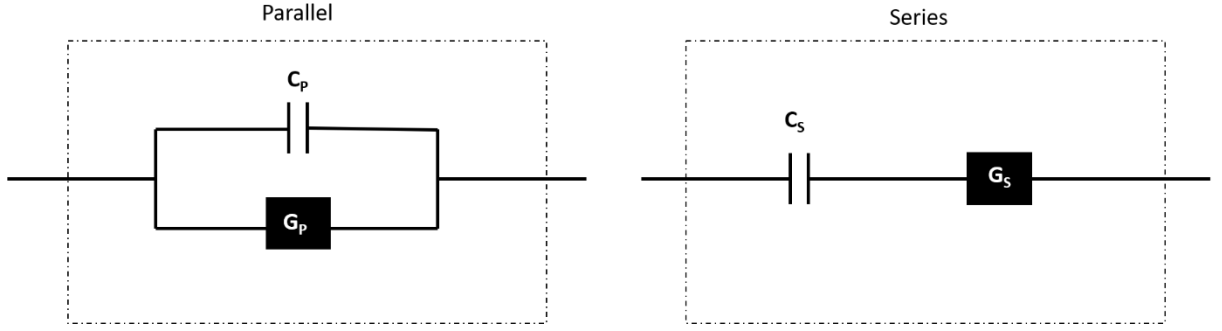
Parallel   Series

FIG. 1.2. Parallel and series circuit models used in measurements of the MIM-capacitors.

The resistivity of the MIM device can be represented by the equivalent series resistance (ESR). The ESR arise due to dielectric lag or ohmic contact resistance in metal structures. Low value of ESR is desirable to minimise power consumption of MIM devices. The following equations express series and parallel impedances:

$$Z_s = R_s + \frac{1}{j\omega C_s} \tag{1.2(a)}$$

$$\frac{1}{Z_p} = G_p + j\omega C_p \tag{1.2(b)}$$

equation (1.2(b)) can be rewritten as,

$$Z_p = \frac{G_p}{G_p^2 + \omega^2 C_p^2} - j\frac{\omega C_p}{G_p^2 + \omega^2 C_p^2} \tag{1.3}$$

where ω is denoted as angular frequency of the AC-signal, Z_s and Z_p gives the series and parallel impedances respectively.

The real part of the parallel impedance as shown in equation (1.3) defines the value of ESR. Thus, it is given as,

$$R_s = \mathrm{Re}\{Z_p\} = \frac{G_p}{G_p^2 + \omega^2 C_p^2} \tag{1.4}$$

The loss of energy in the capacitor can be explained by the dissipation factor (DF). DF varies with change in capacitance and with frequency. This loss occurs due to

presence of set of resistances in the device. DF can be calculated using series and parallel impedances:

$$DF = \frac{\text{Re}\{Z_p\}}{\text{Im}\{Z_p\}} \tag{1.5}$$

which gives,

$$DF = \frac{G_p}{\omega C_p} \tag{1.6}$$

The quality factor (Q) which is the inverse of DF can be written as,

$$Q = \frac{1}{DF} \tag{1.7}$$

The optimum value of Q must least be within a range of 10-100.

1.1.1.2. Metal Insulator Metal (MIM) Memristors

The term memristor had been proposed in the year 1971 by Leon Chua [11]. Memristor is a two terminal device that relates magnetic flux with electric charge, and the charge flowing through the device is responsible for varying its resistance. This can be mathematically expressed as [11]:

$$d\phi = Mdq \tag{1.8}$$

here, M is termed as memristance, while φ and q are of voltage and current time integrals, respectively.

It was seen that memristive behaviour exhibited in different devices such as spin-torque transfer device, phase-change memories, resistive switches, magnetic memories [12]. Memristors exhibit a pinched hysteresis loop, passing through the origin, whose shape varies with the change in frequency and input signals amplitude. Memristor stores the values of magnetic flux and electric charge even in absence of input bias, showing its potential application in non-volatile memory. Memristors possess a property of being scaled to much lower dimensions than existing non-volatile memories [13]. The change in dynamic resistance in the memristor can be utilized to imitate function of brain synapse.

The material's resistance is influence by external electrical stimuli and switches in-between high resistance state (HRS) and low resistance state (LRS). While changing from HRS to LRS, the applied voltage is termed as 'SET' voltage (V_{SET}), and LRS to HRS requires a 'RESET' voltage (V_{RESET}). The materials with bi-stable resistance shows, two modes of switching viz., unipolar mode and bipolar mode as shown in FIG. 1.3 and FIG. 1.4.
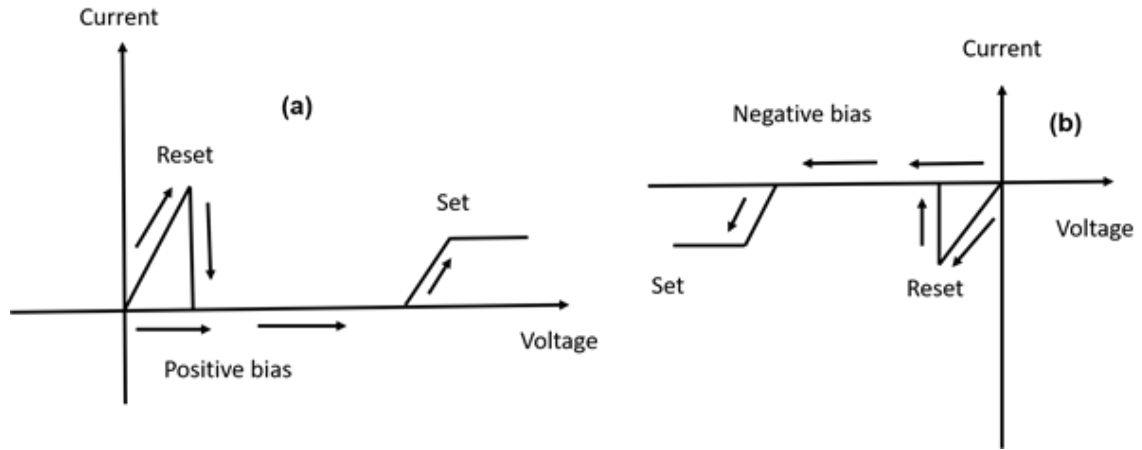
FIG. 1.3. (a) and (b) Unipolar switching of resistive materials.

The switching process that does not depend on polarities of voltage and current are known as unipolar switching. In case of switching to be unipolar in nature, the process of 'SET' and 'RESET' occurs in the same quadrant as seen in FIG. 1.3. In the bipolar switching mode these processes take place in opposite polarities, thus toggling the device between 'ON' and 'OFF' state with change in amplitude and polarity of applied bias. The resistive switching mechanisms can be explained by filament formation or ion migration [14].
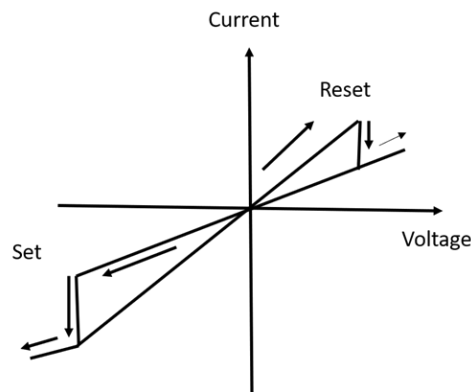
FIG. 1.4. Bipolar switching of resistive materials.

Unipolar switching occurs due to dielectric loss leading to filament formation initiated by joules heating. Switching may also occur due to electronic charge injection where injected electrons tunnel to the defect sites in the material thus decreasing the resistance. Bipolar switching as seen in FIG. 1.4 has been reported to be initiated by ionic migration and redox reaction [14]. The detailed process of filament formation will be explained in chapter 5.

1.1.2. Insulators in charge storage devices

Insulators can be polarized when placed in an electric field. This property gives rise to its application in charge storage. Insulating materials in charge storage devices commonly known as 'dielectrics' have the unique property of separating opposite charges without generating a steady current [3]. The diverse processes of polarization found in dielectric materials are shown in FIG. 1.5.
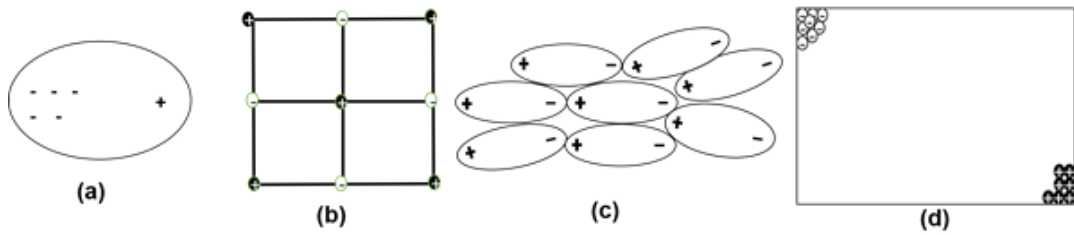
FIG. 1.5. (a) Electronic polarization: the relative displacement of the electron probability density; (b) Ionic polarization: displacement of ionic centers consistent across the crystals; (c) Orientational polarization: free moving electric dipole moments in molecules aligning due to electric field; (d) Space charge polarization: charge centers can move a long distance in the material.

The polarization of these materials can be quickly reversed upon reversing the applied field direction. On changing the polarity, the charges travel to the opposite direction quickly and accumulate. However, there is an exception in space charge polarization, where the ions move very slowly in response to electric field. The lag in this movement leads to high dissipation factor or low quality factor.

A dielectric is characterized by relative permittivity with respect to vacuum. The relative permittivity κ is multiplied with permittivity of free space. The dissipation factor (DF) can also be expressed in terms of permittivity,

$$DF = \frac{\varepsilon_r^{''}}{\varepsilon_r^{'}} = \tan \delta \tag{1.9}$$

It is defined as the ratio of imaginary and real part of the permittivity. The reduction in dielectric thickness results in dielectric loss, because of effect of quantum tunneling. Dielectric thickness is reduced to obtain higher capacitance density and better device performance. But according to Moore's law scaling down after a certain level is not favorable. Thus, attention of the present electronic world is towards finding dielectric material with higher relative permittivity.

Organic materials specially proteins are found to exhibit high dielectric constant, that does not require much thinner layer to achieve the desired capacitance density. Moreover, proteins require low operating voltages, which in turn reduces power consumption of the device.

1.1.3. Protein as dielectric

Proteins are sourced from biological materials, that are non-toxic, biocompatible, biodegradable, environment friendly [7], [15–17]. There is growing interest to fabricate protein based electronic devices.

These bio-polymers consists of amino acid sequences arranged in a 3-D structure comprising of α-helixes and β-sheets. These 3-D structures can be folded to give rise to tertiary protein structures, which can be again combined to quaternary structures [18,19]. Studies on the electronic nature of proteins are clearly not recent state-of-art, although it is essential to note that systematic applications have witnessed a huge increase over the past decade (shown in FIG. 1.6.) and are expected to maintain their upward trend.
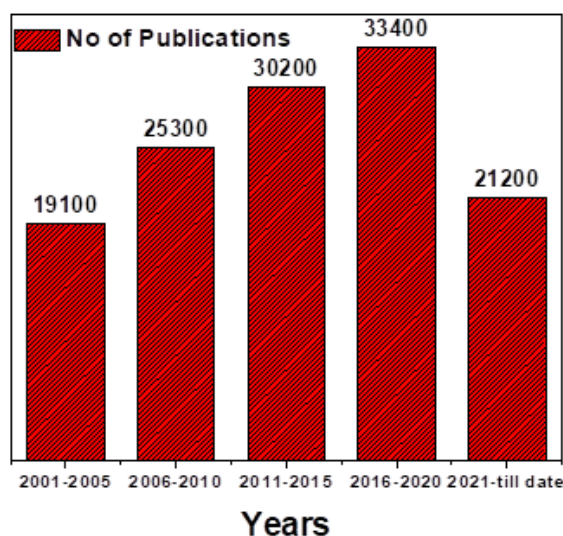
FIG. 1.6. Number of articles published on studies of proteins as dielectric materials since the year 2001.

Basic structure of protein contains one or more polar amino acids (-CO-CR-NH-), which can be attributed to the origin of polarization in proteins. The tertiary protein structure consisting of amino acids linked with peptide bonds is shown in FIG. 1.7(a). The 'R' part denotes the residue. Dihedral angles namely φ and ψ are formed due to rotation in certain bonds such as C–N and C–C respectively. The dihedral angles of φ and ψ that indicates rotational degrees of freedom in the protein responsible for its flexible property are shown in FIG. 1.7(a) (bottom part). Proteins characterized by α helix and β sheet structures are chemically reactive owing to their capability of bond formation [20,21]. Protein as dielectric material and its dipole properties has been studied much earlier experimentally [20]. Bovine Serum Albumin (BSA) an animal protein has been studied for its conductivity and polarization properties [22,23]. Dispersion in hydrated BSA was observed due to water bonding. Dielectric constant of BSA solution varied with applied frequency for 7 g/dl and 34 g/dl concentration obtained from previous reports is shown in FIG. 1.7(b). The data was extrapolated at different temperatures [22].

Theoretical studies were also performed to determine the dielectric properties of protein. A rigorous theoretical derivation for the determination of dielectric properties depending on applied frequency was performed by Loffler et.al. [24]. It was concluded that the dielectric property of the peptide can rightly be explained in terms of its water content. In another work by Lund et.al. [25], core of the protein molecule was assumed as a simple sphere, and the effect of the core structure on the surface charges determining the dielectric property of the molecule was simulated using Monte Carlo method. FrÖhlich-Kirkwood model was used to simulate fluctuation in protein dipole moment. This model was used by Pitera et.al. [20] to estimate the static dielectric constants of proteins, under different physical and chemical conditions. FIG. 1.7(c) summarizes the simulated values of dipole moment (M) with static dielectric constant (ε) of different proteins such as Hen Egg White Lysozyme (HEWL), α- lactalbumin (α-LAC), Rat Fatty Acid Binding Protein (FABP) and Llama antibody (LAMA) obtained from experiments [20]. The phosphodiester bonds that serve as protein backbone gets destabilized due to dehydration and results into formation of zwitterion. This zwitterion results into rise of conductivity in protein. The transport mechanism can be explained by constant redox reactions as explained by the Ramachandran Plot [26,27].
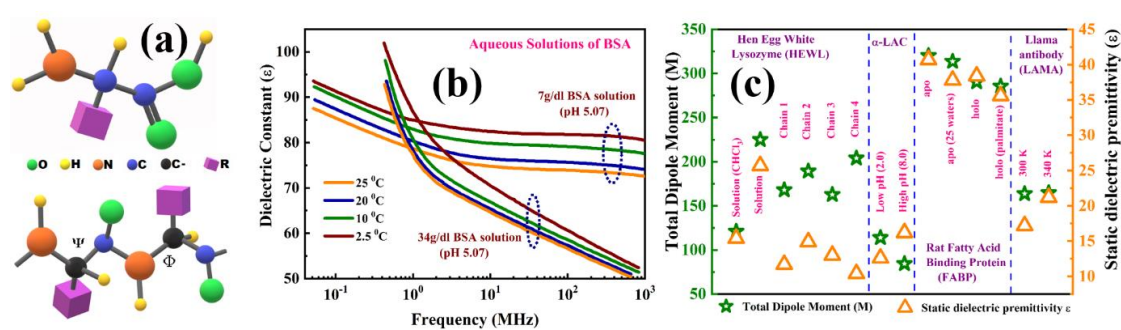
FIG. 1.7. (a) The tertiary structure of protein, along with φ and ψ dihedral angles shown in between two groups of peptides [28]; (b) Permittivity ε' varying with applied frequency for BSA solutions of concentrations 7 g/dl and 34 g/dl [22]; (c) Simulated values of M and ε for HEWL, α-LAC, FABP and LAMA [20].

1.1.4. Ultra Violet (UV) photoactive devices

The devices that can absorb light and convert to electric signals are known as photoactive devices. Light falling on the photoactive layer generates electron hole pair which in turn produces electric current.

1.1.4.1. UV electromagnetic radiation

UV radiation a significant part of solar radiation has huge impact on the earth and mankind. UV detection is important field of research as the radiation causes various adverse health effects including cancer. UV radiation ranges from 100 nm to 400 nm wavelength [29]. It lies in between visible spectrum and X-rays as shown in FIG. 1.8.
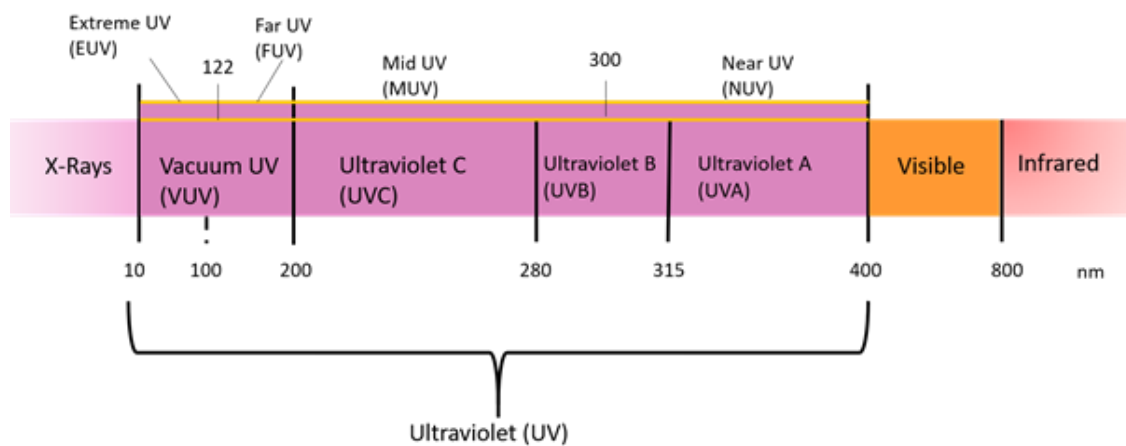
FIG. 1.8. UV spectral region and its subdivisions.

1.1.4.2. Different groups of Photodetectors

UV photodetectors are widely used in industry, defence, medicine, and environmental research. Photodetectors can be divided into two groups:

The first type involves photoelectric effect externally, which means the photons simulated the cathode and generate photoelectrons that are sent to the anode. This technology is used in photomultipliers [30].

The other type employs internal photoelectric effect, where the incident radiation is absorbed by the material and generates electron hole pairs. The

photocurrent varies proportionally with the intensity of incident light. Solid state devices such as CCD, metal-insulator-semiconductor photoelectric detectors use this mechanism [31].

1.1.4.3. Protein as Photoactive material

Proteins generally exhibit insulating characters, but they also exhibit long-range electron transfer (ET) property, that may be used in generation of electron-hole pairs upon simulation with photons. Protein has been not been exploited as photodetectors in wide range. However, some of the works are noticeable and can be used as starting point. Tokita et. al. has reported protein based photodiode and photoconductor [32]. They have shown that cytochromes substituted with zinc demonstrate photoinduced electron transfer. Light sensitive bacteriorhodopsin was reported as photodetector employed in motion sensing [33]. Protein has been used to interface with graphene based device to enhance its photodetection abilities [34].

1.2. Objective of the Thesis

The fundamental purpose of this work is to explore the dielectric characteristics of plant and animal proteins, to fabricate and characterize protein based charge storage devices, and to comprehend the device mechanisms by discussing charge transport pathways. Protein will also be explored as UV photoactive material. Furthermore, we propose a fully organic, transient, soluble, transparent, bio-degradable substrate as starting material for device fabrication.

As stated earlier, organic electronics are the only option to make reusable biodegradable electronic gadgets to meet the current situation, and we will demonstrate how proteins, in addition to being a vital component of animal and plant physiology, are progressively becoming unintelligible in dielectrics as well as electronic substrate applications.

In order to attain the objective, the work will be divided into two categories; one is studying protein as only dielectric material and the other is developing

conventional green device made of protein substrate as well as protein dielectric. At initial stage of this work, animal protein BSA and plant protein papain films will be prepared and characterized for dielectric applications, along with appropriate analytical modeling. In the second part, transient biodegradable substrate made of gelatin will be fabricated and MIM capacitor will be fabricated on this substrate to produce a fully 'Proteotronic device'.

Overall, we will find that protein as a dielectric has good charge storage and resistive switching properties. The gelatin based protein biopolymer substrate will also show good mechanical and morphological properties, making it appropriate for electronic device fabrication.

Conclusively, the aim of this thesis is to develop high-quality, low-cost Proteotronic gadgets for a future bio-compatible green electronic society.

1.3. Organization of the Thesis

Detailed characterizations of the physical, structural and electrical properties of the MIM structures fabricated with protein based dielectric materials have been performed during the course of dissertation. The organization of the thesis is briefly outlined below:

In Chapter 1, we have described the objective of our work. The importance of our present work is also described. The organization of the whole thesis work has also been described.

In Chapter 2, we have reviewed the related available literature on protein based MIM and Memristor devices.

In Chapter 3, overall process of protein film deposition and structural and analytical characterization techniques that have been used to study the physical and electrical properties of protein films are discussed.

In Chapter 4, fabrication of bovine serum albumin (BSA) based MIM structure on ITO coated PET as well as paper substrate and study of its application

in Radio frequency devices and as UV photoactive material respectively are discussed.

In Chapter 5, the structural and electrical properties of plant based protein papain have been studied and its application as dielectric in MIM and Memristor devices are demonstrated.

In Chapter 6, a novel, transient, bio-degradable, transparent protein bio-polymer substrate made of gelatin has been fabricated and BSA based MIM capacitor developed on that green substrate has also been investigated.

In Chapter 7, the conclusions of this research are summarized and the possible future directions are indicated.

Reference:

[1] K. Zhang, J. L. Schnoor, and E. Y. Zeng, "E-waste recycling: where does it go from here?," *Environ. Sci. Technol.*, vol. 46, no. 20, pp. 10861–10867, 2012.

[2] M. Heacock *et al.*, "E-waste and harm to vulnerable populations: a growing global problem," *Environ. Health Perspect.*, vol. 124, no. 5, pp. 550–555, 2016.

[3] B. H. Robinson, "E-waste: an assessment of global production and environmental impacts," *Sci. Total Environ.*, vol. 408, no. 2, pp. 183–191, 2009.

[4] R. Widmer, H. Oswald-Krapf, D. Sinha-Khetriwal, M. Schnellmann, and H. Böni, "Global perspectives on e-waste," *Environ. Impact Assess. Rev.*, vol. 25, no. 5, pp. 436–458, 2005.

[5] J. Zhao *et al.*, "Recent developments of truly stretchable thin film electronic and optoelectronic devices," *Nanoscale*, vol. 10, no. 13, pp. 5764–5792, 2018.

[6] T. Sekitani and T. Someya, "Human-friendly organic integrated circuits," *Mater. Today*, vol. 14, no. 9, pp. 398–407, 2011.

[7] M. Irimia-Vladu, N. S. Sariciftci, and S. Bauer, "Exotic materials for bio-organic electronics," *J. Mater. Chem.*, vol. 21, no. 5, pp. 1350–1361, 2011.

[8] M. D. Angione *et al.*, "Carbon based materials for electronic bio-sensing," *Mater. today*, vol. 14, no. 9, pp. 424–433, 2011.

[9] M. Muskovich and C. J. Bettinger, "Biomaterials-based electronics: polymers and interfaces for biology and medicine," *Adv. Healthc. Mater.*, vol. 1, no. 3, pp. 248–266, 2012.

[10] M. C. Serrano, E. J. Chung, and G. A. Ameer, "Advances and applications of biodegradable elastomers in regenerative medicine," *Adv. Funct. Mater.*, vol. 20, no. 2, pp. 192–208, 2010.

[11] L. O. M. Chua, "The missing circuit element. Circuit Theory," *IEEE Trans. Electron Devices*, vol. 18, pp. 507–519, 1971.

[12] L. O. Chua, "The fourth element," *Proc. IEEE*, vol. 100, no. 6, pp. 1920–1927, 2012.

[13] Y. Ho, G. M. Huang, and P. Li, "Dynamical properties and design analysis for nonvolatile memristor memories," *IEEE Trans. Circuits Syst. I Regul. Pap.*, vol. 58, no. 4, pp. 724–736, 2010.

[14] M. H. R. Lankhorst, B. W. Ketelaars, and R. A. M. Wolters, "Low-cost and nanoscale non-volatile memory concept for future silicon chips," *Nat. Mater.*, vol. 4, no. 4, pp. 347–352, 2005.

[15] M. Irimia-Vladu, E. D. Głowacki, G. Voss, S. Bauer, and N. S. Sariciftci, "Green and biodegradable electronics," *Mater. Today*, vol. 15, no. 7, pp. 340–346, 2012.

[16] J.-W. Chang, C.-G. Wang, C.-Y. Huang, T.-D. Tsai, T.-F. Guo, and T.-C. Wen, "Chicken Albumen Dielectrics in Organic Field-Effect Transistors," *Adv. Mater.*, vol. 23, no. 35, pp. 4077–4081, Sep. 2011.

[17] S.-W. Hwang *et al.*, "Biodegradable elastomers and silicon nanomembranes/nanoribbons for stretchable, transient electronics, and biosensors," *Nano Lett.*, vol. 15, no. 5, pp. 2801–2808, 2015.

[18] G. E. Schulz and R. H. Schirmer, *Principles of protein structure*. Springer Science & Business Media, 2013.

[19] W. Norde, "My voyage of discovery to proteins in flatland... and beyond.," *Colloids Surf. B. Biointerfaces*, vol. 61, no. 1, pp. 1–9, 2007.

[20] J. W. Pitera, M. Falta, and W. F. van Gunsteren, "Dielectric properties of proteins from simulation: the effects of solvent, ligands, pH, and temperature," *Biophys. J.*, vol. 80, no. 6, pp. 2546–2555, 2001.

[21] F. Bibi, M. Villain, C. Guillaume, B. Sorli, and N. Gontard, "A review: Origins of the dielectric properties of proteins and potential development as bio-sensors," *Sensors (Switzerland)*, vol. 16, no. 8, pp. 1–21, 2016.

[22] E. H. Grant, S. E. Keefe, and S. Takashima, "Dielectric behavior of aqueous solutions of bovine serum albumin from radiowave to microwave frequencies," *J. Phys. Chem.*, vol. 72, no. 13, pp. 4373–4380, Dec. 1968.

[23] J. Eden, P. R. C. Gascoyne, and R. Pethig, "Dielectric and electrical properties of hydrated bovine serum albumin," *J. Chem. Soc. Faraday Trans. 1 Phys. Chem. Condens. Phases*, vol. 76, no. 0, pp. 426–434, 1980.

[24] G. Löffler, H. Schreiber, and O. Steinhauser, "Calculation of the dielectric properties of a protein and its solvent: theory and a case study11Edited by R. Huber," *J. Mol. Biol.*, vol. 270, no. 3, pp. 520–534, 1997.

[25] M. Lund, B. Jönsson, and C. E. Woodward, "Implications of a high dielectric constant in proteins," *J. Chem. Phys.*, vol. 126, no. 22, p. 225103, Jun. 2007.

[26] C. D. Bostick, S. Mukhopadhyay, I. Pecht, M. Sheves, D. Cahen, and D. Lederman, "Protein bioelectronics: a review of what we do and do not know," *Reports Prog. Phys.*, vol. 81, no. 2, p. 26601, 2018.

[27] "Dielectric," *J. Biol. Chem.*, vol. 90, p. 443, 1930.

[28] E. Alfinito, J. Pousset, and L. Reggiani, *Proteotronics: Development of Protein-Based Electronics*. Jenny Stanford Publishing, 2015.

[29] B. Leckner, "The spectral distribution of solar radiation at the earth's surface—elements of a model," Sol. energy, vol. 20, no. 2, pp. 143–150, 1978.

[30] A. Rogalski, Z. Bielecki, J. Mikołajczyk, and J. Wojtas, "Ultraviolet Photodetectors: From Photocathodes to Low-Dimensional Solids," Sensors, vol. 23, no. 9, p. 4452, 2023.

[31] M. Razeghi and A. Rogalski, "Semiconductor ultraviolet detectors," J. Appl. Phys., vol. 79, no. 10, pp. 7433–7473, 1996.

[32] Y. Tokita et al., "Protein photoconductors and photodiodes," Angew. Chemie Int. Ed., vol. 50, no. 49, pp. 11663–11666, 2011.

[33] W. W. Wang, G. K. Knopf, and A. S. Bassi, "Protein-based photocell for high-speed motion detection," in Proceedings of IEEE Conference on Control Applications, pp. 731–736, 2005.

[34] J. Tong, L. Zhang, Y. Wang, and T. Li, "High Response Photodetection by Applying the Optimized Photoreceptor Protein Modification on Graphene Based Field Effect Transistors," Front. Mater., vol. 7, p. 222, 2020.

Chapter 2: Literature Review: Proteotronic devices and Organic Soluble Substrates

As stated in the previous chapter, the aim of the thesis is fabrication and study of characteristics of protein based charge storage devices. In addition to that fabrication of a fully organic, transient, soluble, transparent, bio-degradable substrate as starting material for device, is also our goal. In an effort to provide a critical overview of protein in electronics, this review will concentrate on some of the most representative articles published in the past decade to provide a more comprehensive understanding of next-generation materials for Proteotronic applications in futuristic charge storage devices. The purpose is to provide examples of current reports of charge storage devices based on protein as dielectric, in order to compare and contrast their advancements and shortcomings. The proteins used for as dielectric in this dissertation (BSA and papain) and the protein used as soluble transient substrate (gelatin) have been discussed initially as focus materials. The fabrication techniques for protein based devices such as metal-insulator metal (MIM) capacitors, memristors, are also discussed. Various organic soluble substrates reported till date are also reviewed.

2.1. Focus materials and their properties

In this dissertation bovine serum albumin and papain have been studied as dielectric for electrical as well as optoelectronic application, and gelatin has been investigated for its potentiality in electronic substrate applications. The basic properties of the focus materials are thus discussed below:

2.1.1. Bovine Serum Albumin (BSA)

Bovine serum albumin (BSA), with the other name "Fraction V," originating from serum albumin is synthesized in the liver of domestic cows, specifically Bos Taurus. The term "Fraction V" is a reference to classification of albumin as the fifth fraction in the purification process originally developed by Edwin Cohn. This

process relied on the plasma protein's characteristics of differential solubility. BSA is a globular, non-glycosylated protein, that stands out to be lacking carbohydrate groups which is rare in plasma proteins. The molecular weight of BSA is 66 kDa, and constitutes roughly 60% of all proteins found in animal serum. Due to its negative charge, BSA has the ability to bind to water, salts, fatty acids, vitamins, and hormones. It serves as a carrier for these bound components, facilitating their transport between tissues and cells.

The complete precursor of BSA consists of 607 amino acids. During secretion, a signal peptide 18-residue is cleaved from the protein precursor, resulting in 589 residual amino acids. Subsequently, six amino acids happen to be enzymatically removed, resulting in matured BSA with 583 amino acids [1]. A distinctive structural attribute of BSA is its limited presence of tryptophan, methionine, glycine, and isoleucine, contrasted with its abundance of ion incorporated amino acids like lysine and glutamic acid. These residues of ionization impart notable increased overall charge to the protein, amounting to 185 ions/molecule under pH of neutral value, which significantly enhances its solubility.

Albumins are commonly employed as stabilizing agents for other solubilized proteins, particularly labile enzymes. BSA, known for its exceptional stability and minimal interference with biological activities, finds extensive use in various biochemical applications. These include applications in immunochemistry, Western blotting, and ELISA, where it serves as a blocking reagent. Additionally, BSA has the capacity to act as an antioxidant by capturing and neutralizing harmful free radicals. BSA can also be conjugated with fluorescent tags, enabling its utilization in tracer studies when combined with anti-BSA antibodies.

2.1.2. Papain

Papain is categorized as a cysteine hydrolase known for its stability and activity across a broad spectrum of conditions. Its remarkable stability extends to

even high temperatures, making it a versatile enzyme for various applications [2]. The latex obtained from Carica papaya serves as a valuable reservoir of endopeptidases containing four cysteine, namely chymopapain, papain, caricain and glycyl endopeptidase. These proteins from Carica papaya are initially synthesized as precursors that is inactive but they rapidly activate, typically taking only three minutes after injuring the papaya and the latex being released. The first exploration of papain's actions dates back to 1873 in a research conducted by G.C. Roy for the Calcutta Medical Journal and published with title "The Solvent Action of Papaya Juice on Nitrogenous Food Components." It was later in the late nineteenth century that the name "papain" was coined by Wurtz and Bouchut, who partially purified this enzyme from papaya sap [3]. When it was initially named, papain was identified as proteolytic active component. Notably, papain was also the first cysteine protease to have its structure elucidated [4]. Papain is characterized by its considerable heat resistance, displaying an optimal temperature range for activity between 60 to 70 °C. It also exhibits a broad pH tolerance, with its activity spanning the pH range of 5 to 8 [5].

Papain protein is globular with a 23406 Daltons molecular weight and is composed of 212 amino acids. Its structural stability is maintained by the presence of three disulfide bridges. X-ray structure analysis has revealed that these proteins adopt identical three-dimensional folds [6]. The 3D papain structure comprises distinct domains of two structures with a separation. Active site lies within the cleft, housing three amino acids: histidine-159, cysteine-25, and asparagine-158. The mechanism of peptide bond cleavage by papain involves the deprotonation of Cys-25 by His-15.

Papain possesses a broad proteolytic function, capable of breaking down peptides with short chains, proteins, esterified amino acids, and amide-linked compounds. Its versatility finds applications in both medicinal and food industries. In the realm of food preparation, papain is used in its active powdered form to tenderize meat by breaking down meat fibers. In cell culture preparations, papain is a valuable tool for cell dissociation. In various enzymatic formulations,

it is employed for cleaning purposes, aiding in the removal of infected cells or tissues. Papain also finds its way into toothpaste formulations, where it contributes to teeth whitening. Additionally, for the treatment of tooth decay, papain is used in a gel called "papacaries." It's worth mentioning that papain can interfere with drug tests for urine and is used as a detox agent. Nevertheless, it's essential to exercise caution, as papain included in drug products and balancing salt solutions has been associated with adverse effects such as vision loss, decreased blood pressure, and an elevated heart rate [7].

2.1.3. Gelatin

Gelatin, sometimes spelled as gelatine, has its origin in the Latin word "gelatus," meaning "stiff" or "frozen." It is a transparent, colorless, and tasteless material commonly obtained from collagen found in animal body parts. Gelatin is the result of irreversible hydrolysis of collagen, a process that forms smaller peptides by breaking down fibrils of protein. Notably, gelatin has a melting point that is below human body temperature, which is a significant factor in determining the mouthfeel of foods containing gelatin. The viscosity of a mixture of gelatin and water is at its highest when the gelatin concentration is high, and the mixture is maintained at a cool temperature, typically around 4 °C (39 °F).

Typically, gelatin of two distinct types can be manufactured, depending on initial processing of collagen. Type A gelatin undergoes treatment with acid and have its isoelectric point within the pH range of 6 to 9. It is commonly employed for collagen extracted from pig skin, which is less covalently crosslinked. On the other hand, treatment of Type B gelatin is alkaline with isoelectric point at pH 5. Type B is suitable for collagen derived from more complex sources like bovine hides [8].

From a chemical standpoint, gelatin consists of 18 different complex amino acids. Approximately 57% of its composition is comprised of hydroxyproline, proline, and glycine constituents. The remaining 43% is made up of various other noteworthy amino acid groups, including arginine, alanine, glutamic acid, and

aspartic acid [9]. Gelatin constituted by approximately 50.5% carbon, 6.8% hydrogen, 25.2% oxygen, and 17% nitrogen. In its structure, it exhibits a combination of both single unfolded chains and double unfolded chains, with hydrophilicity [10]. Gelatin comprises various polypeptide chains, including alpha (α)-chains, beta (β)-chains, and gamma (γ)-chains [11].

Typically, gelatin is available in various forms such as tablets, granules, or powders [12]. Researchers extensively investigate gelatin as a 3-D cell culture matrix and as a vital constituent in tissue-engineering [13]. In the medical field, gelatin finds applications in various forms, including pharmaceutical additives, nanofibers, nanomicrosphere containers, and hydrogels [14]. Furthermore, gelatin can serve as a valuable component in air filters designed for the analysis of airborne microorganisms, aiding in their retention and detection, which is crucial for identifying allergens that trigger allergic reactions. Additionally, gelatin has found innovative and intriguing applications, including its use in forensic science, particularly in the area of shoe print lifting [15].

2.2. Metal Insulator Metal Proteotronic devices

Protein based MIM structures were fabricated using Keratin and Silk protein [16]. Keratin device was reported on highly doped n-type Si wafer, while the silk device was patented on PET substrate. Keratin solution was dropcasted on Al coated Si substrate and the device was fabricated with 70 nm Al top and bottom electrodes. 500 nm dried Keratin film was washed in distilled water and annealed at 70 ^{0}C. For Au/Silk/Au structure bottom gate electrode 80nm thick Au was evaporated on PET substrate, which was then dipped in silk solution for 15 mins and dried at 60 ^{0}C temperature. The process was repeated several times to form silk dielectric multilayer of 400 nm. The two devices parameters are shown in the Table 2.1. Leakage current for both the devices were similar in the order of $10^{-7}A/cm^2$. Silk exhibited a dielectric constant of 7.2 which is higher than 3.5 value of keratin. The effect of protein denaturation on leakage current of Keratin MIM was studied and formation of disulphide bridges on cysteine was found to be

responsible for low surface roughness of the dielectric [17]. Two different mechanism of current conduction was observed in Keratin based MIM structure, Poole–Frenkel (PF) emission, and Schottky–Richardson (SR) emission. The relative change in current density due to varying time of exposure to open atmosphere was studied. It was observed that the keratin dielectric adsorbs moisture readily and the leakage current increases 76% after exposure of 4days.

Table 2.1. Preparation method and performance of Proteotronic MIMs

Device structure	Deposition method	Dielectric thickness (nm)	Capacitance at 1MHz (nFcm^{-2})	dielectric constant (at 1 KHz)	Leakage Current density (Acm^{-1})	Ref.
Al/Keratin/Al	SC	500	4.2	3.5	7x10^{-7}	[18]
Au/Silk/Au	DIC	400	14.26	7.2	1.2x10^{-7} at -0.01 MVcm^{-1}	[16]

SC* spin coating, DIC* dip coating

2.3. Memristive Proteotronic devices

Table 2.2. Preparation method and performance of Proteotronic Memristors

Device Structure	Deposition method	Dielectric thickness (nm)	Endurance (cycle)	Retention (S)	On/off ratio	Dominating Conduction mechanism *HV- High Voltage *LV- Low Voltage		Resistive switching mechanism	Ref.
						LRS (ON STATE)	HRS (OFF STATE)		
Al/CEA:Au@SiO2/ITO/Glass	SC	377	>10^2	>10^4	>10^5	Ohm's Law (LV), Mott-Gurney law, Child's law (HV)	Ohm's law (LV), trap-controlled space-charge-limited current (TC-SCLC) and the trap-filling process (HV)	Formation and rupture of Fe ions based filament	[19]
Ag/Albumen/ITO/PET	SC	300	>100	1.1x10^5	2x10^7	Ohm's Law	Ohm's Law (LV), Mott–Gurney law, trap-filling process	rapid trap-filling process of the	[20]

Device Structure	Deposition method	Dielectric thickness (nm)	Endurance (cycle)	Retention (S)	On/off ratio	Dominating Conduction mechanism *HV- High Voltage *LV- Low Voltage		Resistive switching mechanism	Ref.
						LRS (ON STATE)	HRS (OFF STATE)		
								injected charge carriers	
Al/Albumen/ITO/Glass	SC	270	~500	>10^4	>10^3	Ohm's law	Ohm's Law, trap-controlled space charge limited current (TC-SCLC) model	electron hopping along filaments formed by the Fe ions or redox centers	[21]
Mg/Collagen/ITO/PET	SPRC	80		-	-	space-charge-limited conduction (SCLC)	Ohm's Law	migration and diffusion of Mg ions	[22]
Ag/Silk/Au	SC	150	>100	>500	~60	Ohm's Law	Ohm's Law (LV), space-charge limited (SCL) (HV)	migration of Ag ions	[23]
Al/Silk/ITO/Glass	DC	357	>500	>10^4	>10^3	Ohm's Law	Ohm's Law (LV), Child's law (space-charge-limited current (SCLC)) (HV).	The capture and emission of electrons in conductive filaments	[24]
Al/Silk/ITO/Glass	SC	400	>10	>10^3	~11	-	-	Formation and rupture of metallic filament	[25]
Al/Silk-Au/PET	SC	150	10	10^3	10^6	-	-	cluster of aggregated Au particles	[26]
Mg/Silk/W/PET	SC	120	100	10^6	>10^5	-	Ohm's Law	growth and rupture of	[27]

Device Structure	Deposition method	Dielectric thickness (nm)	Endurance (cycle)	Retention (S)	On/off ratio	Dominating Conduction mechanism *HV- High Voltage *LV- Low Voltage		Resistive switching mechanism	Ref.
						LRS (ON STATE)	HRS (OFF STATE)		
								metallic filament	
Mg/Silk/Mg/Au/Si	DC	120	100	>10^4	>10^5	Ohm's Law (LV), space-charge-limited (HV)	Ohm's Law (LV), space-charge-limited (HV)	charge trapping/ detrapping between Ag nanoparticles	[28]
Au/DNA/Au/Si	SC	112	>100	>10^5	28	Ohm's Law	Ohm's Law (LV), trap-controlled space charge limited conduction (SCLC)(HV)	Charge trapping/ detrapping in DNA layers	[29]

SC* spin coating, SPRC*spray coating, DC*drop casting

The properties of protein based memristors are shown in Table 2.2. Albumin based memristors were fabricated on ITO substrates. The albumin can be easily separated from egg yolk and spin coated on the substrate for device fabrication. Bok et. al. used a mixture of core shell Au@SiO$_2$ and albumin as dielectric [19]. The dielectric thicknesses were around 200-400 nm. Post-coating the albumin films were subjected to anneal at high temperature to obtain better switching performances. Al was used as top electrode and deposited using thermal evaporation [19,21]. However, Qu et. al. used ink printed silver top electrodes with 150μm diameter [20]. Core shell Au@SiO2 and albumin mixture dielectric was reported to have better performance than only albumin memristors with difference in 3 order magnitude of on-off ratio [19]. The endurance value was found to be 500 cycles in the film with lowest thickness (270nm). The devices showed similar retention characteristics of >10^4 s. Within all the devices examined, it was observed that in low voltages, set the current-voltage curves slope in both ON and OFF state had a value of roughly 1. This finding suggests that mechanism

of current conduction was primarily governed by Ohm's law. At high voltage the slope of the curve during the ON state is around 2, suggesting Mott-Gurney law as the mechanism of current transport [30]. At high voltages, the observed slope of the OFF state was around 3, suggesting that the prevailing current-transport mechanism consisted of trap-controlled space-charge-limited current (TC-SCLC). These traps, located within the insulator, act as space charges. When -ve voltage is applied the electron gets introduced into the defect states, leading to an intensified electric field experienced by the albumen film. The reduction of oxidized Fe ions and the diffusion of oxygen ions in a group of Al atoms into the albumin film occur when the strength of the given negative voltage surpasses V_{SET}. This phenomenon is attributed to the presence of a sufficiently strong electric field. The albumen facilitates the formation of conductive filaments enabling carrier movement by the incorporation of Fe ions. At this juncture, the albumen film, which initially exhibits high resistance, undergoes a transformation into a condition of low resistance. Applied higher positive voltage VRESET, involves the reversal of the process, resulting in the disconnection of the filaments. Consequently, the memory devices regain their high-resistance status. The process of protein denaturation has the potential to alter the pathways through which oxygen diffuses, leading to a reduction in the likelihood of oxygen scattering. Consequently, this could create favorable conditions for the occurrence and subsequent disruption of conductive filaments.

Transparent bio-memristor using collagen was fabricated on ITO coated PET substrate using Mg as top electrode [22]. To generate the dielectric, a substrate was coated with a collagen solution using a spin-coating technique, resulting in the formation of a film having an approximate thickness of 80 nm. The author also noted that the substitution of the Mg top electrode by Al had no discernible impact on the device properties. Ohmic conduction and space-charge-limited conduction (SCLC) contribute to primary conduction mechanisms that govern the high resistance (HRS) and low resistance states (LRS). The SCLC traps are ascribed to the structural abnormalities in collagen, which give rise to trap located below conduction band. Ohmic conduction mechanism under low bias voltage can be

attributed to electric field insufficient of traversing the width, resulting in a lower number of charge carriers injected in comparison with thermally generated charge carriers. The capture of trap centers by numerous charge carriers is facilitated by the amplification of voltage, resulting in a conduction mechanism that adheres to a square-law relationship with voltage. A transition from the SCLC to the Ohmic characteristic was noted as the applied bias was decreased.

Defects within the thin film undergo a process of random dispersion, leading to their assembly. Consequently, the migration of Mg occurs through these assembled defects. Consequently, the observed rise in current over a positive voltage sweep can be attributed to the progressive augmentation of ion concentration throughout the established procedure. On the other hand, the gradual reduction in electrical current can be attributed to the increasing enlargement of the region depleted of magnesium throughout the process of resetting. The occurrence of switching events contributes to the development of zones with high conductivity, potentially due to the localized accumulation of magnesium.

Silk based memristors using different top and bottom electrodes are most widely reported compared to other proteins [30-35]. The process of silk extraction, as documented by Wang et al. was from the cocoons of Bombyx mori by boiling in a solution of 0.02 M Na_2CO_3 for a duration of 45 minutes. Subsequently, the cocoons were thoroughly washed with DI water to eliminate the adhesive substance known as sericin. Subsequently, the fibers were treated with lithium bromide (LiBr) solution with a concentration of 9.3 M, while maintaining a temperature of 60 °C. Subsequently, the resulting solution underwent dialysis in distilled water to eliminate any remaining LiBr residues, and was then subjected to centrifugation at a speed of 9000 rpm to obtain the fibroin solution. The supporting substrate was initially coated with a 50 nm gold. Subsequently, the fibroin liquid was applied onto the substrate coated with gold (Au) using the process of drop-casting. This was followed by allowing the coating to undergo crystallization in ambient air for a duration of 12 hours, in order to form homogeneous films with 10 μm thickness. Following that, the crystallized film

was detached from the substrate, resulting in the transfer of the Au film along with the fibroin film due to inadequate adherence of Au onto fluorinated saline treated silicon. The fibroin film, which was not attached to any other material, was meticulously positioned onto a substrate that provided support, ensuring that the layer of gold (Au) was facing upwards. Subsequently, another 120 nm thick silk film was deposited over the Au film using the spin-coating technique, serving as a resistive switching layer. Ultimately, the Ag electrodes were fabricated using thermal deposition. Following the fabrication process, the memory devices situated upon thin fibroin substrates have been separated from the underlying supporting substrate. In their study, Gogurla et al. developed a silk memristor with embedded Au nanoparticles. The memristor was produced on a substrate of indium tin oxide (ITO) covered PET, with an Al top electrode. The average thickness of this Silk-Au film, which was deposited using a silk-Au nanoparticles solution with a ratio of 10:1, measures 150 nm. The IV characteristics curves of silk memristor heterostructures commonly display an asymmetrical behavior accompanied by notable hysteresis, as shown on a linear scale. The endurance of silk memristors is influenced by factors such as the bias amplitude, electrode material and duration, as well as ambient conditions. The memristors exhibited a range of endurance values, spanning between 10 to 500 cycles. Additionally, retention values were found to be approximately between 10^3 and 10^4 seconds. These findings provide confirmation of the device's nonvolatile nature and its ability to facilitate nondestructive readout. According to Sun et al., the linear regression slope in LRS was 1, which strongly suggests the presence of Ohmic conductance. In HRS, the conduction in positive region is characterized by a low voltage regime. Within the high voltage range, the electrical behavior transitions from Ohmic characteristics to a space-charge limited (SCL) regime. This shift indicates a transition from trap-unfilled SCL conduction towards trap-filled SCL conduction.

The process of resistive switching in silk involves multiple stages, primarily characterized by the creation and disruption of conductive filaments composed of metallic materials. The behavior of resistive switching is

significantly affected by both the silk protein and Au NPs in this instance of nano-particle conjugated silk. The creation of conductive filaments during the 'SET' process can be attributed to the interaction between the positively charge silk fibroin and the negatively charged Au NPs, which is coulombic in nature. Silk fibrons were oxidised due to applied voltage on Al, resulting in the build-up of Au NPs in close proximity to the Al electrode. During the process of Single Electron Transfer (SET), a pathway of high conductivity is established connecting the electrodes. This pathway formed, act as a bridge connecting the electrodes. The Au NPs with a negative charge significantly contribute to change of state from insulation to conduction. During the reversal process, negatively biased Al electrode causes the filament to rupture. This rupture occurs as a result of repulsive forces exerted on the Au nanoparticles, along with the reduction of the fibroin. Consequently, the device transits into the 'OFF' state.

Calf thymus DNA fibre based bio-memristor was fabricated using gold electrodes [29]. The DNA solution was doped with Ag nanoparticles to enhance device performance. Au top electrodes with a thickness of approximately 30 nm were fabricated using low-temperature molecular beam epitaxy (LMBE) technique, using metal shadow mask at room temperature. The linear regression analysis reveals a slope of around 1.0 for the ON state, indicating a distinct manifestation of ohmic conductance characteristics. On the other hand, the conduction behavior during the off state has a complex nature. In the regime of low voltage, ohmic conduction dominates. At high applied bias, the conduction behavior adheres to the established principles of SCLC [38]. The traps below DNA conduction band serve as locations in which the injected charged particles may get caught. When the voltage surpasses the threshold of 0.73 V, all of the accessible traps become occupied, resulting in a sudden and significant surge in current. The device exhibits a consistent ON/OFF ratio over a duration of 10^5 seconds, indicating that the stored information within this device is expected to last long. This abrupt increase in current causes a transition to the ON state. It has been shown that the durability qualities remain intact even after switching over 100 cycles. It was seen that the set voltage exhibits a steady reduction as the

concentration of Ag+ increases, while the reset voltage remains nearly constant. The resistances of the OFF as well as ON state shows a decrease, whereas the ON/OFF ratio experiences minimal alteration.

2.4. Organic Soluble Substrates

Soluble substrates represent a category of materials known for their temporary functionality and consistent performance in everyday applications. They exhibit the ability to degrade entirely or partially when triggered by polar solvents or acids, a process driven by either physical or chemical mechanisms. In this section, we will delve into the origins, applications, and dissolution mechanisms of organic soluble substrates.

Organic substrates, often derived from eco-friendly biomaterials like guar gum, cellulose, and silk protein, have properties such as non-toxicity, biocompatibility, and biodegradability that make them ideal for use in transient electronics. These substrates are not only cost-effective but also deliver good performance, with exceptional degradation capabilities, showing great promise for wide-scale manufacturing of transient electronics.

2.4.1. Silk Protein

Silk protein is a natural fiber that supports the structure of the shells and webs of species named Lepidoptera [31]. The fibroin is sourced from Bombyx mori cocoons using established and standard silk extraction techniques [32]. The process of fabrication of silk substrate from raw silk is shown in FIG. 2.1(a) [33].

Hou et al. fabricated a sensor using protein [34], the characteristics of which is illustrated in FIG. 2.1(b). This capacitive pressure sensor is designed to measure various physiological movements, including tensile strains of human skin, swallowing, limb motion, and breathing. In the field of biomedicine, utilizing silk as a natural biopolymer substrate, a device was reported by *Kim et al.*[35, 36] [FIG. 2.1(c)]. *Hwang et al.*[37] integrated resistors, capacitors, transistors, and diodes into transient electronics on silk substrate. This circuit was constructed using materials like Si (semiconductors), MgO (dielectrics), and Mg (conductor) using transfer

printing method, as shown in FIG. 2.1(d). FIG. 2.1(e) (extreme left) represents a device attachable to human skin, a capacitive sensor fabricated for monitoring laryngeal activities and elbow movement such as drinking, swallowing, and pronunciation [34].
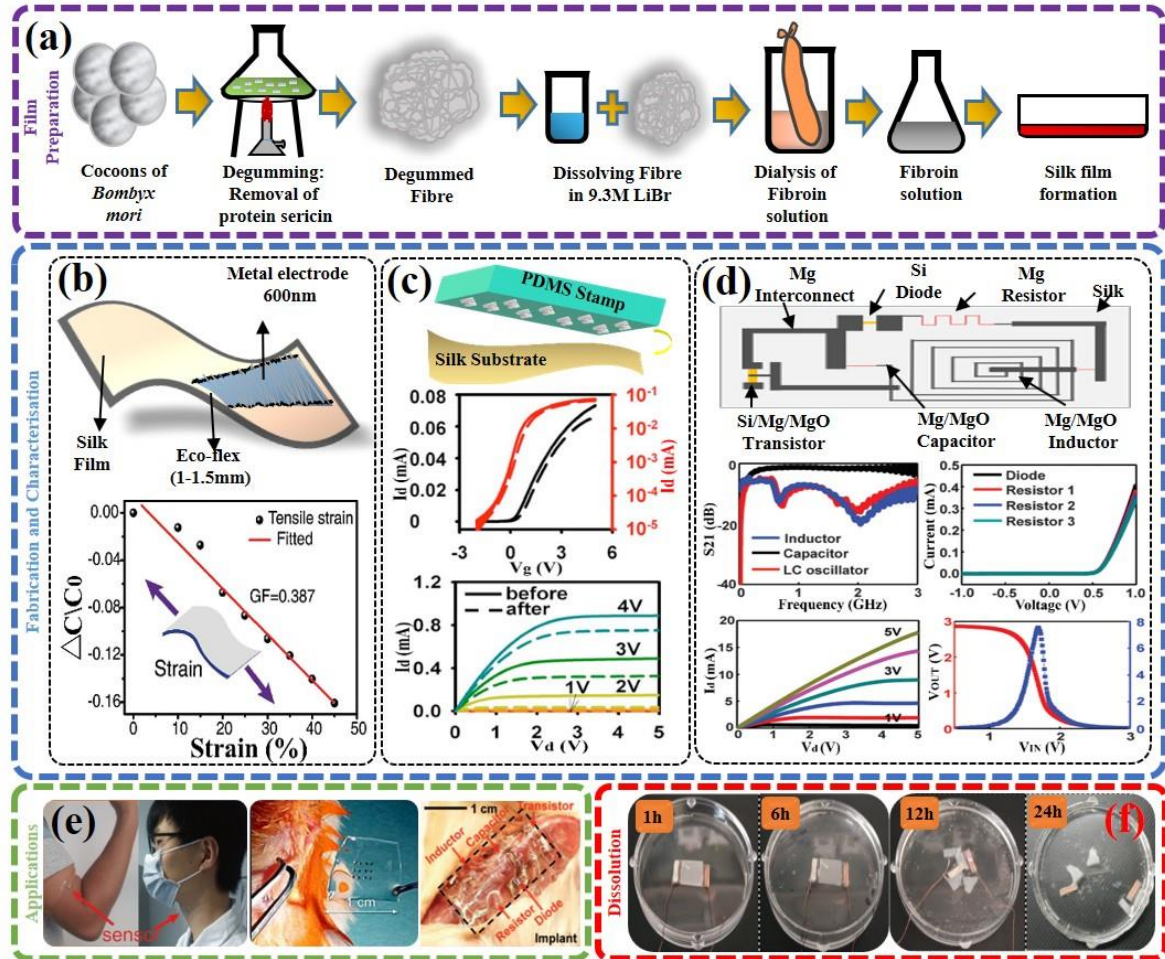
FIG. 2.1. (a) Silk films preparation process [33]; (b) Pressure–strain sensor capacitance curve [34]; (c) Process of printing on silk film; characteristics of the device pre and post dissolution [35]; (d) Interlayer dielectrics of different device interconnects on silk substrate [37]; (e) Body movements monitoring sensor *(left)* [34]; animal toxicity test device implant *(centre)* [35], [37]; (f) Ag NFs/SF films sensor degradation [34].

A device based on protein was implanted for biomedical applications, specifically for assessing in-vivo toxicity and inflammatory responses, as depicted in FIG. 2.1(e) (middle) [35]. One more device was implanted in a mouse BALB/c, specifically in the subdermal dorsal region, as shown in FIG. 2.1(e) (extreme right).

This implant was intended for heat therapy to control infections in the site of surgery [37].

Silk substrate dissolving mechanism: Sericin and silk fibroin are the two monofilaments of silk. Notably, sericin is soluble in water. The silk degradation can occur by two processes: in-vivo and in-vitro, in case of in-vivo the material is degraded by simulating enzymes, and in case of in-vitro the material degrades in a solution DI water [35], and phosphate-buffered saline (PBS) solution [39]. Though, degradation by in-vitro method are primarily favored owing to their practicality and the ability to obtain rapid results. When silk protein is immersed DI water or PBS solution, it undergoes hydrolysis and the polypeptides gets mixed. Subsequently, sericin, dissolves into the DI water and contributes to primary loss of silk. Over time, disintegration starts in the internal silk structures, resulting in solutes within the solution. In the dissolution test, after submerging the device in a solution of 5% papain, complete dissolution occurred after 24 hours at 37 °C [as shown in FIG. 2.1(f)] [34]. In DI water, the devices require approximately 10-15 minutes for complete dissolution,[35,37,38] whereas in PBS, it takes around 5 minutes[39]. It's noteworthy that silk films dissolves notably faster in the PBS solution[39].

2.4.2. Cellulose Nanofibril (CNF) Paper

Cellulose nanofibers (CNFs) are present in wood sources and are ecofriendly and animal compatible [40]. The fabrication process of CNF device starting from raw CNF is shown in FIG. 2.2(a) [41]. Meng et al. created a sensor on the CNF substrate through a process involving patterning with PDMS stencils as shown in FIG. 2.2(b) [42]. Metal-oxide-semiconductor field-effect transistors (MOSFETs) were fabricated on CNF substrate as shown in FIG. 2.2(c). An image depicting a transparent and flexible strain sensing device on CNF films with Ag electrodes as presented in FIG. 2.2(d) (left frame) [42], and silicon CMOS on the CNF substrate featuring a collection of digital logic circuits, is shown in FIG. 2.2(d) (right frame)] [40].

CNF paper dissolving mechanism: CNFs are capable to retain surface moisture when subjected to electrolytes, as hydrophilic groups are present in them.

Consequently, cellulose can form hydrogen bonds as the nature of their molecule is polar. On the other hand, water is recognized as a liquid with robust hydrogen bonding [43]. Achieving a perfect dissolution typically involves getting rid of some hydrogen bonds present in water, which in turn increases systems' total energy [44]. The pH of water can change when hydrogen bonds are broken or formed, but it's important to clarify that changes in pH are not a direct indicator of cellulose solubility in DI water [42], [43]. In experiments, it was observed that cellulose exhibits slight solubility of approximately 1.4 to 1.2 parts per 100,000 at room temperature in DI water. To illustrate CNF device degradation, a fungal degradation test was conducted, employing two distinct fungi: Postia placenta, a type of brown rot fungus, and Phanerochaete chrysosporium, a type of white-rot fungus. The device lost significant weight (9.96%) initially under the brown rot fungus. The cellulose film's decay process was observed over various durations as depicted in FIG. 2.2(e). During the first 10 days, partial decay occurred due to the brown rot fungus, while complete disintegration took place in 60 days [40].
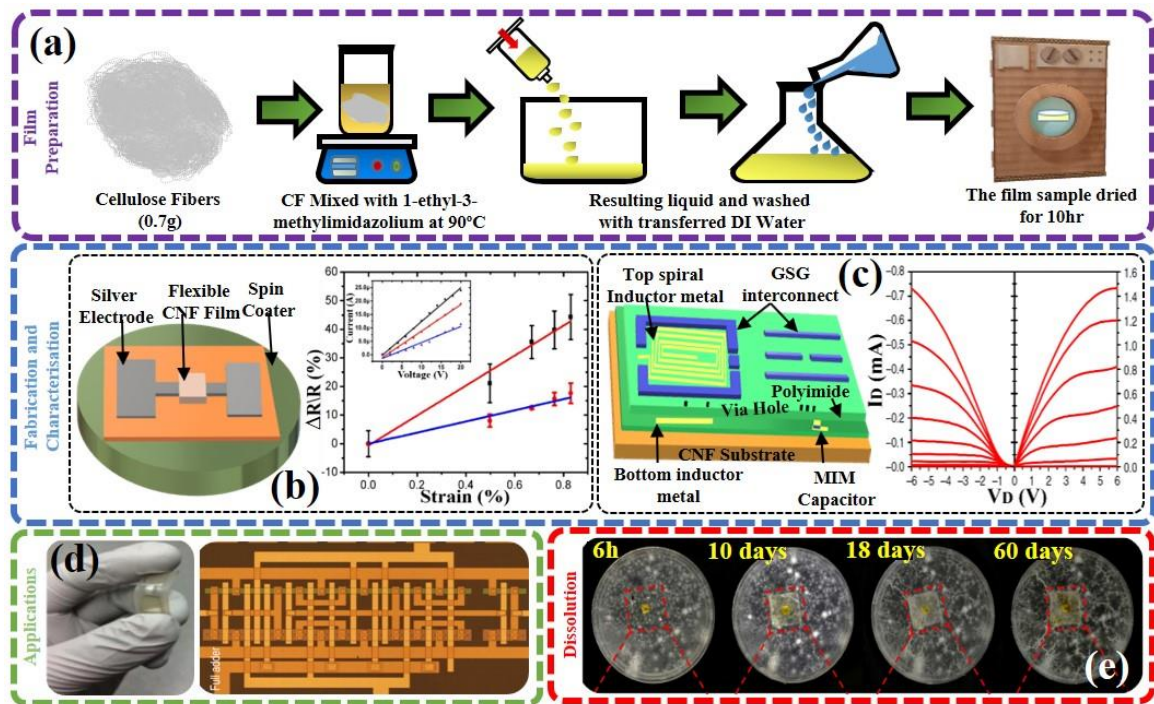
FIG. 2.2. (a) Flowchart illustrating cellulose substrate preparation from raw cellulose fibers; (b) Strain sensing device structure based on CNF and its characteristics [42]; (c) Schematic diagram of CNF substrate based MOSFET device [40]; (d) Image of CNF strain sensor *(left)* [42]; a full adder *(right)* [40]; (e) Series of images of CNF degradation [40].

2.4.3. Galactomannan

Galactomannans are polysaccharides derived from plant primarily found in the leguminous seeds. Galactomannan films are produced through evaporation method and solvent molding as depicted in FIG. 2.3(a) [45].
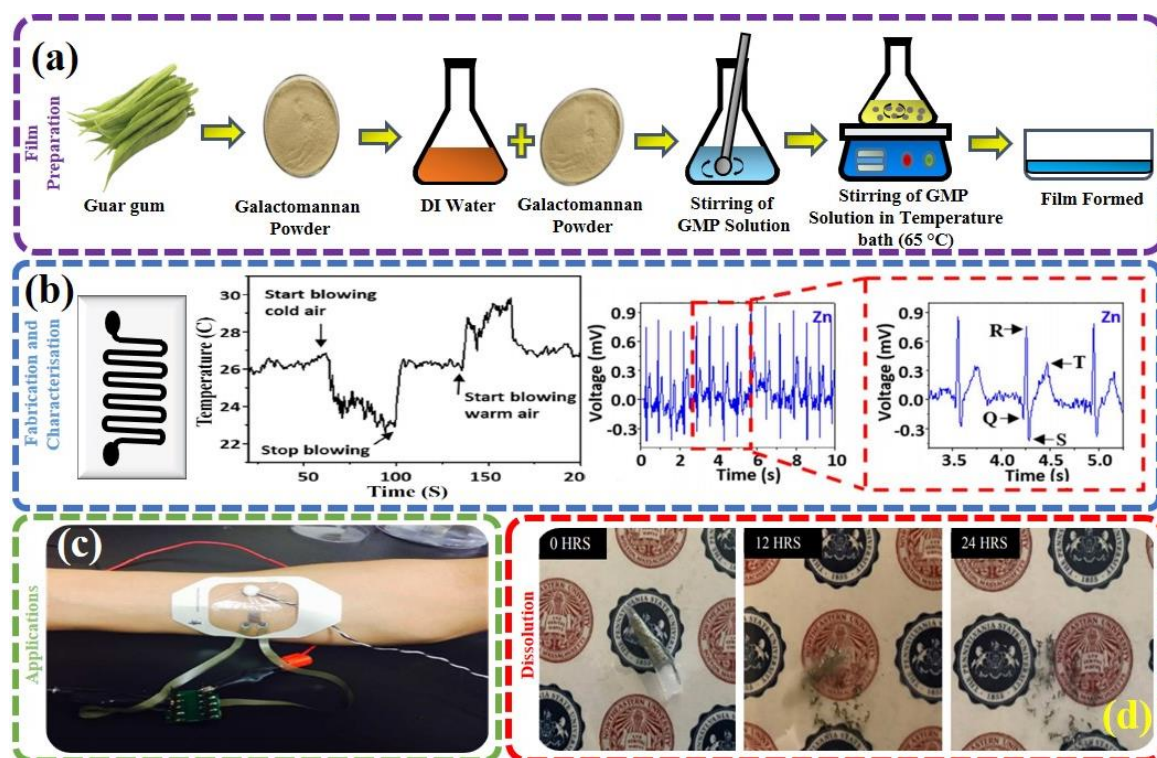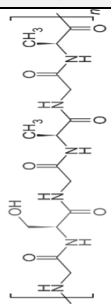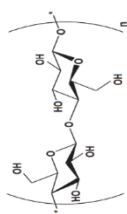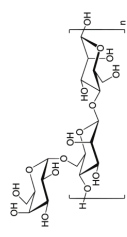
FIG. 2.3. (a) Flowchart outlining the Galactomannan substrate preparation from Guar gum; (b) Galactomannan film based device used as temperature sensor; (c) Temperature measuring setup on-skin; (d) Galactomannan device dissolution in water. (b)-(d) [46].

Yi et al. fabricated a Galactomannan based temperature sensor using Zinc films, as illustrated in FIG. 2.3(b) [46]. The water-soluble, cost-effective, and energy-efficient, on-skin sensor was placed upon hand muscle to monitor ECG, EMG signals as well as body temperature as shown in FIG. 2.3(c).

Galactomannan dissolving mechanism: The polysaccharide Galactomannan contains hydrophilic molecule like glycerol, that makes it water soluble [47]. A Galactomannan device was immersed in DI water to investigate its dissolution behavior. The device dissolved in little time as shown in FIG. 2.3(d) [46]. Table 2.3 presents a comparison of device characteristics of organic transient substrates.

Table 2.3. Characteristics of Organic Transient Substrates

Sl.No.	Substrates	Substrate Thickness	Application	Fabrication Methods	Dissolution medium	Dissolution Mechanism	Chemical Structure of Substrates	Ref.
1	Silk Protein	25 – 60 μm	RRAM/ Motion Sensor/ Electrical circuits	DC Sputtering/ RF Magnetron Sputtering/ Photolithography/Electrospinning/Chemical Vapour Deposition	DI Water: 15 min/ PBS: 5 min/ papain Solution: 24hrs	Proteolytic degradation		[34], [35], [37], [39], [48]
2	Cellulose Nanofibril	200 μm	Strain sensors/ CMOS Device	Stencil Lithography/ Spin Coating	DI Water: 30 min/ Fungi: 60 days	Decomposition		[40], [42], [49]
3	Galactomannan	60 μm	On-skin temperature Sensor/ ECG and EMG signal Monitoring Device	Metal Deposition/ Magnetron Sputtering/ Electron Beam Evaporation	DI water: 24 hrs	Electrostatic and Hydrophobic Interactions		[46]

Reference:

[1]   M. A. Karolina, "Structural and immunologic characterization of bovine, horse and rabbit serum," *Mol Immunol*, vol. 52, pp. 174–182, 2012.

[2]   L. W. Cohen, V. M. Coghlan, and L. C. Dihel, "Cloning and sequencing of papain-encoding cDNA," *Gene*, vol. 48, no. 2–3, pp. 219–227, 1986.

[3]   A. Cstorer and R. Ménard, "[33] Catalytic mechanism in papain family of cysteine peptidases," in *Methods in enzymology*, Elsevier, vol. 244, pp. 486–500, 1994.

[4]   J. Drenth, J. N. Jansonius, R. Koekoek, and B. G. Wolthers, "The structure of papain," *Adv. Protein Chem.*, vol. 25, pp. 79–115, 1971.

[5]   J. Smith and L. Hong-Shum, "Food Additives Data Book pp. 212-214." Blackwell Publishing, 2003.

[6]   R. W. Pickersgill, G. W. Harris, and E. Garman, "Structure of monoclinic papain at 1.60 Å resolution," *Acta Crystallogr. Sect. B Struct. Sci.*, vol. 48, no. 1, pp. 59–67, 1992.

[7]   L. E. Mansfield and C. H. Bowers, "Systemic reaction to papain in a nonoccupational setting," *J. Allergy Clin. Immunol.*, vol. 71, no. 4, pp. 371–374, 1983.

[8]   L.-C. Lv, Q.-Y. Huang, W. Ding, X.-H. Xiao, H.-Y. Zhang, and L.-X. Xiong, "Fish gelatin: The novel potential applications," *J. Funct. Foods*, vol. 63, p. 103581, 2019.

[9]   S. Sultana, M. E. Ali, and M. N. U. Ahamad, "Gelatine, collagen, and single cell proteins as a natural and newly emerging food ingredients," in *Preparation and processing of religious and cultural foods*, Elsevier, 2018, pp. 215–239.

[10]   Z. A. N. Hanani, Y. H. Roos, and J. P. Kerry, "Use and application of gelatin as potential biodegradable packaging materials for food products," *Int. J. Biol. Macromol.*, vol. 71, pp. 94–102, 2014.

[11] A. A. Mariod and H. Fadul, "Gelatin, source, extraction and industrial applications," *Acta Sci. Pol. Technol. Aliment.*, vol. 12, no. 2, pp. 135–147, 2013.

[12] L. S. Kumosa, V. Zetterberg, and J. Schouenborg, "Gelatin promotes rapid restoration of the blood brain barrier after acute brain injury," *Acta Biomater.*, vol. 65, pp. 137–149, 2018.

[13] F. M. Chen and S. Shi, "Principles of tissue engineering." Elsevier: New York, NY, USA, 2014.

[14] K. Ma, X. Cai, Y. Zhou, Y. Wang, and T. Jiang, "In Vitro and In Vivo Evaluation of Tetracycline Loaded Chitosan-Gelatin Nanosphere Coatings for Titanium Surface Functionalization," *Macromol. Biosci.*, vol. 17, no. 2, p. 1600130, 2017.

[15] Y. Shor, T. Tsach, A. Vinokurov, B. Glattstein, E. Landau, and N. Levin, "Lifting shoeprints using gelatin lifters and a hydraulic press," *J. Forensic Sci.*, vol. 48, no. 2, pp. 368–372, 2003.

[16] J.-C. Hwang, C. H. Wang, and C. Y. Hsieh, "OTFT and MIM capacitor using silk protein as dielectric material and methods for manufacturing the same." Google Patents, Mar. 06, 2012.

[17] J.-W. Chang, C.-G. Wang, C.-Y. Huang, T.-D. Tsai, T.-F. Guo, and T.-C. Wen, "Chicken Albumen Dielectrics in Organic Field-Effect Transistors," *Adv. Mater.*, vol. 23, no. 35, pp. 4077–4081, Sep. 2011.

[18] R. Singh, Y.-T. Lin, W.-L. Chuang, and F.-H. Ko, "A new biodegradable gate dielectric material based on keratin protein for organic thin film transistors," *Org. Electron.*, vol. 44, pp. 198–209, 2017.

[19] C. H. Bok, S. J. Woo, C. Wu, J. H. Park, and T. W. Kim, "Flexible bio-memristive devices based on chicken egg albumen: Au@ SiO2 core-shell nanoparticle nanocomposites," *Sci. Rep.*, vol. 7, no. 1, p. 12033, 2017.

[20] B. Qu *et al.*, "Transparent and flexible write-once-read-many (WORM) memory device based on egg albumen," *J. Phys. D. Appl. Phys.*, vol. 50, no. 31, p. 315105, 2017.

[21]   Y.-C. Chen, H.-C. Yu, C.-Y. Huang, W.-L. Chung, S.-L. Wu, and Y.-K. Su, "Nonvolatile bio-memristor fabricated with egg albumen film," *Sci. Rep.*, vol. 5, p. 10022, May 2015.

[22]   N. Raeis-Hosseini, Y. Park, and J. Lee, "Flexible Artificial Synaptic Devices Based on Collagen from Fish Protein with Spike-Timing-Dependent Plasticity," *Adv. Funct. Mater.*, vol. 28, no. 31, p. 1800553, 2018.

[23]   B. Sun, D. Liang, X. Li, and P. Chen, "Nonvolatile bio-memristor fabricated with natural bio-materials from spider silk," *J. Mater. Sci. Mater. Electron.*, vol. 27, no. 4, pp. 3957–3962, 2016.

[24]   L. Wang and D. Wen, "Nonvolatile Bio-Memristor Based on Silkworm Hemolymph Proteins," *Sci. Rep.*, vol. 7, no. 1, p. 17418, 2017.

[25]   M. K. Hota, M. K. Bera, B. Kundu, S. C. Kundu, and C. K. Maiti, "A Natural Silk Fibroin Protein-Based Transparent Bio-Memristor," *Adv. Funct. Mater.*, vol. 22, no. 21, pp. 4493–4499, Nov. 2012.

[26]   N. Gogurla *et al.*, "Transparent and flexible resistive switching memory devices with a very high ON/OFF ratio using gold nanoparticles embedded in a silk protein matrix," *Nanotechnology*, vol. 24, no. 34, p. 345202, 2013.

[27]   X. Ji *et al.*, "Biodegradable and Flexible Resistive Memory for Transient Electronics," *J. Phys. Chem. C*, vol. 122, no. 29, pp. 16909–16915, Jul. 2018.

[28]   H. Wang, B. Zhu, X. Ma, Y. Hao, and X. Chen, "Physically transient resistive switching memory based on silk protein," *Small*, vol. 12, no. 20, pp. 2715–2719, 2016.

[29]   S. Qin, R. Dong, X. Yan, and Q. Du, "A reproducible write–(read)n–erase and multilevel bio-memristor based on DNA molecule," *Org. Electron.*, vol. 22, pp. 147–153, 2015.

[30]   A. A. Grinberg, S. Luryi, M. R. Pinto, and N. L. Schryer, "Space-charge-limited current in a film," *IEEE Trans. Electron Devices*, vol. 36, no. 6, pp. 1162–1170, 1989.

[31] J. G. Hardy, L. M. Römer, and T. R. Scheibel, "Polymeric materials based on silk proteins," *Polymer (Guildf).*, vol. 49, no. 20, pp. 4309–4327, 2008.

[32] H. J. Jin *et al.*, "Water-stable silk films with reduced β-sheet content," *Adv. Funct. Mater.*, vol. 15, no. 8, pp. 1241–1247, 2005.

[33] C. Mukherjee, M. K. Hota, D. Naskar, S. C. Kundu, and C. K. Maiti, "Resistive switching in natural silk fibroin protein-based bio-memristors," *Phys. Status Solidi Appl. Mater. Sci.*, vol. 210, no. 9, pp. 1797–1805, 2013.

[34] C. Hou *et al.*, "A Biodegradable and Stretchable Protein-Based Sensor as Artificial Electronic Skin for Human Motion Detection," *Small*, vol. 15, no. 11, pp. 1–8, 2019.

[35] D.-H. Kim *et al.*, "Silicon electronics on silk as a path to bioresorbable, implantable devices," *Appl. Phys. Lett.*, vol. 95, no. 13, p. 133701, 2009.

[36] A. R. Tripathy *et al.*, "Polymer matrix composite engineering for PDMS based capacitive sensors to achieve high-performance and broad-range pressure sensing," *Appl. Surf. Sci. Adv.*, vol. 3, p. 100062, 2021.

[37] S. Hwang, "A Physically Transient Form of Silicon Electronics," *Sci. AAAS*, vol. 337, p. 1640, 2012.

[38] B. Zhu *et al.*, "Silk fibroin for flexible electronic devices," *Adv. Mater.*, vol. 28, no. 22, pp. 4250–4265, 2016.

[39] F. Song *et al.*, "ZnO-Based Physically Transient and Bioresorbable Memory on Silk Protein," *IEEE Electron Device Lett.*, vol. 39, no. 1, pp. 31–34, 2018.

[40] Y. H. Jung *et al.*, "High-performance green flexible electronics based on biodegradable cellulose nanofibril paper," *Nat. Commun.*, vol. 6, no. May, pp. 1–11, 2015.

[41] H. Zhu *et al.*, "Biodegradable transparent substrates for flexible organic-light-emitting diodes," *Energy Environ. Sci.*, vol. 6, no. 7, pp. 2105–2111, 2013.

[42] L. Meng, S. M. Mahpeykar, Q. Xiong, B. Ahvazi, and X. Wang, "Strain sensors on water-soluble cellulose nanofibril paper by

polydimethylsiloxane (PDMS) stencil lithography," *RSC Adv.*, vol. 6, no. 88, pp. 85427–85433, 2016.

[43]   B. Medronho, A. Romano, M. G. Miguel, L. Stigsson, and B. Lindman, "Rationalizing cellulose (in)solubility: Reviewing basic physicochemical aspects and role of hydrophobic interactions," *Cellulose*, vol. 19, no. 3, pp. 581–587, 2012.

[44]   B. Lindman, G. Karlström, and L. Stigsson, "On the mechanism of dissolution of cellulose," *J. Mol. Liq.*, vol. 156, no. 1, pp. 76–81, 2010.

[45]   N. Zhao, Y. Chai, T. Wang, K. Wang, J. Jiang, and H. yan Yang, "Preparation and physical/chemical modification of galactomannan film for food packaging," *Int. J. Biol. Macromol.*, vol. 137, pp. 1060–1067, 2019.

[46]   N. Yi *et al.*, "Fully Water-Soluble, High-Performance Transient Sensors on a Versatile Galactomannan Substrate Derived from the Endosperm," *ACS Appl. Mater. Interfaces*, vol. 10, no. 43, pp. 36664–36674, 2018.

[47]   V. R. F. Dos Santos, B. W. S. Souza, J. A. Teixeira, A. A. Vicente, and M. A. Cerqueira, "Relationship between galactomannan structure and physicochemical properties of films produced thereof," *J. Food Sci. Technol.*, vol. 52, no. 12, pp. 8292–8299, 2015.

[48]   G. Shen, X. Hu, G. Guan, and L. Wang, "Surface modification and characterisation of silk fibroin fabric produced by the layer-by-layer self-assembly of multilayer alginate/regenerated silk fibroin," *PLoS One*, vol. 10, no. 4, pp. 1–19, 2015.

[49]   P. Phanthong, P. Reubroycharoen, X. Hao, G. Xu, A. Abudula, and G. Guan, "Nanocellulose: Extraction and application," *Carbon Resour. Convers.*, vol. 1, no. 1, pp. 32–43, 2018.

Chapter 3: Fabrication and Characterization Methods

As discussed in the introductory chapter the objective of this dissertation is to study physical, structural and dielectric properties of protein along with their application in charge storage proteotronic devices. This chapter offers an exposition of the protein film deposition technique, elucidating the structural and analytical methodologies employed for investigating the physical attributes of protein films, including their interactions with diverse organic and inorganic substrates as delineated within this dissertation. Succinct introductions to the fundamentals of each analytical method will be presented, accompanied by an account of the instruments and experimental parameters employed in this research.

3.1. Device Fabrication

The device fabrication techniques used in this dissertation are discussed below in order:

3.1.1. Substrate Cleaning

Ensuring the pristinity of the substrate surface prior to material deposition is of utmost significance for achieving the required attributes of the films or nanostructures. The common impurities found on a substrate or wafer typically arise from processes such as scribing/cleaving, the presence of ambient dust, human intervention, bacterial contamination, lint from wiping materials, remnants of photoresist, oil/grease, and residues from cleaning chemicals. Contamination present on the surface of the substrate can lead to a reduced nucleation density of the material, giving rise to various complications such as inadequate adherence of the film or nanostructure to the substrate, diminished repeatability, non-uniform deposition, and suboptimal material properties, among others. Typically, ITO-coated PET and glass substrates may exhibit certain moisture-related contaminations. Thus, the substrates must undergo a preliminary cleaning process before device fabrication. This cleaning process

involves the utilization of established chemical treatment procedures, which are outlined as follows:

i. *Trichloroethylene (TCE)*: TCE is an extensively utilized halogenated aliphatic organic chemical that serves as a versatile degreasing agent. In the event that the substrate is tainted with grease, oil, or a wax stain, it is subjected to a cleaning process involving the use of TCE. The substrates are immersed in a solution of pure TCE for a duration of 5 minutes while being placed under continuous ultrasonication.

ii. *Acetone:* The specimens that have been subjected to TCE cleaning are immersed in an acetone solution for a duration of 5 minutes while being continuously exposed to ultrasonic vibration. The immersion of the substrates in acetone effectively eliminates the residual presence of TCE and additionally facilitates the degreasing process, resulting in further cleansing of the substrates. The significant vapor pressure shown by acetone facilitates expeditious drying, resulting in minimal residue deposition on the surfaces.

iii. *Iso-propyl alcohol (IPA):* Following the acetone cleaning process, it is strongly advised to cleanse the substrates in isopropyl alcohol for a duration of 5 minutes while subjecting them to continuous ultrasonication. The IPA solution effectively eliminates any remaining traces of acetone and also eliminates particulate matter from the substrates.

iv. *De-ionized (DI) water:* DI water is employed in the next step after the aforementioned cleaning procedures to eliminate any remaining IPA solution present on the surface of the substrates. Ultimately, the samples undergo a drying process facilitated by the use of N_2 gas.

Following the chemical cleaning, it's important to make the surface less reactive through exposure to UV light.

3.1.2. Spin Coating

Spin coating is a familiar method of coating thin films evenly over flat surfaces. Spin coating produces a surface that is comparatively flat and uniform

in nature. The process of spin coating is suitable for applying sol-gels. This method entails spinning a solution containing solid particles of a polymer compound dissolved in a solvent onto a substrate's surface. This procedure leads to the creation of a gel-like structure on the substrate's surface, as illustrated in FIG. 3.1. The gel undergoes solidification with the subsequent extraction of the solvent, leading to the formation of a solid film. One notable benefit associated with the spin coating technique for depositing thin films is the high degree of homogeneity achieved in terms of film thickness. Due to the phenomenon of self-levelling, the thicknesses exhibit a negligible variation of no more than 1%. Thicker layers of films may lead to the formation of quite substantial edge beads, which exhibit physical limitations in terms of planarization [1].

The process of spin coating involves casting a solution onto a substrate, then achieving the desired rotation speed. The fluid then levels, begins to thin due to viscous forces, and may change colour. The rate at which the solvent evaporates is influenced by factors like volatility, vapor pressure, and the conditions in the surroundings. The thickness of a film created through spin coating is related to the inverse of the square root of the spinning speed.

$$h_f \propto \frac{1}{\sqrt{\omega}} \tag{3.1}$$
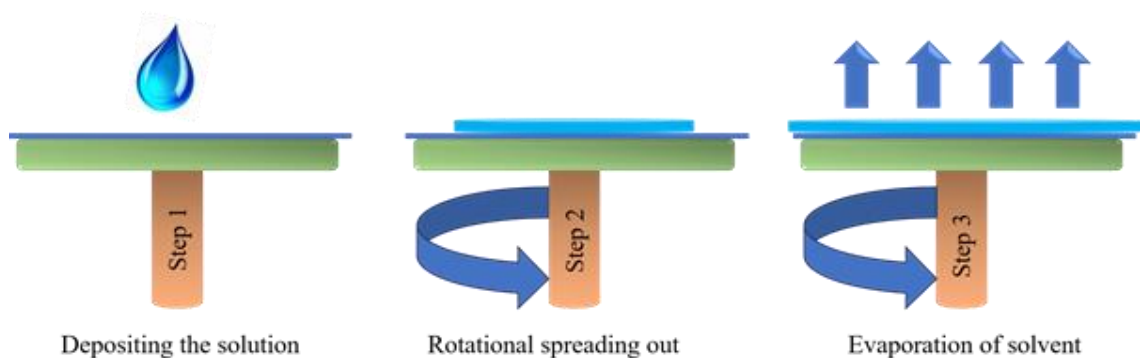
FIG. 3.1. Thin film coating using spin coater.

Dynamic dispense is a precise method that provides improved consistency among different substrates due to less time for solvent evaporation and less critical ramp speed and dispense time. It uses less ink and depends on the

substrate's wetting properties. However, it becomes difficult to achieve substrate coverage with low spin speeds or viscous solutions due to insufficient centripetal force and reduced rotation speed.

3.1.3. Thermal Evaporation

Thermal evaporation stands out as one of the frequently employed methods for depositing films specially metal contacts [2,3]. The process involves, conversion of a solid substance (such as a pure metal, eutectic mixture, or combination) into vapor through the application of high temperatures, followed by the vapor cooling down and turning into a solid colder substrate, resulting in thin film deposition. The process of heating is accomplished by the application of a substantial electric current through a filament, typically designed in the form of a crucible, which possesses a measurable electrical resistance. FIG. 3.2 presents a schematic of the thermal evaporation system. The selection of the filament material is determined by its evaporation temperature and its resistance to alloying or chemical reactions with the evaporant. All filament boats utilized were composed of tungsten material. After the metal has undergone evaporation, its vapor particles engage in collisions with the gas molecules present in the evaporation chamber. During the process of transferring via the ambient gas, a fraction of particles becomes dispersed within a specific distance. At a temperature of 25 °C, the mean free path for air is estimated to be around 45 cm when the pressure is at $1e^{-4}$ torr. However, when the pressure decreases to $1e^{-6}$ torr, the mean free path increases significantly to approximately 4500 cm. Hence, in order to achieve a predominantly linear trajectory for the majority of evaporated substances and maintain a substrate-to-source separation of around 10 to 50 cm within a vacuum chamber, it is imperative to maintain pressures below $1e^{-5}$ torr. A high-quality vacuum is essential for generating deposits that are free from contaminants. The determination of the ratio of deposited material between the crystal detector and the substrate is important due to the presence of a lateral space between these two surfaces in the context of in-situ monitoring of the films. The ratio referred to as the "tooling factor" (with a value of 1.71 for Aluminum) is

a distinct parameter specific to a given evaporator. It is influenced by various factors, including as the dimensions of the system and the specific evaporant being used. Unless explicitly mentioned, a base pressure of less than $2e^{-6}$ torr was ensured before initiating each evaporation process.
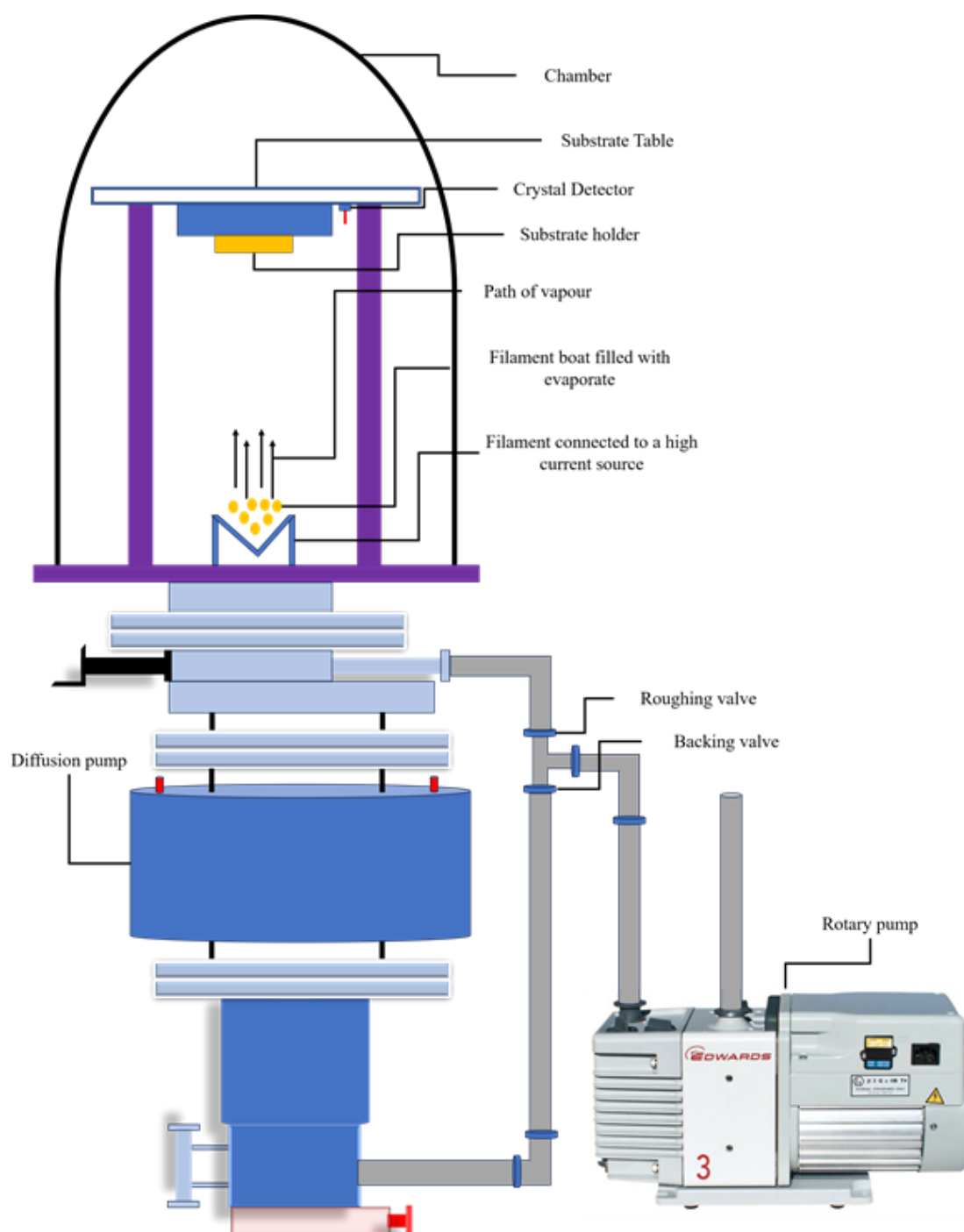
FIG. 3.2. Illustration of thermal evaporation system.

3.2. Sample Characterization techniques

The device characterization techniques used in this dissertation are divided into 3 categories viz. morphological, structural and electrical.

3.2.1 Morphological Study

The morphological study reveals information about the surface of the films used in the current works. The devices used for morphological studies are discussed as below:

3.2.1.1. Optical Microscope

Contemporary compound microscopes employ a dual-stage magnification configuration, wherein the main imaging lens, known as the objective, is linked to a secondary visualizing lens system, commonly referred to as the eyepiece or ocular. These components are positioned at opposing extremities of a body tube [4]. The primary function of the objective lens is to produce the initial image at different magnification levels, the eyepiece serves the purpose of observing the image generated by the objective lens. Sophisticated microscopes feature infinity optical systems that enable the projection of a parallel bundle of wavefronts from the rear aperture of the objective lens. These wavefronts are subsequently focused by a tube or telan lens, leading to the creation of an image at the intermediate image plane within the eyepieces. As a result, the observer can perceive a considerably enlarged virtual representation of the specimen by peering through the eyepieces. FIG. 3.3 shows schematic diagram of optical microscope setup. The determination of magnification involves the multiplication of the objective and eyepiece values [5]. The numerical aperture of a microscope objective quantifies its capacity to collect light and distinguish intricate details in a specimen, which depends on the number of diffracted wavefront patterns it can capture. The perfect point spread function (PSF) represents the three-dimensional diffraction pattern created when light emanates from a tiny point source and travels to the image plane of a microscope.

An optical microscope's design ensures organized light rays are precisely guided, with specimen illumination being a key controllable variable for high-quality images. Köhler illumination, introduced in 1893, optimizes specimen illumination. Microscope objectives, illumination collector, condenser, and eyepieces are essential components for primary image formation.
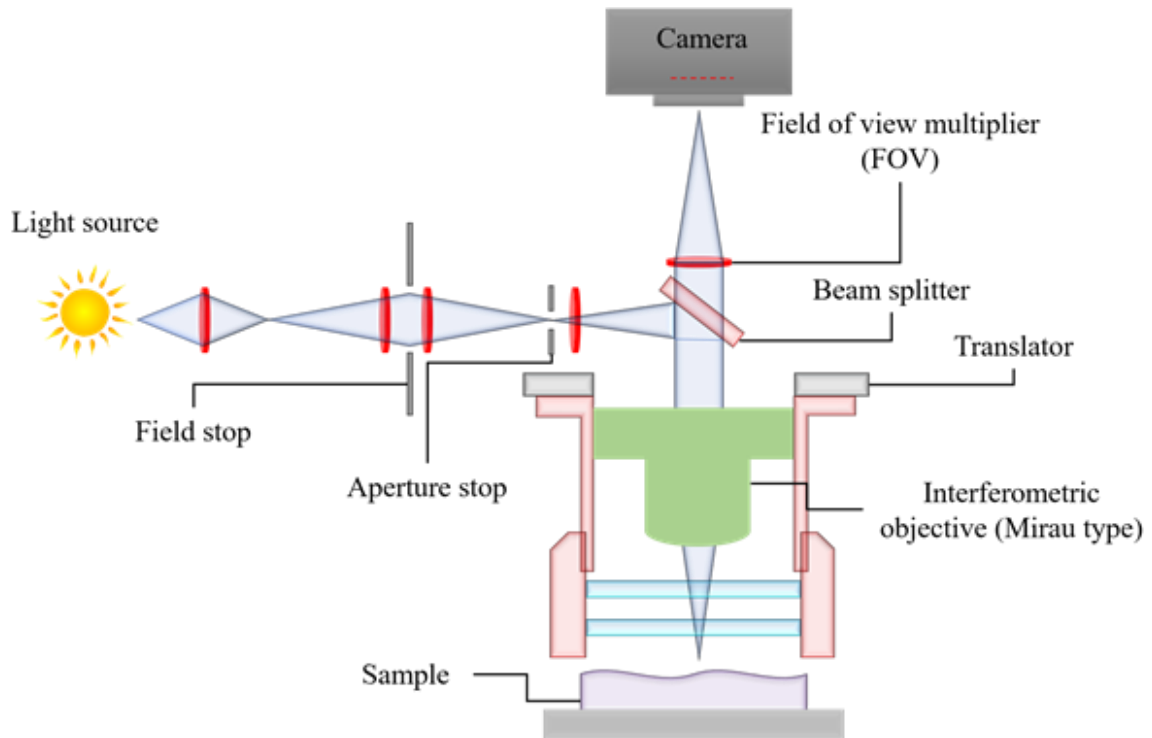
FIG. 3.3. Schematic diagram of optical microscope setup.

3.2.1.2. Field Emission Scanning Electron Microscope

Field Emission Scanning Electron Microscope (FESEM) employs electrons in a zigzag scanning pattern, enabling scientists to observe minute topographical features on surfaces or complete objects. This technique is used in the fields of biology, chemistry, and physics, for observing structures as minuscule as 1 nanometer in size. Prior to being viewed with a scanning electron microscope (SEM), objects must undergo a process to render them conductive for the flow of electric current. The procedure entails depositing an extremely thin layer (measuring between 1.5 and 3.0 nanometers) of either gold or a gold-palladium alloy onto the surface. Moreover, it is imperative that items have the capability to withstand the elevated levels of vacuum and refrain from causing any alterations

to the vacuum environment, such as the release of water molecules or gases. Metals, polymers, and crystals typically remain unaltered and retain their structural integrity when subjected to scanning electron microscopy (SEM) [6].

FESEM employ a cold source, featuring a slender, finely pointed tungsten needle as the cathode, and an applied voltage (0.5-30 KV). The electron beam generated is approximately 1000 times finer, resulting in superior image quality. To concentrate the electron beam, electromagnetic lenses and column apertures are utilized, directing it to a minute, sharp focal point. The size of the electron beam is influenced by the current within the condenser, with lower current yielding a smaller diameter and higher current resulting in a larger beam. A narrow beam offers enhanced resolution but sacrifices signal-to-noise ratio. The condenser lens is composed of two components, with scan coils deflecting electron beams in a zigzag pattern, thus creating synchronized images on the monitor. Schematic diagram of a FESEM is shown in FIG. 3.4.

The objective lens directs the electron beam towards an object, exerting increased force when positioned at a close working distance. This yields the smallest beam diameter, leading to superior resolution but limited depth of field. Stigmator coils rectify deviations or abnormalities in beam deflection for a perfectly round-shaped beam, while ellipsoidal beams cause blurred and stretched images.
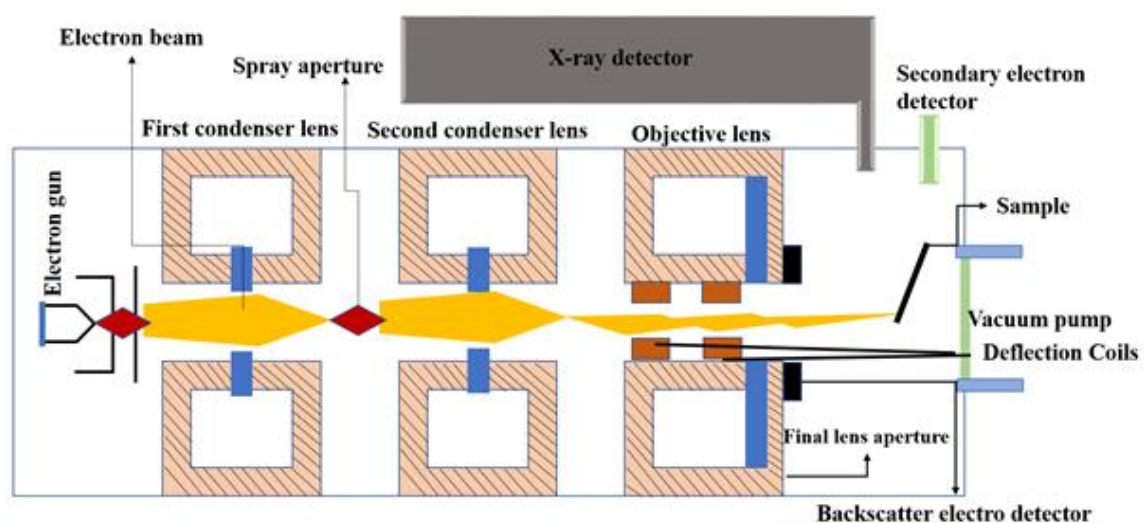
FIG. 3.4. Schematic diagram of FESEM setup.

The specimen is coated with a conductive material and secured onto a specialized holder. It is then placed within a high vacuum chamber and affixed to an adjustable stage. The object can be repositioned using a joy stick, tilted, rotated, or shifted in Z direction. A secondary electron emission detector, is positioned behind the specimen holder. When the primary probe interacts with the specimen, it generates secondary electrons that possess a defined velocity. These electrons are drawn towards the Corona and collide with the scintillator, resulting in the emission of photons. The signal is then converted into a video signal with proper amplification, which is sent to a cathode ray tube. The variations in contrast within real-time image depict the surface structure of the specimen.

3.2.1.3. Atomic Force Microscope

Atomic force microscopy (AFM) is a form of scanning probe microscopy that serves as a valuable tool for characterizing surface topography [7]. It employs a fine-tipped probe to traverse a surface, concurrently monitoring the tip and the sample interaction. Surface roughness assessments were conducted utilizing tapping mode AFM. Tapping mode AFM, denoted as TM-AFM, enables the high-resolution measurement of surface morphology and depends on the size of the cantilever used. These probes typically possess a resonance frequency of 325 kHz and 40 N/m force constant. The scanning dimensions employed in this study are 5 µm × 5 µm, and the resolution limit achieved is below 1 nm.

FIG. 3.5 illustrates a schematic of a standard commercial AFM instrument. As the cantilever gets closer to the object, the interaction between the atoms on the sample's surface and cantilever's edge induces a deflection in the cantilever. The bending of the cantilever is detected using a laser and a photodiode, providing data about the tip's height above the sample surface. The cantilever's position is regulated by a feedback circuit in the z-direction, while scanning in the x-y directions produces a topographical image of the surface.

Atomic Force Microscopy (AFM) can be operated in three primary modes: tapping mode, noncontact mode, and contact mode. In tapping mode, a

piezoelectric device induces vibrations in the cantilever, while the probe makes partial contact with the sample at a portion of the vibrational cycle. Tapping mode frequently allows for higher-resolution surface morphology measurements compared to the other modes and reduces the chance of sample damage.
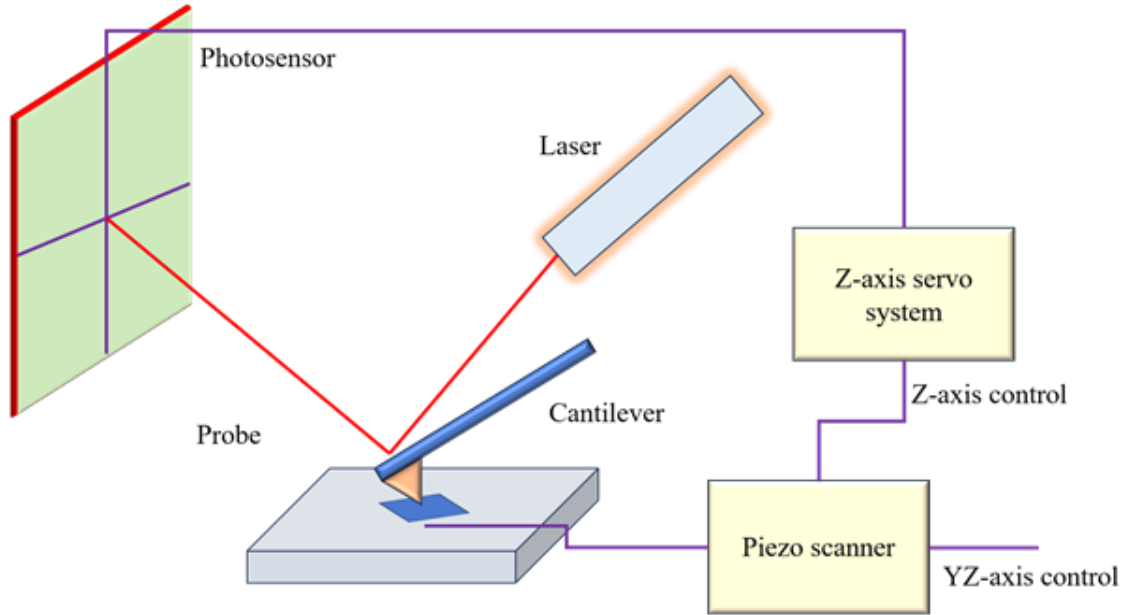
FIG. 3.5. Configuration of an Atomic Force Microscopy (AFM) system.

To assess the surface roughness, a surface image is generated through scanning along the x-y directions. Surface roughness is quantified using parameters such as R_{MAX}, which represents the disparity between the highest and lowest surface points, and the root mean square roughness (r.m.s.). Within a specific scanning area, the standard deviation of the height values is expressed as follows:

$$RMS = \sqrt{\frac{\sum_{i=1}^{N}(Z_i - Z_{avg})^2}{N}} \tag{3.2}$$

where, Z_{ave} denotes the mean Z value within the specified area, Z_i represents the present Z value, and N signifies the count of points within the designated area.

When conducting AFM measurements, it's crucial to utilize top-notch, long-lasting, and finely pointed tips. Using worn-out tips can yield entirely

distorted images, and the acquired roughness data becomes unreliable. Additionally, it's essential to steer clear of employing multiple tips for imaging purposes.

3.2.1.4. Contact Angle Goniometer

The contact angle provides insight into the degree of surface wetting exhibited by a liquid [8]. The magnitude of a contact angle can vary, contingent upon the specific physical characteristics of the materials under investigation. The phenomenon of droplet spreading is commonly referred to as "wetting," whereby a droplet can exhibit either wetting or dewetting behavior upon contact with a surface. The surface tension of a droplet is determined by the interactions that occur between the molecules composing it. Within the majority of the droplet, molecules experience intermolecular forces that exert equal influence from all directions. The intermolecular forces between surface molecules are comparatively stronger than those between bulk molecules due to the absence of forces exerted from all directions. This implies that the resistance encountered by an object in penetrating the surface is greater compared to the resistance experienced by an object in motion inside the bulk after submersion [9].

The process consists of two primary phases: data acquisition and subsequent analysis. The apparatus necessary for conducting a contact angle measurement is depicted in FIG. 3.6. It comprises of three fundamental components: a light source, a camera, and a tilting stage. The stage is designed to be flat to prevent any displacement of the liquid droplet during deposition. A liquid droplet is placed onto the stage, illuminated from behind, and an image is captured by the camera.

When designing the optical components of a measurement system, several factors must be considered. Image size is of paramount importance as it encompasses the entire droplet, and a blurry or indistinct edge can hinder the observation of its slope and the solid surface. Clarity can be influenced by various

factors such as camera resolution, image magnification, light intensity, and the contrast with the background. Excessive pixelation can complicate the identification of the droplet's boundary. Image magnification has a bearing on the level of detail that can be discerned, while inadequate contrast can make it challenging to distinguish the droplet from its surroundings. Light levels can also impact the measurement process. It is crucial for the imaging system's depth of field to be correctly adjusted to ensure that the baseline can be accurately determined even through the blurry front of the droplet.

The baseline corresponds to the solid surface upon which the droplet is placed, and the contact angle signifies the angle formed where this baseline intersects with the edge of the droplet. The determination of the droplet's edge can be accomplished through manual delineation, automated detection using software, or estimation based on standard droplet configurations. The contact angle is calculated using the baseline and gradient as soon as the image is obtained using trigonometrical relation **tan(θ) = (opposite/adjacent)**.
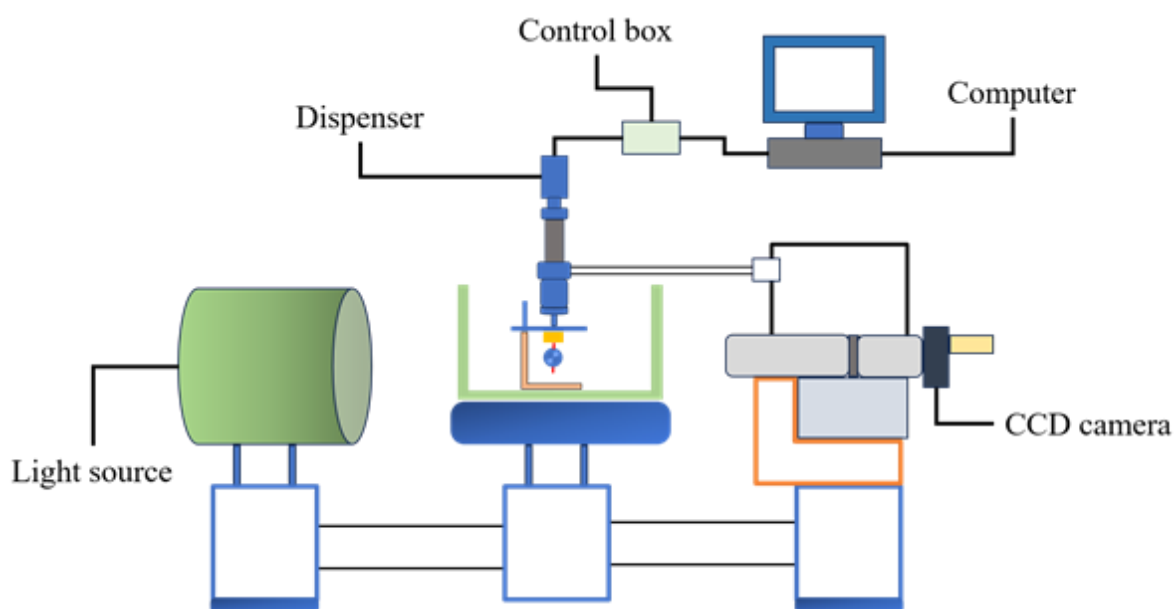
FIG. 3.6. Schematic of Contact angle goniometer setup.

3.2.2 Structural characterizations

The structural characterizations provide information about the chemical bonds and the molecular structure of the material. The instruments used for this purpose are discussed briefly below:

3.2.2.1. Fourier Transform Infrared Attenuated Total Reflectance Spectroscopy

Fourier Transform Infrared Spectroscopy is a method of characterizing structural property of a material in all infrared frequencies at a very high speed [10, 11]. The functioning principle of an attenuated total reflection involves the detection of alterations in an infrared beam that undergoes total internal reflection upon interaction with a sample, as depicted in FIG. 3.7. An infrared beam is focussed towards a high refractive index crystal at a particular angle, causing internal reflection. This gives rise to an evanescent wave, which extends past the crystal's surface to the sample attached. An evanescent wave can be conceptualized as an infrared bubble that resides on the crystal's surface, facilitating a simplified understanding of its nature. The evanescent wave extends only a short distance, typically ranging from 0.5 µm to 5 µm, beyond the crystal's surface and enters the sample. Thus, it's crucial to ensure effective contact between the crystal's surface and the sample. In specific spectral bands within the infrared range where the energy is absorbed by the sample, the evanescent wave experiences attenuation or alteration. The energy that each evanescent wave loses is subsequently returned to the infrared (IR) beam. Then this beam from the other end of the crystal is pointed towards the IR detector. As a result, infrared spectrum is generated by the system. In order to ensure proper interaction, it is imperative that the sample is in direct physical contact with the ATR crystal. This requirement arises from the limited extent of the evanescent wave or bubble, which extends beyond the crystal by a range of 0.5 µm to 5 µm. For internal reflectance to occur in the crystal, it is important that the crystal refractive index is notably high than refractive index of the sample. Otherwise, the light will be transmitted through the crystal instead of being internally reflected. ATR crystals generally exhibit

refractive index values ranging from 2.4 to 4.0 when measured at a wavenumber of 2000 cm^{-1}.
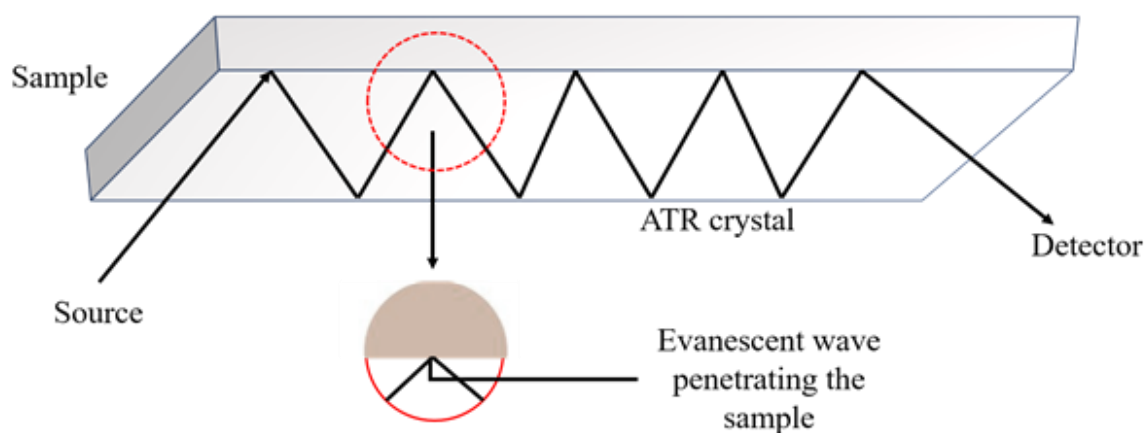
FIG. 3.7. Schematic of FTIR-ATR measurement.

The equipment utilizes an interferometer to divide the incoming beam into signals with distinct infrared frequencies. The frequency spectrum acquired subsequent to measurement is decoded using Fourier transformation. To create a comparative scale for the absorption intensity, it is essential to record a background spectrum alongside it. Typically, this measurement does not include the presence of a sample within the beam. This can be likened to the process of measuring the "percent transmittance" by utilizing a sample placed within a beam.

3.2.2.2. Raman spectroscopy

Raman spectroscopy a part of molecular spectroscopy that uses the relation between light and substance, is used to acquire knowledge about the composition or properties of a material, similar to Fourier-transform infrared spectroscopy (FTIR). The data obtained through Raman spectroscopy is derived from a phenomenon of light scattering, on the other hand, infrared (IR) spectroscopy relies on the absorption of light [12]. Raman spectroscopy enables the acquisition of data pertaining to both intra- and inter-molecular vibrations, hence offering supplementary insights into the properties of the substance under investigation. Both Raman and Fourier Transform Infrared (FTIR) spectroscopy techniques yield

spectra that capture unique vibrational patterns of a molecule, often referred to as its "molecular fingerprint." These spectroscopic methods are highly useful in substance identification. Nevertheless, Raman spectroscopy has the capability to provide supplementary data pertaining to lower frequency modes, as well as vibrations that offer valuable insights into the structural framework of a molecule.

When photons of light interact with molecules in a solid, liquid, or gases, majority of them experience scattering, maintaining the same energy as the photons that initially interacted with them. The phenomenon being referred to is commonly known as elastic scattering, or more specifically, Rayleigh scattering. A minute proportion of these photons, roughly one photon in ten million, will undergo scattering at a distinct frequency from that of the incoming photon. The phenomenon under discussion is commonly referred to as inelastic scattering, or more specifically, the Raman effect, which was named in honor of its discoverer, Sir C.V. Raman. When the scattered light has diminished energy than the incident light, the incident radiation imparts some of its energy to the molecule. This leads to a reduction in the energy of the scattering. The incident is commonly known as Stokes Raman scattering. When the scattered radiation energy is more than that of the incident radiation, the incident radiation absorbs a portion of the molecule's vibrational/rotational energy, resulting in the scattered radiation possessing higher energy. This phenomenon can also be denoted as Anti-Stokes Raman scattering. The schematic diagram of Raman spectroscopy instrument is illustrated in FIG. 3.8.

Raman spectroscopy uses laser as a light source, with the spectrum's radiation varying based on the laser's bandwidth. A filter separates Raman scattered light from Rayleigh scattered light for high-quality spectra. LCD array detectors are used in modern Raman spectrometers to detect signals of different wavelengths and weak signals. A compatible computer aids in drawing the final Raman spectroscopy graph/spectrum.
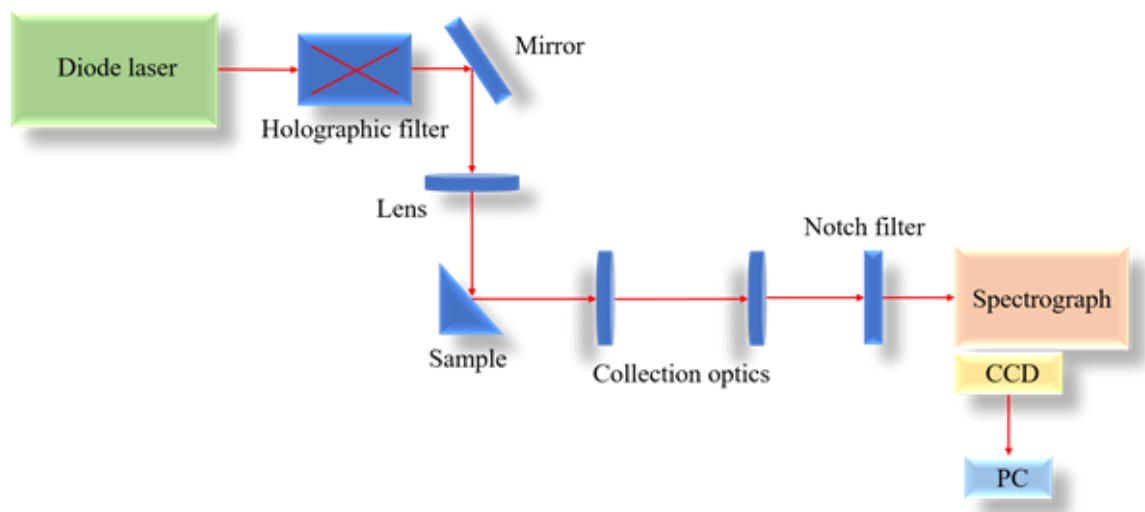
FIG. 3.8. Schematic of Raman spectroscopy instrument.

3.2.2.3. Inelastic Electron Tunneling Spectroscopy (IETS)

Inelastic electron tunneling spectroscopy (IETS) is a method that has demonstrated remarkable sensitivity and precision when investigating the molecules' vibrational spectra attached to the surface of an insulator within junction of a metal-insulator-metal tunnel structure [13,14]. FIG. 3.9 shows schematic diagram of inelastic electron tunneling spectroscopy instrument. It is based on the physical phenomenon of inelastic contact between a tunneling electron and a molecule that has been adsorbed onto a surface. The spectral analysis technique can be employed for the purpose of identifying the chemical entities present on the dielectric surface. Electron's wave function originating from a particular metal has the capability to extend onto the adjacent insulating layer. The phenomenon of electron tunneling occurs when electrons are able to go through an insulating material, thereby establishing a connection between two metal electrodes. The phenomenon described can manifest in two ways: elastic tunneling, where no energy is lost, or inelastic tunneling, where energy is transferred to fundamental excitations of the molecules located within the insulating layer. Utilizing inelastic electron tunneling spectroscopy proves to be a

valuable approach for studying the vibrational modes displayed by molecules adhering to insulating layers within a metal-insulator-metal tunnel junction. The data provides valuable insights into the characteristics pertaining to the arrangement, chemical bonding, and spatial alignment of molecules that have undergone adsorption. A significant advantage of inelastic electron tunneling spectroscopy lies in its exceptional sensitivity.

The device exhibits the ability to detect a range of 1-10 molecules, this corresponds to a fraction of a single layer of molecules on a junction that spans 1 square millimeter in size. In the context of IETS, a thin layer of oxide is interposed between two metallic plates, with the presence of adsorbed molecules on its surface. A bias voltage is employed across the two contacts. An illustrative depiction of the energy levels within the metal-oxide-metal device, when subjected to an applied bias is acquired. A subset of the electrons involved in tunneling phenomena have the potential to dissipate energy through the process of activating vibrations within the oxide or the adsorbate. The occurrence of these inelastic processes results in the emergence of a secondary tunneling pathway, so contributing an extra current component to the overall tunneling current. Following the occurrence of the incident electron, it is vital for the electron to possess a sufficient amount of energy in order to induce the excitation of this particular vibration. Consequently, a minimum energy threshold is established, marking the initiation of this inelastic process. The observed phenomenon can be classified as a vibronic condition. The minimal energy required for the electron is associated with a minimum bias voltage, which marks the initiation of the supplementary contribution. The amplitude of the inelastic current is quite small, in comparison to the elastic tunneling current, amounting to approximately 0.1%.
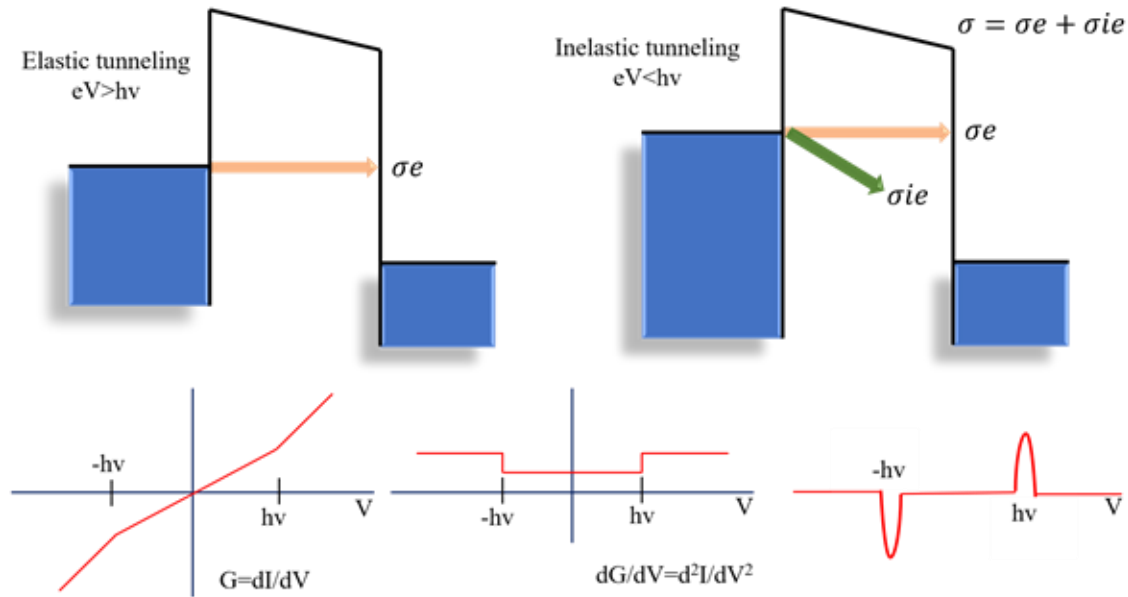
FIG. 3.9. Schematic diagram of Inelastic electron tunneling spectroscopy measurement.

3.2.2.4. X-ray photoelectron spectroscopy (XPS)

X-ray photoelectron spectroscopy (XPS), is a technique of spectroscopy used for its quantitative capabilities. It offers important attributes of the chemical state, elemental composition, and electronic structure, in the near-surface region of a material, typically at a depth of less than 5 nm [15,16]. The concept under consideration traces its roots back to the initial observation of the Hertz's photoelectric effect. Subsequently, Einstein provided a more accurate and detailed characterization of its energetic properties. Further advancements in this field were made by Robinson and Rawlinson, who conducted research on X-ray photoelectron spectra pertaining to various metallic substances. Currently, XPS offers significant insights into the electrical structure, chemical composition, and surface stoichiometry of a given sample.
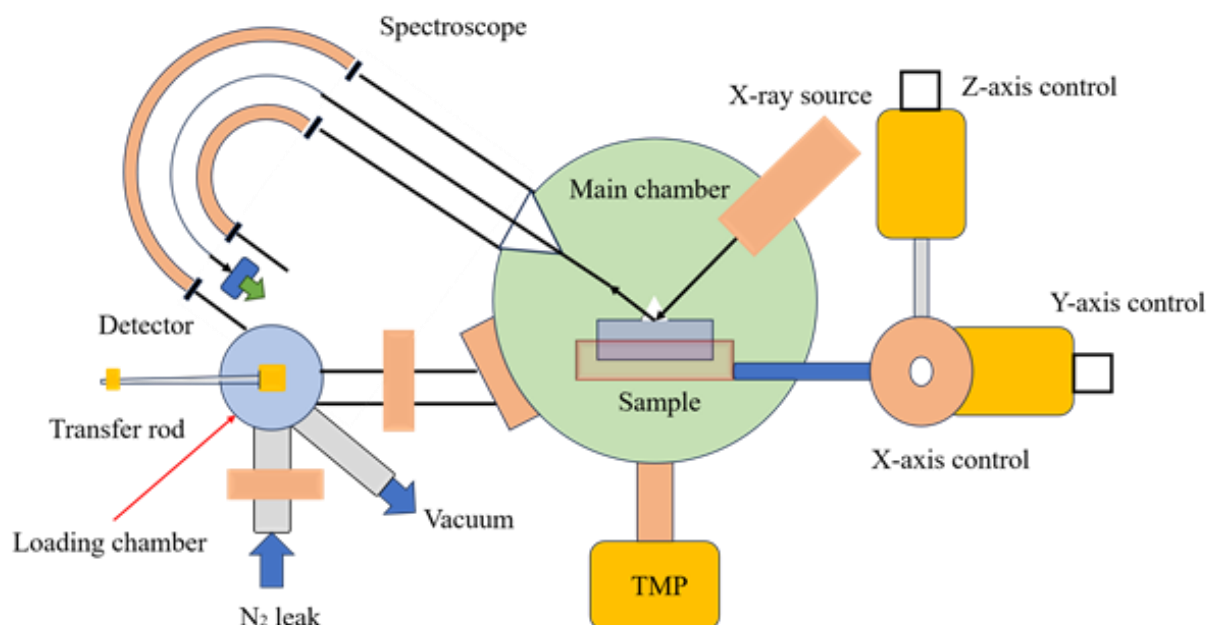
FIG. 3.10. Illustration representing the configuration of XPS apparatus.

XPS involves exposing a material to soft X-rays in a vacuum environment. The schematic diagram of the instrument is shown in FIG. 3.10. It studies both kinetic energy as well as the no of electrons escaping from the materials topmost atomic layer. This process demands extremely high vacuum conditions and chamber pressures in the range of 10^{-9} to 10^{-10} Torr. The X-ray can have energies up to 10 keV, and as it interacts with atoms, it primarily affects orbital electrons through photon absorption. Commonly used X-ray sources include monochromatic aluminum K-alpha X-rays and non-monochromatic magnesium K-alpha X-rays, with aluminum X-rays offering superior energy resolution. For even higher energy resolution, researchers employ intense and narrowly defined synchrotron radiation. It's important to note that in XPS, only electrons from the material's surface or the immediately below few layers of atom can escape and reach the detector. This characteristic makes XPS a surface-sensitive technique owing to the extremely limited mean free path length of electrons in solids.
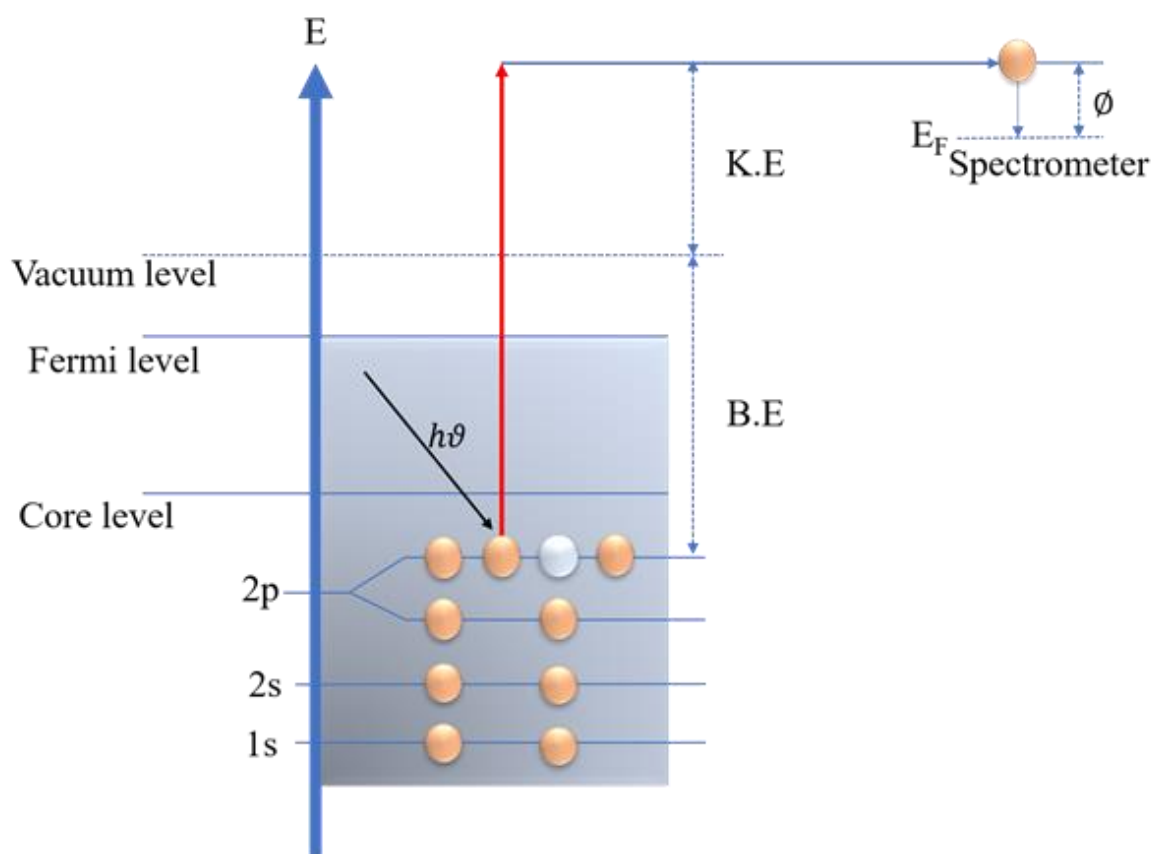
FIG. 3.11. Physical illustration of XPS method.

FIG. 3.11 presents a graphical representation of the electronic transition inherent in XPS. Initially, an incident X-ray photon expels an electron from one of the electronic levels at the core. The emitted core electron has kinetic energy (KE) given by:

$$KE = h\upsilon - BE - \phi \qquad (3.3)$$

In this equation, hυ represents the incoming X-ray energy, BE corresponds to atomic orbital binding energy, while "φ" signifies work function.

XPS spectra are employed to identify and quantify the presence of elements on the surface by utilizing their distinctive binding energies. Core-level electron binding energy is influenced by atoms' surroundings. Binding energies in different compounds can vary due to factors like oxidation state, molecular environment, and lattice parameters. These variations, recognized as chemical

shifts, aid in discerning the oxidation states of the examined substances. The change in binding energy can be mathematically represented as follows:

$$\Delta BE = BE - BE_0 = IA + EA \tag{3.4}$$

In this equation, *BE₀* represents the core-level electron binding energy in an isolated atom. The component known as the intra-atomic part IA can be expressed in relation to the effective charge of the atom, as *IA=Kq*, where *K* is a constant specific to the chemical element. The other component, referred to as the extra-atomic part EA, signifies the potential energy stemming from the surrounding environment, often termed the Madelung potential. Identifying the chemical states of an atom relies on precise measurements of positions of the peaks and their corresponding shifts.

3.2.3. Optical characterization

The optical characterization is performed to get insight about the band gap and defect states present in the materials. The instruments used in optical studies are discussed below:

3.2.3.1. UV-Vis spectrophotometer

The spectrometer system utilizing ultraviolet-visible-near infrared (UV-VIS-NIR) electromagnetic radiation is employed to quantify the light intensity (I) transmitted through a sample with a given thickness (d), and afterwards compare it to the initial intensity (I₀) of the input light [17]. The transmittance, denoted as 'T,' is defined as the ratio of 'I' to 'I₀', and is often represented as a percentage number (%). The spectrophotometer commonly utilizes different light sources to cover a range of wavelengths. These sources include a tungsten lamp, (300 nm-2500 nm). In case of ultraviolet (UV) range specifically, a Deuterium arc lamp is employed, covering the wavelength range of 190 nm to 400 nm. Alternatively, a Xenon arc lamp is used to cover the whole UV to near infrared (NIR) region,

spanning from 160 nm to 2000 nm. A monochromator is utilized to establish a certain wavelength of light and is synchronized with the readout circuit or computer system. The collected light that traverses the sample is captured by a circuit consisting of a detector, and afterwards transmitted to the computer. The transmittance T is recorded at each instance when the wavelength of the light is altered. FIG. 3.12 illustrates the schematic diagram outlining the functioning principles of the spectrophotometer. The analysis of the transmitted light through the sample, which is dependent on the wavelength, yields crucial insights into the physical characteristics of a certain material, including its energy band gap and absorption coefficient (α). α of the material for a particular wavelength, can be obtained by Beer-Lambert Law as [18]:

$$I = I_0 e^{-\alpha d} \tag{3.5}$$

$$\alpha = -\frac{\ln(T)}{d} \tag{3.6}$$

$$\alpha = (Ah\nu)\left(h\nu - E_g\right)^m \tag{3.7}$$

The optical absorption coefficient, *a*, is also given by the Tauc's relation in equation (3.7), where, *A* is constant, *d* is the sample thickness, *h* is Plank's constant, *ν*, I_o is initial intensity of the light, *I* is intensity of light after passing through the sample, Eg is the bandgap of the sample, and exponent *m* signifies the nature of transition whose values are as follows:

(a) m= 1/2 in case of direct allowed transitions;

(b) m= 3/2 in case of direct forbidden transitions;

(c) m= 2 in case of indirect allowed transitions;

(d) m= 3 in case of indirect forbidden transitions.
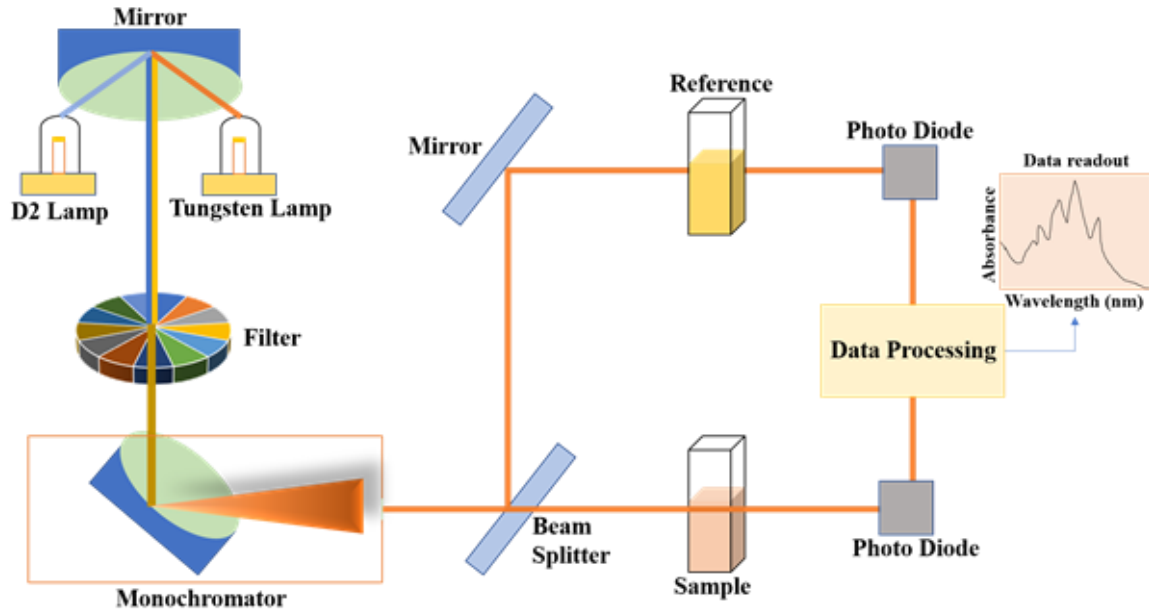
FIG. 3.12. Schematic diagram showing UV-Vis Spectrophotometer set-up.

3.2.3.2. Photoluminescence (PL)

Photoluminescence (PL) is an optical spectroscopic technique that is utilized for the characterization of semiconductor materials in a non-destructive manner [19,20]. The procedure entails stimulating carriers to move between two energy bands present in materials. The necessary stimulating energy for the carriers is supplied by a LASER beam or a monochromatic light source possessing an excitation energy surpassing the band gap of the material. Following the photo-excitation of carriers, a series of relaxation or recombination events take place, resulting in the emission of secondary photons. The duration of the relaxing process across distinct energy levels inside the forbidden band may exhibit variation.

Photomultiplier tubes are used to scan emitted photons that possess varying energy and wavelengths. Each peak noticed in the intensities can be attributed to a certain energy level or band, which is determined by their Full Width at Half Maximum i.e. FWHM. FIG. 3.13 displays the illustration of the PL system utilized in the present study. The luminescence spectra exhibit two prominent peaks: a near band edge (NBE) emission, associated with the

recombination of excitons, and a broad deep level emission (DLE), indicating the existence of defects. Photoluminescence (PL) spectroscopy proves to be a valuable method for exploring various characteristics of semiconductors. These include properties such as the band gap, impurity and defect levels, and the processes governing recombination.
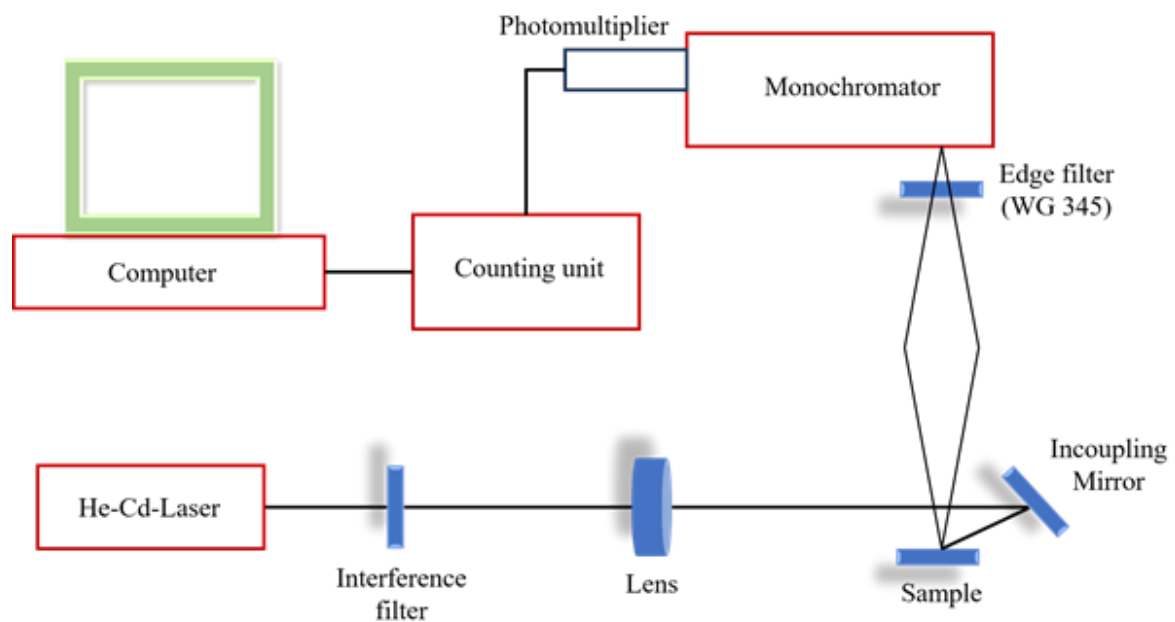
FIG. 3.13. Schematic diagram showing Photoluminescence set-up.

3.2.4. Mechanical characterization

The behavior of the material can be assessed by several testing methodologies, utilizing specialized testing apparatus. The Universal Testing Machine (UTM) (as shown in FIG. 3.14) is employed to determine the mechanical characteristics, such as tensile, compressive, and transverse stresses, of a specified test sample by applying forces in the form of tension, compression, or transverse loading [21]. The nomenclature of the machine is derived from its capacity to conduct a diverse array of tests on various types of materials. The procedures and application of a particular system are comprehensively described in a testing methodology, frequently disseminated by a recognized standards body.
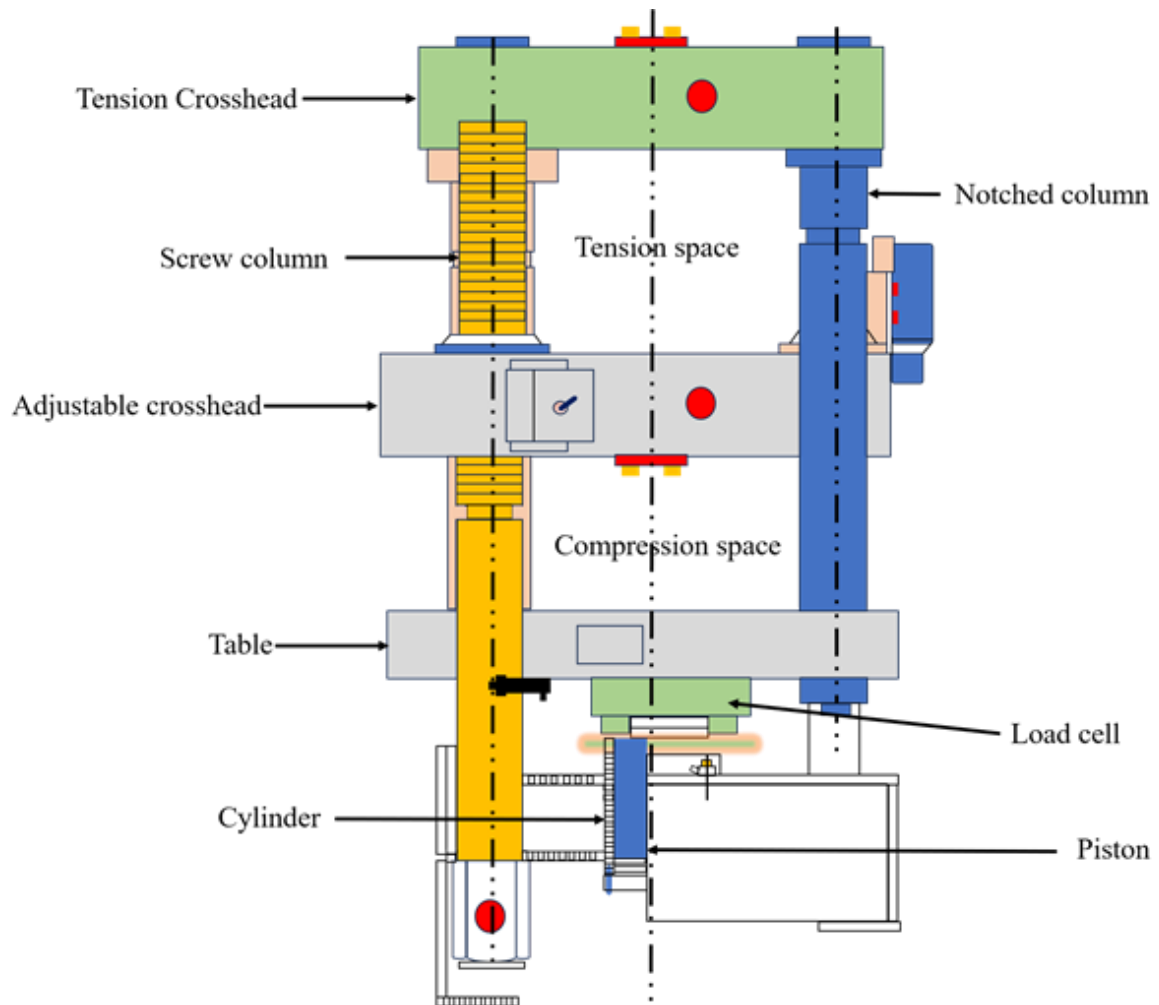
FIG. 3.14. Schematic diagram of Universal testing machine.

The universal testing machine is equipped with a pair of vertical threaded shafts, upon which the movable crosshead is designed to smoothly traverse. The crosshead will remain consistent. The two heads will be equipped with locking clamps in order to secure the specimen in position. Examples of materials commonly used for tensile testing include wires and rods. For a tensile test, the object is kept between the cross head and movable head jaws. In the case of a compressive test, the sample is positioned between the movable head and the table. A speed controller is employed to manage the rotational speed of two vertically oriented threaded shafts. Consequently, this adjustment induces a modification in the applied load on the specimen, facilitated by the adjustable crosshead. By utilizing the loading dial indicator, one is able to ascertain the magnitude of the imposed load on the specimen during the testing process.

After the initiation of the machine, it proceeds to exert a progressively escalating force on the specimen. During the experimental trials, the control system and its corresponding software document the load applied to the specimen, as well as its extension or compression. Machines exhibit a wide spectrum of sizes, ranging from compact table top systems to those with capacities exceeding 53 MN (12 million lbf). A Universal Testing Machine (UTM) can be utilized to perform a range of tests, including the bend test, friction test, peel test, flexural test, tension test, and spring test.

3.2.5. Electrical characterization

This section explores the primary methods frequently employed for electrically characterizing charge storage devices. Current-voltage and Capacitance-voltage measurement methods are utilized to derive details about dielectric properties and ascertain essential device parameters.

3.2.5.1. Cyclic voltammetry

Voltammetry is the technique of measuring current by varying the potential between two electrodes [22]. Cyclic voltammetry stands as an advanced technique in the realm of voltammetry. During the scanning process, chemical species either undergo oxidation or reduction, depending on the direction of the potential ramp. Cyclic voltammetry relies on a three-electrode cell setup, comprising a reference electrode, a working electrode, and a counter electrode. FIG. 3.15 illustrates the schematic representation of this procedure. While the working electrode potential is adjusted, the potential at the reference electrode is constant, set at a clearly defined value. The current passing through the working electrode is effectively balanced by the current at the counter electrode, which boasts a larger surface area. Furthermore, no current flows between the reference electrode and the working electrode. As electrons are transferred, they lead to the formation of a capacitive double layer referred to as the diffuse double layer on the electrode surface.

The measured response can be given as:

$$i_d = nFAD_0 \left(\frac{\delta C_0}{\delta x} \right)_0 \qquad (3.8)$$

Here, i_d represents the current limited by diffusion, A denotes the electrode's surface area, D_0 stands for the diffusion coefficient of the analyte, and $\left(\frac{\delta C_0}{\delta x} \right)_0$ signifies the concentration gradient at the electrode surface [23].
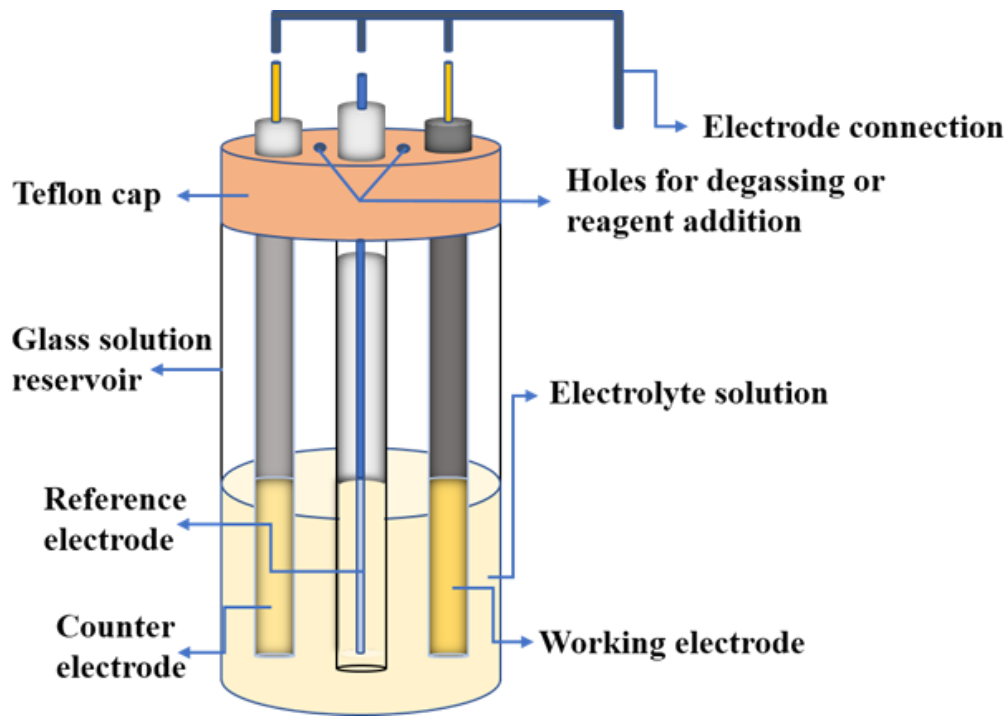
FIG. 3.15. Schematic setup for Cyclic voltammetry.

3.2.5.2. UV sensor measurement

A UV LED cabinet consisting of 280 nm and 232 nm wavelengths, has been used for photo excitation. The sample under test is connected directly to another Keithley source measuring unit for measuring the current-voltage measurements. Prior to measure response of the photodetectors, the calibration was performed which suggests an excellent near UV emission with no visible emission band in the spectra [24].

3.2.5.3. Capacitance-Voltage Characterization

The Capacitance-Voltage (CV) technique is used to study various crucial parameters related to MIM (Metal-Insulator-Metal) devices. For all experiments in this study, CV measurements were conducted with Agilent E4980A LCR meter (schematic shown in FIG. 3.16). In the CV measurement, a direct current bias superimposed with an alternating current signal is applied to the terminals of MIM structure, allowing simultaneous measurement of capacitance and conductance. It's important to note that the added ac signal should be as minimal as possible to avoid interference with the measurement results. By sweeping the gate bias, the capacitance of the MIM capacitor changes as a function of the gate voltage.

The devices are electrically characterized by fabricated ohmic contact on the film. The fabricated device is placed inside a probe station which has four micro-manipulators. Each manipulator has gold (Au)coated tungsten (W) microprobe of tip-diameter ~ 20 µm. The micro-tip connection to metal contacts on such nanostructures is highly sensitive to background vibrations and therefore, the entire setup is placed over a vibration isolation bench. Specially, the junction capacitance-voltage measurement can be performed by varying the A.C. frequency from 100 KHz to 1 MHz. Such measurements are extremely important for investigating the device parameters such as capacitance voltage characteristics, dielectric constant, doping concentration and the presence of interface trap or defect density and so on.

3.2.5.4. Current-Voltage Characterization

The current-voltage measurement (IV) (schematic shown in FIG. 3.16) is a widely used technique for assessing charge storage devices. The direct current-voltage (D.C. IV) characteristics can be assessed using a voltage of 200 µV and a current range spanning from 10 fA to 20 mA, with a measurement speed of 1000 readings per second. Moreover, bias stress and other time-dependent electrical measurements can also be performed with selected speed. It serves to evaluate the dielectric film's quality and delve into aspects related to reliability and dielectric

breakdown. Current flows across the dielectric material by tunneling. There are two well-established tunneling mechanisms, known as direct tunneling (DT) and Fowler-Nordheim (FN) tunnelling. When carriers tunnel across a potential barrier, the FN tunneling prevails, and it is expressed as follows:

$$J_{Fn} = A_G E_{ox}^2 \exp\left(\frac{-B}{E_{ox}}\right) \tag{3.9}$$

where $A = \dfrac{q^3\left(\dfrac{m}{m_{ox}}\right)}{8\pi h \Phi_B}$ and $B = \dfrac{8\pi\sqrt{2m_{OX}\Phi_B^3}}{3qh}$

The Fowler-Nordheim (FN) tunneling current experiences exponential growth as the applied field intensifies. When current conduction transpires across a trapezoidal barrier, the primary tunneling mechanism is direct tunneling, and its relation can be described as follows:

$$J_{DT} = A_G E_{OX}^2 \exp\left[\frac{-B\left[1-1\dfrac{qV_{OX}}{\Phi_B}\right]^{\frac{3}{2}}}{E_{ox}}\right] \tag{3.10}$$
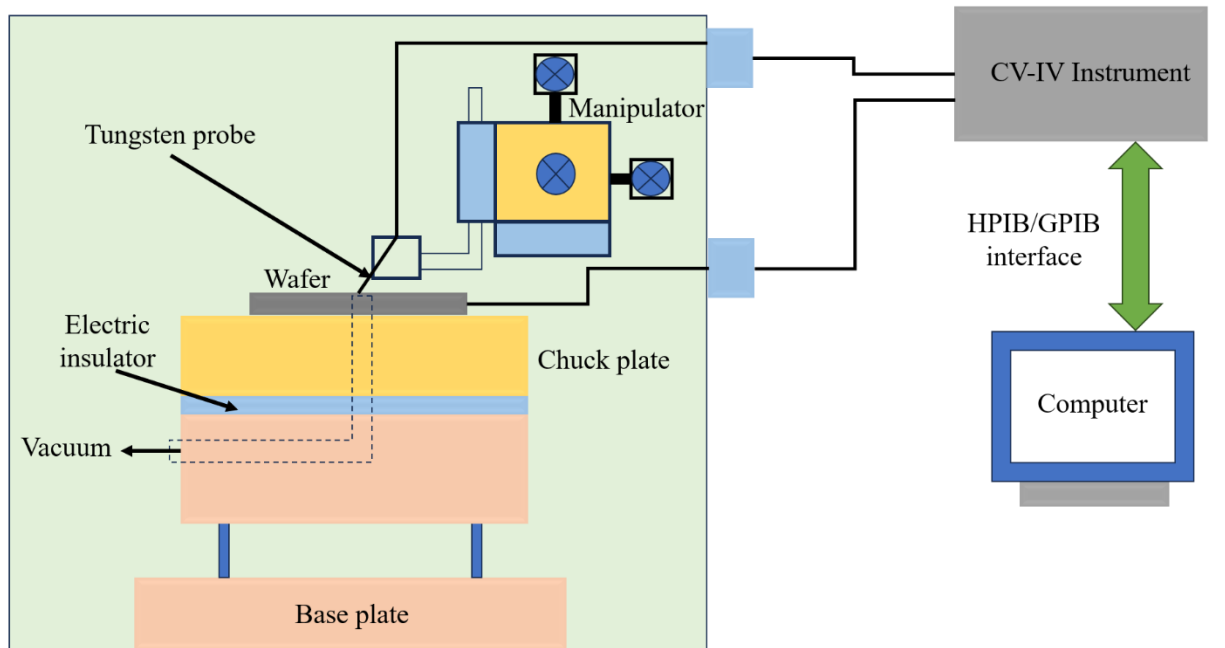
FIG. 3.16. Setup of CV and IV measurements.

3.2.5.5. Constant Voltage Stressing

To gain insights into the physical degradation processes affecting gate dielectrics and their interfaces, constant voltage stress tests (CVS) are frequently utilized at various applied electric field levels.
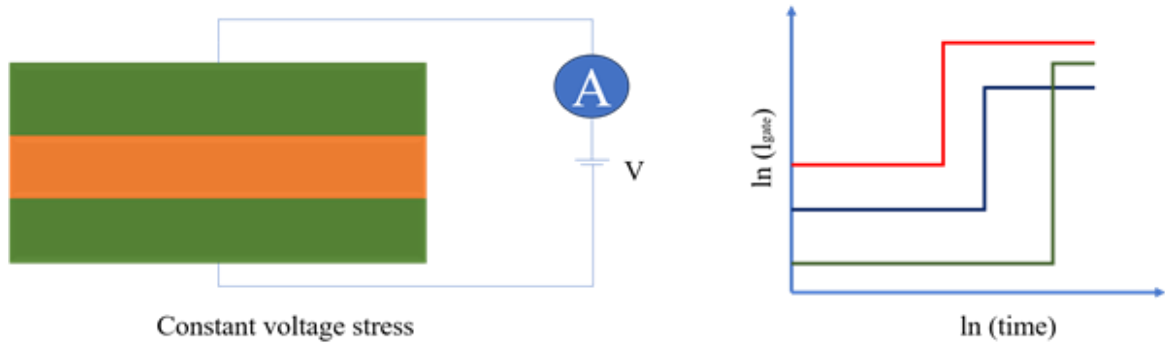
FIG. 3.17. Schematic of constant voltage stress measurement.

We examined the impact of stress at a consistent electric field. Stressing was interrupted for every 100s to monitor the capacitance-voltage and current-voltage characteristics.

Reference:

[1]   R. G. Larson and T. J. Rehg, "Liquid Film Coating," *Liq. Film Coating", SF Kistler PM Schweizer Chapman Hall Glas.*, pp. 99–100, 1997.

[2]   R. V Stuart, "Sputtering. Vacuum technology, thin films, and sputtering." New York: Academic Press, 1983.

[3]   K. Chopra, *Thin film device applications*. Springer Science & Business Media, 2012.

[4]   J. Mertz, *Introduction to optical microscopy*. Cambridge University Press, 2019.

[5]   B. Herman and J. J. Lemasters, "Optical microscopy: emerging methods and applications," 2012.

[6]   S. Burany, "Scanning Electron Microscopy and X-Ray Microanalysis. J. Goldstein, D. Newbury, D. Joy, C, Lyman, P. Echlin, E. Lifshin, L. Sawyer, and J. Michael. Kluwer Academic, Plenum Publishers, New York; 2003, 688 pages (Hardback, $75.00) ISBN 0-306-47292-9," *Microsc. Microanal.*, vol. 9, no. 5, p. 484, 2003.

[7]   F. J. Giessibl, "Review of Modern Physics," *949œ983*, 2003.

[8]   Y. Yuan and T. R. Lee, "Contact angle and wetting properties," *Surf. Sci. Tech.*, pp. 3–34, 2013.

[9]   A. Krishnan, Y.-H. Liu, P. Cha, R. Woodward, D. Allara, and E. A. Vogler, "An evaluation of methods for contact angle measurement," *Colloids Surfaces B Biointerfaces*, vol. 43, no. 2, pp. 95–98, 2005.

[10]   K. K. Chittur, "FTIR/ATR for protein adsorption to biomaterial surfaces," *Biomaterials*, vol. 19, no. 4–5, pp. 357–369, 1998.

[11]   A. R. Hind, S. K. Bhargava, and A. McKinnon, "At the solid/liquid interface: FTIR/ATR—the tool of choice," *Adv. Colloid Interface Sci.*, vol. 93, no. 1–3, pp. 91–114, 2001.

[12]   L. A. Lyon *et al.*, "Raman spectroscopy," *Anal. Chem.*, vol. 70, no. 12, pp. 341–362, 1998.

[13] P. K. Hansma and J. Kirtley, "Recent advances in inelastic electron tunneling spectroscopy," *Acc. Chem. Res.*, vol. 11, no. 12, pp. 440–445, 1978.

[14] M. A. Reed, "Inelastic electron tunneling spectroscopy," *Mater. today*, vol. 11, no. 11, pp. 46–50, 2008.

[15] M. M. Browne, G. V Lubarsky, M. R. Davidson, and R. H. Bradley, "Protein adsorption onto polystyrene surfaces studied by XPS and AFM," *Surf. Sci.*, vol. 553, no. 1–3, pp. 155–167, 2004.

[16] S. L. McArthur, "Applications of XPS in bioengineering," *Surf. Interface Anal. An Int. J. devoted to Dev. Appl. Tech. Anal. surfaces, interfaces thin Film.*, vol. 38, no. 11, pp. 1380–1385, 2006.

[17] A. Aitken and M. Learmonth, "Protein determination by UV absorption," *protein Protoc. Handb.*, pp. 3–6, 1996.

[18] D. F. Swinehart, "The beer-lambert law," *J. Chem. Educ.*, vol. 39, no. 7, p. 333, 1962.

[19] Q. Wang *et al.*, "Reevaluating protein photoluminescence: remarkable visible luminescence upon concentration and insight into the emission mechanism," *Angew. Chemie*, vol. 131, no. 36, pp. 12797–12803, 2019.

[20] H. B. Bebb and E. W. Williams, "Photoluminescence I: theory," in *Semiconductors and semimetals*, Elsevier, vol. 8, pp. 181–320, 1972.

[21] A. A. Shamsuri and S. A. A. Z. M. Darus, "Statistical analysis of tensile strength and flexural strength data from universal testing machine," *Asian J. Probab. Stat.*, vol. 9, no. 3, pp. 54–62, 2020.

[22] G. A. Mabbott, "An introduction to cyclic voltammetry," *J. Chem. Educ.*, vol. 60, no. 9, p. 697, 1983.

[23] P. T. Kissinger and W. R. Heineman, "Cyclic voltammetry," *J. Chem. Educ.*, vol. 60, no. 9, p. 702, 1983.

[24] B. L. Diffey, "Sources and measurement of ultraviolet radiation," *Methods*, vol. 28, no. 1, pp. 4–13, 2002.

Chapter 4: Analytical Modelling and Fabrication of Flexible BSA based MIM Structure and its Optoelectronic Applications

4.1. Introduction

Previous three chapters dealt with primary objective of the work, brief literature review and discussion about the characterization techniques used in this dissertation along with instrumental details. The thesis is aimed at inclusion of protein to modern electronics (Proteotronics), that will benefit the society by providing biodegradable, bio-compatible and even bio-metabolizable devices. Thus, study of physical, structural and electrical properties of protein is necessary. In this chapter, bovine serum albumin (BSA), an animal sourced protein obtained from bovine blood has been studied structurally and morphologically. BSA based MIM structure was fabricated on ITO coated PET as well as paper substrate to study its application in radio frequency devices and as UV photoactive material respectively. It will be seen that such devices can definitely come at very low-cost and wide applications.

The dielectric properties of BSA were investigated in experimental studies [1,2] with a focus on applications involving radiowave to microwave frequencies. The study showed a significantly high dielectric constant value for BSA, suggesting its potential suitability as a replacement for traditional oxides in bio-electronics domain. BSA is widely recognized as a universal blocking agent due to its non-reactivity towards a majority of proteins. Furthermore, it possesses the capability to serve as a carrier for many exogenous and endogenous substances. Consequently, it holds potential for the transportation of medications and ligands, making it a prospective route for application in future bio-sensors [3].

The chapter is divided into two parts. Firstly, structural and morphological characteristics of BSA protein film are studied. MIM capacitor was fabricated on

flexible substrate using BSA as dielectric. The CV and IV measurements along with measurement under CVS were carried out for electrical characterization of the device. The charge storage mechanism is also explained with corresponding models. Bending of the device and measuring the performance post-bending was performed to study its mechanical robustness. Secondly, A device was fabricated on flexible trace-on paper substrate with pencil drawn interdigitated graphite electrodes and its performance as an UV photoactive layer has been investigated.

4.2. BSA based MIM device

The fabrication method and characterization of BSA MIM device are discussed below:

4.2.1. Materials and Methodology

Plastic substrate was used for BSA MIM fabrication. The polyethylene terephthalate (PET) substrate with indium tin oxide (ITO) deposited on it, was obtained from Sigma Aldrich (catalog number 639303), and has a surface resistance of 60 Ω/sq. Before the fabrication process, the ITO-PET underwent a cleaning procedure involving the use of methanol for a duration of 10 minutes while being subjected to continuous ultrasonication. Subsequently, the substrates were rinsed with DI water and exposed to ultraviolet (UV) radiation for a period of 2 hours. A uniform coating of aqueous solution of BSA was applied onto substrates using spin coating at various rotational speeds (2000, 2500, and 3000 rpm) for a duration of 60 seconds. The coated substrates were subsequently dried for a period of 4 hours at a temperature of 40 °C. FESEM (Zeiss Supra 40) was employed to study the thickness and morphology of the film. The film spun at 2500 rpm exhibited the best consistency. As a result, this particular sample was selected for subsequent stages of studying film characteristics and device fabrication. The chemical bonds of the BSA film were analyzed using FTIR-ATR (Agilent Cary 630) instrument. (Nano surf easyscan2) AFM was used to estimate the degree of roughness on the film surface. Furthermore, the film was optically characterized using Shimadzu UV-1800 UV-Vis Spectrophotometer. In this

experiment, 80 nm Al was deposited onto the film employing thermal evaporator (Hind High Vac BC 300) using a shadow mask with an area of 4×10^{-3} cm². The purpose of this process was to create electrical top contacts. The electrical properties of the device were assessed by employing the Agilent E4980A LCR meter and the Keithley 2604B source meter. Constant voltage stressing (CVS) experiment was conducted to investigate the reliability of the device. Subsequently, the devices were subjected to repeated bending at various bending radii to assess their reliability.

4.2.2. Result and Discussion

The results obtained after physical characterization, electrical characterization and reliability study under mechanical stress of BSA based device are discussed below:

4.2.2.1. Physical Characterization

The cross-sectional profile of the thin BSA layer was seen using FESEM, as depicted in FIG. 4.1(a). The process of spin-coating results in a homogeneous film, with 2.71 µm thickness. The protein contains amide I bonds which is shown in the FTIR spectra of FIG. 4.1(b). The absorption of the Amide I region is closely related to the conformation of the peptide backbone, primarily influenced by the stretching vibration of the C=O bond and to a lesser extent by the stretching vibration of the C-N bond [4,5]. Deconvoluted BSA spectra demonstrates the presence of six prominent peaks, which are observed at wavenumbers of 1602, 1627, 1650, 1675, and 1691 cm^{-1}. The strong peak observed at a wavenumber of 1650 cm^{-1} corresponds to the characteristic of the α-helix, which predominates the proteins' secondary structure. Existence of 'β-turn' is revealed by the spectral peak observed at a wavenumber of 1675 cm^{-1}. The typical features of the β-sheet structure are observed at 1627, 1691, and 1602 cm^{-1} [6]. FIG. 4.3(b) displays both amide II and amide I region. The coexistence of many peaks in the observed spectra indicates that the film comprises a combination of α-helical, β-sheet, and 'β-turn' structural elements, which confirms its protein nature. Furthermore, it is

worth noting that the thin film does not exhibit denaturation or the presence of disordered structures.
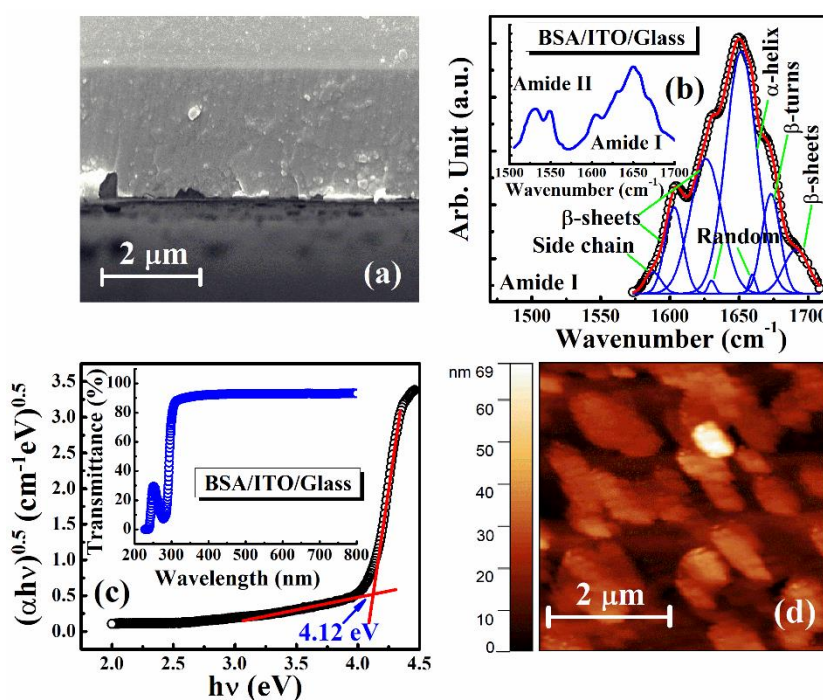
FIG. 4.1. (a) FESEM image of BSA provides evidence for a layer thickness of approximately 2.71 μm; (b) FTIR-ATR analysis reveals sub-peaks in the region of static amide-I, the two amide regions (I and II) are shown in the inset; (c) Tauc plot of BSA shows a band gap of 4.12 eV, % transmittance is shown in the inset; (d) BSA film surface is studied employing AFM.

Absorption of the BSA film was evaluated in the 220 nm to 800 nm wavelength range. FIG. 4.1(c) depicts the Tauc plot, which represents the relationship between its optical absorption spectra and the material's bandgap. The extrapolation of the Tauc plot reveals an optical bandgap of 4.12 eV [7,8]. The transmittance spectrum depicted in FIG. 4.1(c) (inset) has its value over 90% within the visible wavelength range, showing that the film is highly transparent.

In order to investigate the BSA film morphologically AFM was employed. FIG. 4.1(d) illustrates the surface morphology within a designated area measuring 5×5 μm². The calculated average surface roughness (r.m.s.) was ~8.9 nm, suggesting the presence of both peaks and valleys in the film.

4.2.2.2. Electrical characteristics

Electrical characterization of BSA based MIM device involves capacitance and current voltage characteristics, along with performance of the device under voltage stress.

Capacitance Voltage characteristics

FIG. 4.2(a) illustrates the plot showing the relationship between normalized capacitance and voltage for the capacitor based on BSA. The measurements were conducted within a frequency from 10^5 Hz to 10^6 Hz. Experimental data of normalized capacitance in the plot, reveals a negative curvature. The capacitance values were determined theoretically and represented by solid lines. The expression for the capacitance can be represented as follows,

$$\frac{\Delta C}{C_0} = \alpha V^2 + \beta V \qquad (4.1)$$

where ΔC is the difference of the capacitance at zero bias (C_0) and the capacitance at the voltage V applied, the change in capacitance relative to C_0, denoted as $\Delta C/C_0$, is termed as the normalised capacitance and is quantified as parts per million (ppm). The voltage coefficients of capacitance (VCC) as mentioned in the equation, are characterized in quadratic (VCC-α) and linear (VCC-β) terms, that determine the nature of the CV graph. VCC-α assumes a crucial function in application of high frequency devices, while VCC-β can be removed through the implementation of appropriate filter circuit designs[9].
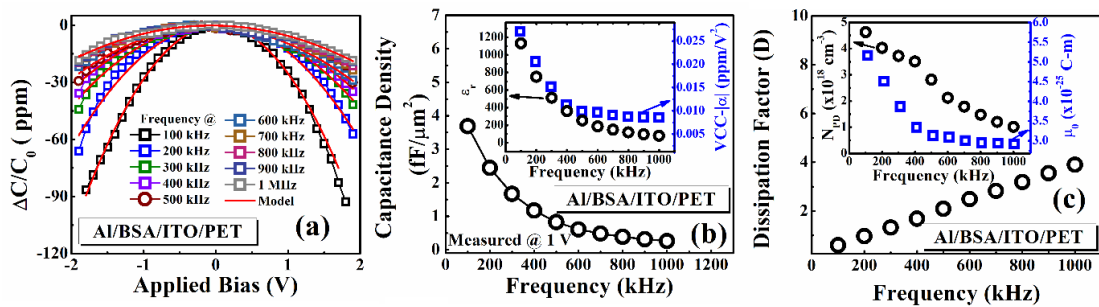
FIG. 4.2. (a) Non-linear capacitance-voltage relationship exhibits a negative curvature; (b) Capacitance density at different frequencies at 1 V, variation of the VCC- |α| and dielectric constant with frequency (in inset); (c) Linear relationship of dissipation factor with frequency, and the dipole density and the permanent dipole moment plotted at different frequencies (inset).

Capacitance density at 1V was plotted against frequency and shown in FIG. 4.2(b). Capacitance density of 3.69 fF/μm², was recorded at 100 kHz frequency. However, it was noted that the capacitance density had a non-linear degradation, resulting in a fall to 0.261 fF/μm² when the input frequency was increased to 1 MHz. The observed variance may be attributed to a significant change in capacitance at various frequencies due to the presence of charges within the traps. These traps exemplify a fixed temporal characteristic, leading to a decrease in value and subsequently resulting to a lower capacitance as the frequency increases. The previously established capacitance model has already proved the presence of non-linearity [10]. At high frequencies, the nonlinearity factor, resulting from the existence of interfacial defects and varying polarizations, diminishes as the carriers are unable to effectively track the applied alternating current (AC) signal [11].

The graph in FIG. 4.2(b) (inset) illustrates the correlation between the modulus value of VCC-α and the input frequency. The value of the VCC-|α| was 0.027 ppm/V² at 100 kHz, and it exhibits a further reduction as the frequency increases. The negative VCC-α arises when the constant dipole inclines within the dielectric. This inclination is caused by polarization, as well as electronic or ionic orientation. Various analytical models have provided explanations for this phenomenon [12,13]. According to the International Technology Roadmap for Semiconductors (ITRS), it is stipulated that the value of VCC-α for a conventional MIM device must be below 100. It is worth noting that the reporting of a below 100 VCC-α is not extensively documented in the literature [14,15]. The presence of a negative VCC-α can potentially contribute to the attainment of a low VCC values by mitigating the corresponding high positive characteristics exhibited by other dielectric materials in stack dielectric structures [16,17]. Furthermore, it is important to note that the VCC-α exerts a significant influence on the relaxation period of thin films, thus resulting in electrode polarization [18,19]. The FIG. 4.2(b) (inset) shows the relative permittivity of the protein dielectric plotted against frequency. A relative permittivity of value around 80 was observed at 1 MHz

frequency, which closely aligns with the value previously reported [2](~81, for 7g/dl BSA solution with pH 5.07).

FIG. 4.2(c) illustrates the relationship between the dielectric dissipation and frequency. The observed curve exhibited a positive correlation with frequency, indicating a rise as frequency increased. Notably, the dissipation factor remained below unity exclusively until reaching a frequency threshold of 200 kHz, rendering it particularly suitable for utilization within this specific range of frequency. The dielectric loss can be ascribed to several factors, including resistance at the electrodes, the presence of defect states in between the dielectric and contacts, poor grain boundaries [20]. An analogous attribute was previously reported by Goswami et. al [21-24].

Sanal et.al.[13], have modelled analytically VCC-α as,

$$VCC - \alpha = -\frac{N_{PD}\lambda^3 \mu_0^4}{81\varepsilon(0)[kT]^3 t^2} \tag{4.2}$$

where, the number of dipoles is denoted as N_{PD}, the permanent dipole moment is given as μ_0, the field correction factor is given as λ, it can be represented as $\lambda = \frac{3\varepsilon_r}{(2\varepsilon_r + 1)}$ by Lorentz approach, $\varepsilon(0)$ be the static permittivity given as $\varepsilon_0 \varepsilon_r$, where ε_0 denotes permittivity in vacuum, the BSA film thickness is denoted as t. As we know the relation, $\frac{\chi}{\varepsilon_0} = \varepsilon - 1$, and employing appropriate substitution $\chi = \frac{\mu_0^2 N_{PD}}{3kT}$, the value of μ_0 can be estimated as,

$$\mu_0 = \sqrt{\frac{3kT\varepsilon_0(\varepsilon_r - 1)}{N_{PD}}} \tag{4.3}$$

which can be re-written as $\mu_0 = A'.\sqrt{\frac{(\varepsilon_r - 1)}{N_{PD}}}$ \hfill (4.4)

We have replaced, $A' = \sqrt{3kT\varepsilon_0}$ which is a constant.

Combination of equations (4.2) and (4.3) yield the number of dipoles N_{PD},

$$N_{PD} = \frac{-\lambda^3 \varepsilon_0 (\varepsilon_r - 1)^2}{9\varepsilon_r (KT)t^2 . VCC - \alpha} \tag{4.5}$$

with the substitution of λ (approximating $\varepsilon_r \gg 1$) in equation (4.5),

$$N_{PD} = \frac{-3\varepsilon_0 (\varepsilon_r - 1)^2}{8\varepsilon_r (KT)t^2 . VCC - \alpha} \tag{4.6}$$

which can be written as,

$$N_{PD} = A^{"} \frac{\varepsilon_0 (\varepsilon_r - 1)^2}{\varepsilon_r . VCC - \alpha} \tag{4.7}$$

where the constant term for the dielectric is $A^{"} = \frac{-3}{8(KT)t^2} = -1.24$ $J^{-1}cm^{-2}$. The estimation of the values of N_{PD} and μ_0 from equation (4.7) and equation (4.3) are plotted against frequency and shown in the FIG. 4.2(c) (inset). At 1 MHz frequency, it was seen that the insulating material BSA exhibited a dipole density of 1.01×10^{18} cm^{-3} with μ_0 value of 2.92×10^{-25} C-m. Table 4.1 shows of the values of N_{PD} and μ_0 compared with devices previously reported.

Table 4.1. Values of N_{PD} and μ_0 for different dielectrics

Structure	Measuring Freq.	N_{PD} (cm^{-3})	μ_0 (C-m)	Ref.
Al/SiO$_2$/Al	1 kHz	2.61×10^{20}	2.13×10^{-29}	[13]
Hydrated BSA	100 kHz	4.7×10^{21}	1.2×10^{-29}	[1]
Al/BSA/ITO	1 MHz	1.01×10^{18}	2.92×10^{-25}	This Work

Charge Storage Mechanism

The primary constituents of amino acid encompass Carbon (C), Hydrogen (H), Oxygen (O), and Nitrogen (N), although many amino acids may contain additional elements within their side chains. An amino acid is composed of a α-carbon atom, joined with an amine group (-NH2), a carboxyl group (-COOH), and a side chain (R group) [25,26]. The arrangement of orbitals surrounding the α-

carbon atom are tetrahedral in nature and allows for the involvement of four distinct groups. Consequently, this arrangement gives birth to two distinct spatial configurations, resulting in two potential stereoisomers of the amino acid, namely L and D. The α-carbon, serving as the chiral centre, exhibits this property [27]. The side chains (R groups) of these arrangements exhibit opposing characteristics, including variations in size, structure, and electrical charge. These properties influence the solubility of amino acids in water. Amino acids can be categorised based on nature of their side chains, which include hydrophobic, aromatic, polar uncharged, basic, and acidic. When an amino acid dissolves in an aqueous medium, it assumes a bipolar ionic state, where the carboxyl group (COO-) and the amino group (NH3+) are present as charged species. The amino acid is sometimes classified as a neutral molecule known as a zwitterion due to its possession of both positive and negative charges [27]. FIG. 4.3(a) and 4.3(b) show the non-ionic and zwitter-ionic forms of amino acids, respectively. Hence, in a solvent composed of water, there is a state of equilibrium between the molecular configuration and the zwitterionic configuration of amino acids. Amino acids are also commonly recognized as amphiprotic due to their possession of both amine and carboxylic acid functional groups, allowing them to both donate and accept protons.
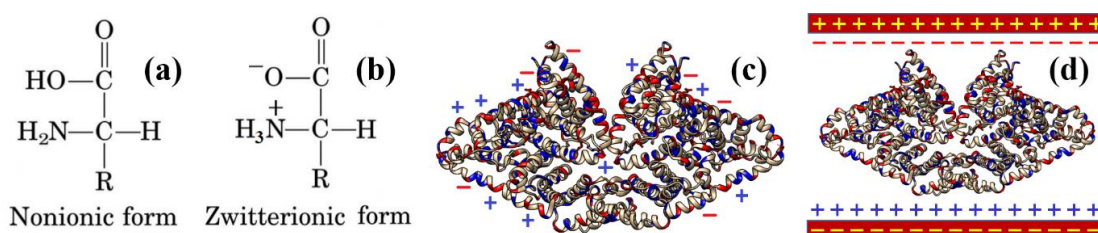
FIG 4.3. (a) Non-ionic and (b) Zwitterionic forms of amino acids; (c) Side chains of hydrated BSA containing both positive and negative charges, and in this representation, mobile H_3O^+ ions are denoted by a '+' sign, whereas mobile OH- ions are denoted by a '-' sign; (d) The generation of electric double-layer capacitor by hydrated BSA under the influence of an applied bias.

The equilibrium constant (K_{eq}) defines the propensity of an acid (HA) to undergo deprotonation and generate its corresponding conjugate base (A). In the context of ionization reactions, the equilibrium constants are commonly referred to as ionization or dissociation constants, denoted as K_a. pK_a can be mathematically expressed as $pK_a = \log (1/K_a) = -\log K_a$ [28], which is a tool to measure the tendency of groups to liberate a proton and it is evident from the pK_a expression that for tenfold decreasing tendency, pK_a value increases by one unit [29]. Protonation takes place when pH < pK_a, and conversely, deprotonation happens when pH > pK_a value. At a pH value equal to the pK_1, the concentration of the cation $NH_3^+CH(R)CO_2H$ and the zwitterion $NH_3^+CH(R)CO_2^-$ are equivalent. Similarly, at a pH value equal to the pK_2, the concentrations of the zwitterion $NH_3^+CH(R)CO_2^-$ and the anion $NH_2CH(R)CO_2^-$ are identical. The equilibrium point between the net positive charge and the negative charge is precisely located at the midpoint between the two pK_a values [30]; as a result of which the average charge of all forms become null [31], this point is known as isoelectric point (pI). At this point, the mobility of electrons reaches zero. In general, it is commonly considered that the concentration of zwitterions is significantly larger than that of neutral molecules, when comparing their pK values to those of amines and carboxylic acids. The generation of zwitterions is significantly influenced by the nature of its R group.

The method proposed by Theodor von Grotthuss, a chemist of German origin, involves the transportation of protons through the process of tunneling or hopping through interconnected hydrogen bond chains within water molecules. The transport process results in a greater mobility (3.6×10^{-3} cm^2 sec^{-1} V^{-1}) of H$^+$ ions compared to K$^+$ ions, although having similar hydrodynamic radii [30]. In this particular process, the transfer of a proton occurs as it jumps from one molecule to another through the exchange of a hydrogen bond with a covalent link. Nevertheless, the transfer of a unit charge does not have any observable outcome, as it only induces polarization in water molecules as it traverses one single water chain. Therefore, it is necessary for the water chain to undergo

reorganization in order to accommodate additional protons. This can be achieved by facilitating the transportation of a Bjerrum D orientation defect, which influences the orientation of water molecules within the chain. In the end, the transfer of a unit charge will occur through the collective movement of H+ and a D defect. Likewise, the transfer of a negatively charged hydroxide ion (OH-) - commonly referred to as a proton hole can occur across the chain by the identical two-step processes [32]. Therefore, it is apparent that protonic conductivity exhibits two distinct charge carriers, akin to semiconductors. These properties of the hydrated BSA film are attributed to the creation of mobile ions and the creation of ionic double layers (IDL). The presence of mobile ions in hydrated BSA is attributed to the interaction between acidic/basic amino acid residues and water molecules. [33]. The acidic and basic reactivity of a protein remains unaltered upon the conversion of α-amino and α-carboxyl groups of amino acids into peptide bonds inside proteins, as there exists only one α-amino group (located at the N-terminus) and one α-carboxyl group (located at the C-terminus). In the hydrated state, the R groups of acidic and basic amino acids engage in interactions with water, hence exhibiting acid-base behavior [34]. The characteristics of basic and acidic amino acids present in BSA, including those with both negatively and positively charged R groups, are depicted in Table 4.2. The pK_R values of glutamic acid and aspartic acid, which are present in BSA, is found to be 4.25 and 3.65, respectively. The values indicate that the ionization of both amino acids occurs at pH levels lower than that of water, which has a pH of 7 under normal conditions.

Table 4.2. Properties of basic and acidic amino acids found in BSA

Amino Acid	Abbreviation	Symbol	pK_a Values		
			pK_1 (-COOH)	pK_2 (-NH_3^+)	pK_R (R group)
Positively charged R groups					
Lysine	Lys	K	2.18	8.95	10.53
Histidine	His	H	1.82	9.17	6.00
Arginine	Arg	R	2.17	9.04	12.48
Negatively charged R groups					
Aspartate	Asp	D	1.88	9.60	3.65
Glutamate	Glu	E	2.19	9.67	4.25

As a result, the carboxyl groups undergo deprotonation upon interaction with water (H_2O), leading to the generation of mobile H_3O^+ ions and negatively charged side chains $(CH_2)_2COO^-$ and CH_2COO^-. Despite the positively charged nature of Histidine's R group, its pK_R value ($pK_R=6$) is lower than the pH value of water. Consequently, Histidine behaves as an acid and undergoes deprotonation upon interaction with water. In the same way, it can be shown that the pK_R values of the basic amino acids lysine and arginine are 10.53 and 12.48, respectively. These values surpass the pH level of water. Hence, upon interaction with water, the amino groups present in the side chains undergo protonation, resulting in the formation of OH- mobile ions and the corresponding positively charged $(CH_2)_4$-NH_3^+ side chains.

FIG. 4.3(c) illustrates the molecular configuration of BSA in the form of a Homo dimer. The figure highlights the presence of acidic amino acid residues (in blue), and basic amino acid residues (in red). Additionally, the figure includes a schematic representation depicting the negatively and positively charged side chains, accompanied by mobile ions of hydrated BSA positioned between two electrodes. The formation of ionic double layers (IDL) occurs when proteotronic capacitors are subjected to a voltage bias, as depicted in FIG. 4.3(d). The static nature of the positively and negatively charged side chains in BSA allows for a reaction to biased voltages due to its elongated chain structure. Consequently, the accumulation of H_3O^+ and OH- ions at the negative and positive electrodes, respectively, results in the creation of ionic double layers. The movement of H_3O^+ and OH- ions, either through direct drift or Grotthuss transfer, facilitates the presence of a free proton (H+) mechanism at the electrode interface. The formation of an ionic double layer is hypothesized to enhance the capacitance of the capacitor, consistent with the findings of the experiment.

Current Voltage characteristics

The leakage current density is plotted with applied bias as shown in FIG. 4.4. The curve shows current density value of 1.2×10^{-7} A/cm^2 at 1V which is low,

compared to ITRS 2024 criterion. Table 4.3 presents a summary of the parameters of MIM capacitors using different dielectrics, as previously reported.
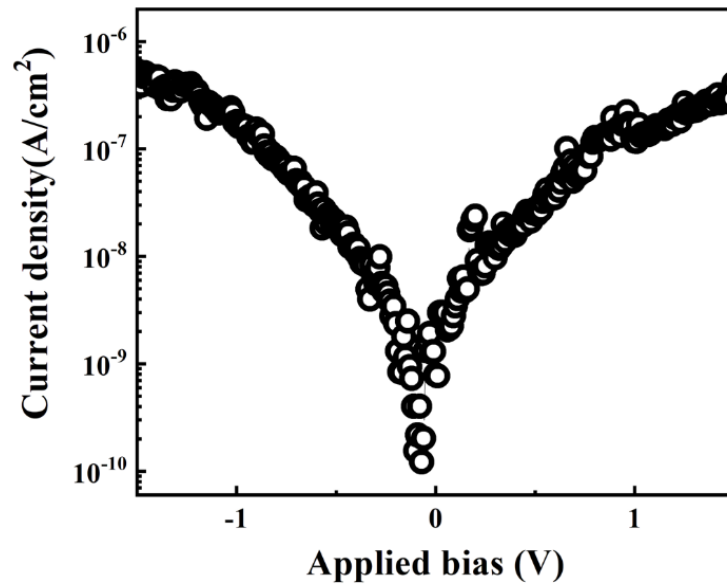
FIG. 4.4. Current density varied with applied voltage.

Table 4.3. MIM structure parameters with various dielectrics

Dielectric	Keratin [35]	TiO$_2$/SiO$_2$ [36]	Graphene Oxide [37]	This work	ITRS at 2024 [14]
Thickness	500 nm	2.5/14 nm	370 nm	2.71 µm	-
Top/bottom electrode	Al	Al/TaN	Pt/ITO	Al/ITO	-
Work function	4.3	4.3/4.6	5.6/4.24	4.3/4.24	-
Capacitance density (fF/µm^2) at 1 MHz	0.04	11.9	4	0.26	>12
VCC–α at 1 MHz	-	90	100.6	-0.008	<100
Current density (A/cm^2)	1.34×10^{-6}	2.8×10^{-5}	-	1.2×10^{-7}	$<1.0 \times 10^{-8}$

Constant Voltage stress (CVS)

To investigate reliability of the BSA based MIM capacitor, CVS experiments were conducted at fixed voltages of 3V and 5V. It was noticed that the percentage of capacitance increases as the stress time increases for constant voltages of 3V and 5V, as shown in FIG. 4.5. This potential alteration might be caused by the phenomenon of charge trapping occurring between BSA film and the electrodes. Therefore, the phenomenon of charge trapping in dielectric materials was seen

under voltage stress on top electrode, resulting in the creation of additional electric dipoles. The observed outcome is an augmentation in the density of capacitance as a factor of the duration of stress, wherein the highest level of charge trapping is observed at locations with deep traps [38]. The $\Delta C/C_0$ value for a 10-year duration is approximately 0.99% in both cases, indicating significant competency of the device in terms of reliability.
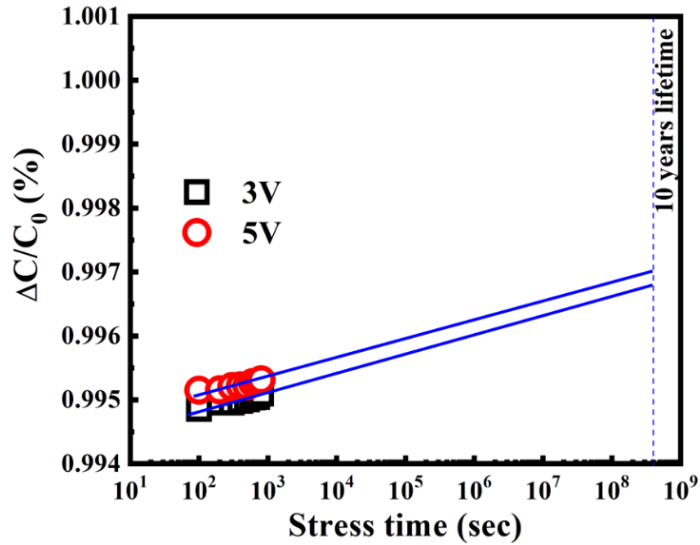
FIG. 4.5. $\Delta C/C_0$ data obtained under CVS for 10 year.

4.2.3. Reliability under flexibility test

To study the mechanical resilience of BSA MIMs, they were subjected to bending with varying curvature radii using the X-Y-θ test. At 1 MHz, the value of capacitance density was obtained after each instance of stress, with a total of 100 bending cycles. This experimental setup and the resulting data are shown in FIG. 4.6(a). The centre of the substrate was selected for device characterization due to their heightened susceptibility to stress during bending.

The experimental results indicate increase in capacitance density to 0.66 fF/µm² when the bending radius is increased to 1.05 cm at the 1000 cycles. This increase can be attributed to two factors: the expansion of device area by Poisson's effect, and the reduction in dielectric thickness due to lateral expansion. Reducing radius to 0.75 cm results in a gradual fall of capacitance to 0.14 fF/µm². FIG. 4.6(b)

and FIG. 4.6(c) present the BSA and Al surface conditions, respectively, following 1000 bending cycles at 0.75 cm radius.
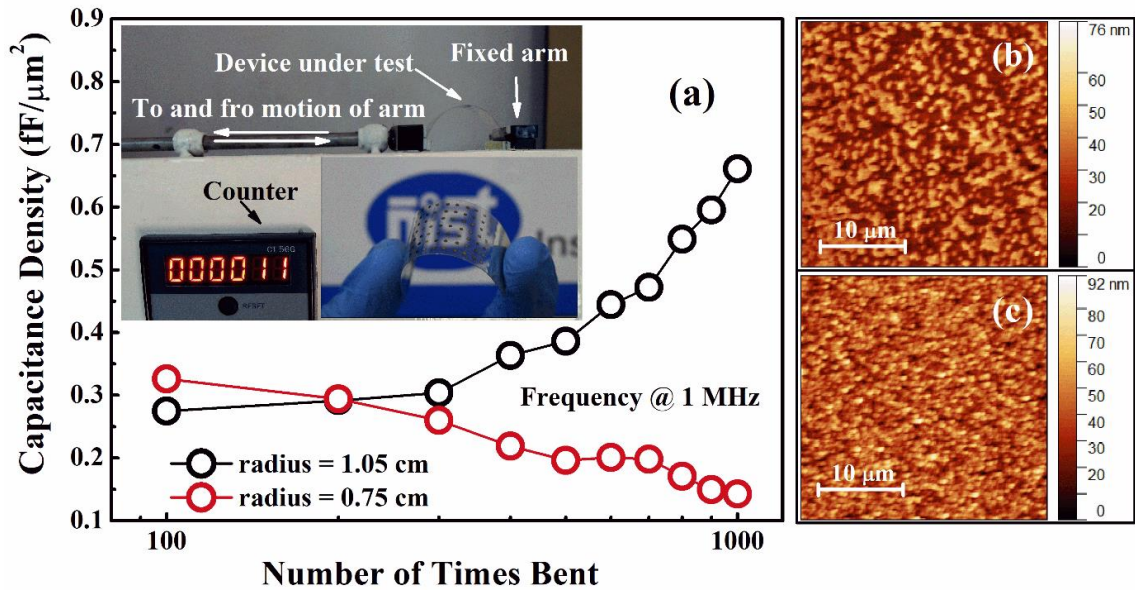
FIG. 4.6. (a) Capacitance density variation with the bending cycles at different bending radii, (in the inset) image of MIM device, and automated mechanical bending device; The surface scan of (b) BSA and (c) Aluminum (Al) in across 30×30 μm² area after 1000 cycles bending at 0.75 cm radius.

Notably, no significant discontinuities were observed on the surface within the scanned region of 30×30 μm². Nevertheless, the progressive decline in capacitance could potentially suggest the emergence of tiny vertical fractures within the dielectric or metal layers [39,40]. Therefore, electronics based on BSA may be suitable for flexible electronic applications that require a certain degree of device bending within certain limits.

4.3. Optoelectronic Study of BSA device on paper substrate

Compared to metallic or plastic substrates paper as a substrate is much more attractive [41]. Paper substrates has already been used in the devices, such as foldable printed circuit boards [42], cellulose-based batteries [43], thermochromic displays [44], etc.

Paper has some good qualities to be used in devices such as insulating characteristics and heat resistance. Paper exhibits a good quality porosity that may

be attributed to 3-D arrangement of cellulose fibres. This property enables solvents or liquids to pass through the paper and makes it suitable for sensing applications [45]. Various methods have been used on paper for device fabrication such as screen printing [46], spray coating [47], photolithography [48], Pen-on-Paper method [49], and Pencil-on-Paper method [50]. The electrodes commonly used on paper are carbon fibers, carbon nanotubes, graphene powder, and copper and silver inks. Usage of carbon materials as electrodes has few disadvantages such as complex and costly processes of thermal evaporation and sputtering, thus limiting its extensive usage [51]. On the other hand, Pencil writing on Paper (PoP), a common method adopted for years dating back to the 16th century is more suitable choice for researchers.

Using Pentalic brand type B pencil , an electronic RC circuit and a capacitor was fabricated on paper [52]. Supercapacitor using an interdigitated electrode was reported with pencil on paper [53]. Graphite pencil electrodes were used on paper for glucose biosensing application [54,55]. Paper substrates were also used a UV sensor by deposition of Zinc Oxide (ZnO) film layer on pencil drawn interdigitated electrodes [56].

Interdigitated electrodes (IDEs) are a kind of co-planar electrodes that have a periodic arrangement with resemblance to comb or numerous fingers. IDEs are found is capacitive circuits known as Interdigitated Capacitors (IDCs). IDCs are analogous to multiple layers of dielectric sandwiched in between finger-like structures forming a capacitor. IDCs has advantages in reducing Signal to Noise Ratio (SNR), and increasing sensitivity and high capacitance values. IDCs are particularly effective in gas sensors, chemical sensors, humidity sensors and for applications in high frequencies microwave and radio frequency integrated circuits.

4.3.1. Materials and method

Prior fabrication paper substrates were cleaned with methanol for 10 minutes, it eliminates any remaining surface impurities present in the surface. HB,

2B, and 4B pencils were used to draw thick lines on the cleaned paper. The lines drawn using 4B pencil shows lowest resistance when tested as conducting electrodes. 4B pencils were used to draw IDEs of dimension 1.5 cm x 1.5 cm, 0.1 cm inter-electrode distance, and 1.3 cm electrode length. Graphite particles that were loosely bound were removed using repeated high-speed N_2 flash. BSA solution was dropcasted upon the IDE on a paper substrate and dried at room temperature for six hours. Both capacitor and UV sensor were fabricated with device and the corresponding CV and IV were measured using Agilent E4980A LCR meter and Keithley 2604B source meter. The fabrication procedure is shown in FIG. 4.7.

An analytical formulation for calculating the interelectrode capacitance of an IDE [57] is given in equation (4.8).

$$C_{IDC} = (N-3)\frac{C_{I,IDC}}{2} + 2\frac{C_{I,IDC}C_{E,IDC}}{C_{I,IDC}+C_{E,IDC}}$$

(4.8)

where, the half capacitance of the exterior is denoted as $C_{E,IDC}$, half-capacitance of the interior is $C_{I,IDC,}$ and the number of electrodes are denoted by N, which must be greater than three. Using equation (4.8) the capacitance of the BSA based IDE paper capacitor was found to be 2.2×10^{10} F/μm^2.

FIG. 4.7. Process of fabricating IDE based device on paper substrate.

4.3.2. Prototype set-up development
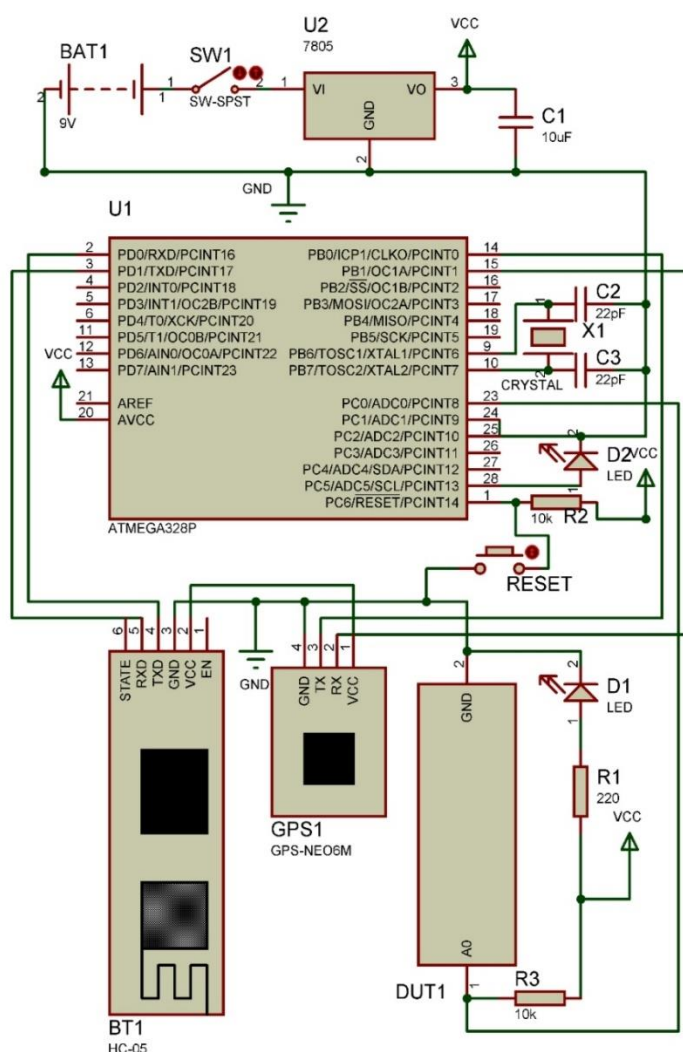
FIG. 4.8. Prototype circuit diagram for optoelectronic characterization setup of BSA as photoactive materials.

A voltage divider composed of a 10 Mega-ohm resistor R3 and UV detector is linked with 8-bit microcontroller CMOS ATmega328/P. It is a low-power circuit built on the improved RISC (reduced instruction set computer) architecture, as shown in FIG. 4.8. The microcontroller has access to an external 9V power supply.

4.3.3. Characterization of BSA as UV photoactive material

The BSA based paper device was subjected to UV illumination, and the corresponding photocurrent was measured. UV illumination of two different

wavelengths (232 nm and 280 nm) were used. The measurement setup is shown in FIG. 4.9(a). The dark current measured in the applied voltage range of +15 V to -15 V is shown in FIG. 4.9 (b). The current measured was in the order of 10^{-5} A in the absence of UV light. When UV light was shone a little increase in photocurrent was observed. The photocurrent generated at different wavelengths remained unchanged. On-off current was measured on the BSA paper device as illustrated in FIG. 4.9(c). UV light pulses of three minutes duration were applied on BSA. A consistent pattern was observed in the photo response that implies presence of UV sensing ability of BSA. Reduction in dark current and rise in photocurrent was observed.
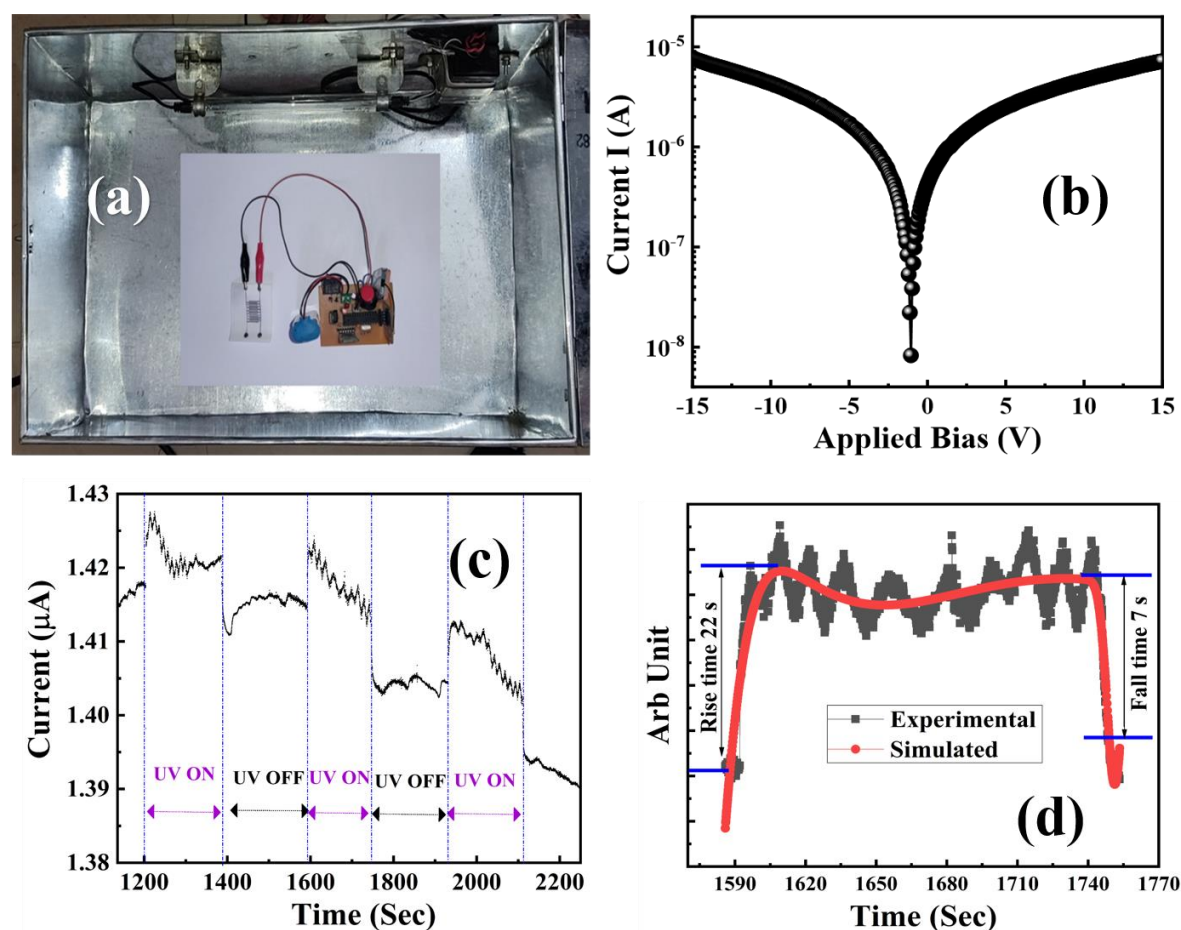
FIG. 4.9. (a) Image of paper based physical UV sensor with BSA as an active layer; (b) Characteristics of Protein based device on paper without UV illumination; (c) Photocurrent of BSA in on-off response to 232 nm UV light with 200 secs time interval on paper substrate with Graphite electrodes; (d) Estimation of rise time and fall time.

After light absorption the current rises steeply, then a state of progressive saturation is reached which is followed by gradual decay due to cessation of UV irradiation. The steep rising slope denotes the fast photoresponse of the device. Small fluctuations were observed in FIG. 4.9(c) which may arise due to noise in the applied illumination intensity. The responsivity R can be denoted as the ratio of photocurrent and input light intensity [58,59],

$$R = \frac{I_{light} - I_{dark}}{P_{light}} = \frac{I_{ph}}{P_{light}} \qquad (4.9)$$

where I_{ph} is the photocurrent obtained from UV illumination at a wavelength of 232 nm and P_{light} is laser intensity of 1 mW. The value of R is found to be in the order of 10^{-3} A/W. Besides the responsivity rise time and fall time are also important to quantify the performance. Rise time can be explained as the time required by the amplitude of the current to reach 90% of its final value from initial, while the fall time calculates the transition from 90% to initial value. In our device the rise time and fall time are measured as 22 and 7 s respectively (FIG. 4.9(d)). The photoresponse can be explained by generation of electron and hole pairs (e-h), resulting into rise in current. A significant quantity of e-h pairs undergo recombination on the protein's surface, so facilitating the seamless transfer of electrons and augmenting the photocurrent [60]. Some of the e-h pairs undergo recombination due to defect states in the material. The thickness of the BSA layer plays the crucial role. The thickness must be less that the penetration depth (1/α), where α is the coefficient of absorption. The devices achieve best performance when the noise is lower than the noise of incident photon. Optical noise arises due to discrete nature of the photon.

To summarize, animal protein bovine serum albumin (BSA) was the focus material in this chapter. It was used to fabricate of transparent and flexible MIM capacitor. BSA was deposited using simple spin coating technique in ITO coated PET. The value of capacitance density was 0.261 fF/μm² at 1 MHz and exhibited a negative slope denoting negative value of VCC-α. The charge storage mechanism was explained using suitable model that aligns the device with

inorganic capacitors' mechanisms. The value of $\Delta C/C_0$ under different stress voltages obtained showed fluctuation of capacitance by less than 1.0% for a 10-year. The mechanical flexibility of the device was quite high and was demonstrated by repetitive bending with varying radii that may be attributed to inherent high ductility of the protein film. The device thus has potential for application in fabrication of advanced bio-inspired extremely large-scale integrated circuits. A BSA based optoelectronic device was fabricated via the technique of flexible trace-on paper, incorporating interdigitated graphite electrodes created through pencil drawing. The device showed good responsivity of 10^{-3} A/W that denotes the viability of BSA to be used as future photoactive material.

Reference:

[1]   J. Eden, P. R. C. Gascoyne, and R. Pethig, "Dielectric and electrical properties of hydrated bovine serum albumin," *J. Chem. Soc. Faraday Trans. 1 Phys. Chem. Condens. Phases*, vol. 76, no. 0, pp. 426–434, 1980.

[2]   E. H. Grant, S. E. Keefe, and S. Takashima, "Dielectric behavior of aqueous solutions of bovine serum albumin from radiowave to microwave frequencies," *J. Phys. Chem.*, vol. 72, no. 13, pp. 4373–4380, Dec. 1968.

[3]   A. S. Mohamad, R. Hamzah, K. F. Hoettges, and M. P. Hughes, "A dielectrophoresis-impedance method for protein detection and analysis," *AIP Adv.*, vol. 7, no. 1, p. 15202, 2017.

[4]   G. Z. C. H. S. S. AW, "DeFlores LP Jones KC Tokmakoff A," *Acc. Chem. Res*, vol. 41, pp. 432–441, 2008.

[5]   D. M. Byler and H. Susi, "Examination of the secondary structure of proteins by deconvolved FTIR spectra," *Biopolymers*, vol. 25, no. 3, pp. 469–487, Mar. 1986.

[6]   J. Kong and S. Yu, "Fourier transform infrared spectroscopic analysis of protein secondary structures," *Acta Biochim. Biophys. Sin. (Shanghai).*, vol. 39, no. 8, pp. 549–559, 2007.

[7]   S. Chakraborti *et al.*, "Interaction of Polyethyleneimine-Functionalized ZnO Nanoparticles with Bovine Serum Albumin," *Langmuir*, vol. 28, no. 30, pp. 11142–11152, 2012.

[8]   J. Tauc and A. Menth, "States in the gap," *J. Non. Cryst. Solids*, vol. 8, pp. 569–585, 1972.

[9]   K.-S. Tan *et al.*, "Error correction techniques for high-performance differential A/D converters," *IEEE J. Solid-State Circuits*, vol. 25, no. 6, pp. 1318–1327, 1990.

[10]   C. Mahata *et al.*, "High performance TaYOx-based MIM capacitors," *Microelectron. Eng.*, vol. 86, no. 11, pp. 2180–2186, 2009.

[11]   C.-H. Cheng *et al.*, "A study on frequency-dependent voltage nonlinearity of SrTiO3 rf capacitor," *Electrochem. Solid-State Lett.*, vol. 13, no. 12, p. H436, 2010.

[12]   T. H. Phung, P. Steinmann, R. Wise, Y.-C. Yeo, and C. Zhu, "Modeling the Negative Quadratic VCC of SiO_2 in MIM Capacitor," *IEEE electron device Lett.*, vol. 32, no. 12, pp. 1671–1673, 2011.

[13]   A. Sanal, P. Sathyanarayanan, V. Velmurugan, and D. Kannadassan, "Negative VCC in MIM capacitors: modeling and experiments," *J. Comput. Electron.*, vol. 17, no. 1, pp. 458–462, 2018.

[14]   C.-C. Lin, Y.-H. Wu, R.-S. Jiang, and M.-T. Yu, "MIM Capacitors Based on $ZrTiO_x$/$BaZr_yTi_{1-y}O_3$ Featuring Record-Low VCC and Excellent Reliability," *IEEE electron device Lett.*, vol. 34, no. 11, pp. 1418–1420, 2013.

[15]   S.-U. Park *et al.*, "Analysis of reliability characteristics of high capacitance density MIM capacitors with SiO_2–HfO_2–SiO_2 dielectrics," *Microelectron. Eng.*, vol. 88, no. 12, pp. 3389–3392, 2011.

[16]   C. Jorel, C. Vallée, P. Gonon, E. Gourvest, C. Dubarry, and E. Defay, "High performance metal-insulator-metal capacitor using a $SrTiO_3$/ZrO_2 bilayer," *Appl. Phys. Lett.*, vol. 94, no. 25, p. 253502, 2009.

[17]   S. J. Kim *et al.*, "Improvement of voltage linearity in high-/spl kappa/MIM capacitors using HfO_2-SiO_2 stacked dielectric," *IEEE Electron Device Lett.*, vol. 25, no. 8, pp. 538–540, 2004.

[18]   J. H. Beaumont and P. W. M. Jacobs, "Polarization in potassium chloride crystals," *J. Phys. Chem. Solids*, vol. 28, no. 4, pp. 657–667, 1967.

[19]   C. Fang, M. Wang, P. Han, Y.-Q. Cao, D. Wu, and A.-D. Li, "High-Performance MIM Capacitors Using Zr-Sn-Ti-O Dielectrics Derived from Atomic Layer Deposition," *IEEE electron device Lett.*, vol. 40, no. 5, pp. 682–685, 2019.

[20]   R. Thomas, D. C. Dube, M. N. Kamalasanan, S. Chandra, and A. S. Bhalla, "Structural, electrical, and low-temperature dielectric properties of sol–gel derived $SrTiO_3$ thin films," *J. Appl. Phys.*, vol. 82, no. 9, pp. 4484–4488, 1997.

[21] R. K. Goyal and A. B. Kulkarni, "Electrical properties of novel three-phase polymer nanocomposites with a high dielectric constant," *J. Phys. D. Appl. Phys.*, vol. 45, no. 46, p. 465302, 2012.

[22] M. K. Hota, C. K. Sarkar, and C. K. Maiti, "Frequency-dependent dielectric response of HfTaOx-based metal–insulator–metal capacitors," *Semicond. Sci. Technol.*, vol. 27, no. 8, p. 85002, 2012.

[23] C. Y. Kim *et al.*, "Frequency-dependent capacitance-voltage and conductance-voltage characteristics of low-dielectric-constant SiOC (-H) thin films deposited by using plasma-enhanced chemical vapor deposition," *J. Korean Phys. Soc.*, vol. 57, 2010.

[24] A. Goswami and A. P. Goswami, "Dielectric and optical properties of ZnS films," *Thin Solid Films*, vol. 16, no. 2, pp. 175–185, 1973.

[25] A. L. Lehninger, *Lehninger Principles of Biochemistry: David L. Nelson, Michael M. Cox*. Recording for the Blind & Dyslexic New York, 2004.

[26] J. D. Westbrook, C. Shao, Z. Feng, M. Zhuravleva, S. Velankar, and J. Young, "The chemical component dictionary: complete descriptions of constituent molecules in experimentally determined 3D macromolecules in the Protein Data Bank," *Bioinformatics*, vol. 31, no. 8, pp. 1274–1278, 2015.

[27] T. E. Creighton, *Proteins: structures and molecular properties*. Macmillan, 1993.

[28] F. J. R. Rossotti and H. Rossotti, "The determination of stability constants: and other equilibrium constants in solution," McGraw-Hill, 1961.

[29] D. D. Perrin, B. Dempsey, and E. P. Serjeant, *pKa prediction for organic acids and bases*, vol. 1. Springer, 1981.

[30] A. J. Bard and L. R. Faulkner, "Fundamentals and applications. Electrochem," *Methods*, vol. 2, no. 482, pp. 580–632, 2001.

[31] A. D. McNaught and A. Wilkinson, *Compendium of chemical terminology*, vol. 1669. Blackwell Science Oxford, 1997.

[32] G. Meisenberg and W. H. Simmons, *Principles of medical biochemistry e-book*. Elsevier Health Sciences, 2016.

[33] J. E. Nielsen and G. Vriend, "Optimizing the hydrogen-bond network in Poisson–Boltzmann equation-based pKa calculations," *Proteins Struct. Funct. Bioinforma.*, vol. 43, no. 4, pp. 403–412, 2001.

[34] M. Aftabuddin and S. Kundu, "Hydrophobic, hydrophilic, and charged amino acid networks within protein," *Biophys. J.*, vol. 93, no. 1, pp. 225–231, 2007.

[35] R. Singh, Y.-T. Lin, W.-L. Chuang, and F.-H. Ko, "A new biodegradable gate dielectric material based on keratin protein for organic thin film transistors," *Org. Electron.*, vol. 44, pp. 198–209, 2017.

[36] Y.-H. Wu, W.-Y. Ou, C.-C. Lin, J.-R. Wu, M.-L. Wu, and L.-L. Chen, "MIM Capacitors With Crystalline-TiO$_2$/SiO$_2$ Stack Featuring High Capacitance Density and Low Voltage Coefficient," *IEEE electron device Lett.*, vol. 33, no. 1, pp. 104–106, 2011.

[37] A. Bag, M. K. Hota, S. Mallik, and C. K. Maiti, "Graphene oxide-based flexible metal–insulator–metal capacitors," *Semicond. Sci. Technol.*, vol. 28, no. 5, p. 55002, 2013.

[38] H. Y. Kwak *et al.*, "Characterization of Al2O3-HfO2-Al2O3sandwiched MIM capacitor under DC and AC stresses," *Solid. State. Electron.*, vol. 79, pp. 218–222, 2013.

[39] J. W. Hutchinson and Z. Suo, "Mixed mode cracking in layered materials," *Adv. Appl. Mech.*, vol. 29, pp. 63–191, 1991.

[40] P. Servati and A. Nathan, "Orientation-dependent strain tolerance of amorphous silicon transistors and pixel circuits for elastic organic light-emitting diode displays," *Appl. Phys. Lett.*, vol. 86, no. 3, p. 33504, 2005.

[41] S. M. Khan, J. M. Nassar, and M. M. Hussain, "Paper as a substrate and an active material in paper electronics," *ACS Appl. Electron. Mater.*, vol. 3, no. 1, pp. 30–52, 2020.

[42] A. C. Siegel, S. T. Phillips, M. D. Dickey, N. Lu, Z. Suo, and G. M. Whitesides, "Foldable printed circuit boards on paper substrates," *Adv. Funct. Mater.*, vol. 20, no. 1, pp. 28–35, 2010.

[43] G. Nyström, A. Razaq, M. Strømme, L. Nyholm, and A. Mihranyan, "Ultrafast all-polymer paper-based batteries," *Nano Lett.*, vol. 9, no. 10, pp. 3635–3639, 2009.

[44] A. C. Siegel, S. T. Phillips, B. J. Wiley, and G. M. Whitesides, "Thin, lightweight, foldable thermochromic displays on paper," *Lab Chip*, vol. 9, no. 19, pp. 2775–2781, 2009.

[45] P. J. Bracher, M. Gupta, and G. M. Whitesides, "Patterning precipitates of reactions in paper," *J. Mater. Chem.*, vol. 20, no. 24, pp. 5117–5122, 2010.

[46] W. Dungchai, O. Chailapakul, and C. S. Henry, "A low-cost, simple, and rapid fabrication method for paper-based microfluidics using wax screen-printing," *Analyst*, vol. 136, no. 1, pp. 77–82, 2011.

[47] Y. Li, C. Liu, Y. Xu, T. Minari, P. Darmawan, and K. Tsukagoshi, "Solution-processed organic crystals for field-effect transistor arrays with smooth semiconductor/dielectric interface on paper substrates," *Org. Electron.*, vol. 13, no. 5, pp. 815–819, 2012.

[48] L. Yu and Z. Z. Shi, "Microfluidic paper-based analytical devices fabricated by low-cost photolithography and embossing of Parafilm®," *Lab Chip*, vol. 15, no. 7, pp. 1642–1645, 2015.

[49] A. Russo, B. Y. Ahn, J. J. Adams, E. B. Duoss, J. T. Bernhard, and J. A. Lewis, "Pen-on-paper flexible electronics," *Adv. Mater.*, vol. 23, no. 30, pp. 3426–3430, 2011.

[50] M. Weng *et al.*, "Multiresponsive Bidirectional Bending Actuators Fabricated by a Pencil-on-Paper Method," *Adv. Funct. Mater.*, vol. 26, no. 40, pp. 7244–7253, 2016.

[51] A.-N. Kawde, M. D. Aziz, N. Baig, and Y. Temerk, "A facile fabrication of platinum nanoparticle-modified graphite pencil electrode for highly sensitive detection of hydrogen peroxide," *J. Electroanal. Chem.*, vol. 740, pp. 68–74, 2015.

[52] J. E. Thompson, "Pencil-on-paper capacitors for hand-drawn rc circuits and capacitive sensing," *J. Chem.*, vol. 2017, 2017.

[53] M. P. Down, C. W. Foster, X. Ji, and C. E. Banks, "Pencil drawn paper based supercapacitors," *RSC Adv.*, vol. 6, no. 84, pp. 81130–81141, 2016.

[54] M. Santhiago and L. T. Kubota, "A new approach for paper-based analytical devices with electrochemical detection based on graphite pencil electrodes," *Sensors Actuators B Chem.*, vol. 177, pp. 224–230, 2013.

[55] Ö. Sağlam, B. Kızılkaya, H. Uysal, and Y. Dilgin, "Biosensing of glucose in flow injection analysis system based on glucose oxidase-quantum dot modified pencil graphite electrode," *Talanta*, vol. 147, pp. 315–321, 2016.

[56] M. A Ansari, D. Dasgupta, and K. Sreenivas, "Paper based ZnO thin film UV light detector using graphite pencil based electrodes," *Adv. Mater. Proc.*, vol. 2, no. 7, pp. 428–432, 2017.

[57] R. Igreja and C. J. Dias, "Analytical evaluation of the interdigital electrodes capacitance for a multi-layered structure," *Sensors Actuators A Phys.*, vol. 112, no. 2–3, pp. 291–301, 2004.

[58] G. Konstantatos, "Current status and technological prospect of photodetectors based on two-dimensional materials," *Nat. Commun.*, vol. 9, no. 1, p. 5266, 2018.

[59] L. D. Bastatas, P. Wagle, E. Echeverria, A. J. Austin, and D. N. McIlroy, "The Effect of UV Illumination on the room temperature detection of vaporized ammonium nitrate by a ZnO coated nanospring-based sensor," *Materials (Basel).*, vol. 12, no. 2, p. 302, 2019.

[60] M. Shakiba and A. V Akimov, "Dependence of Electron–Hole Recombination Rates on Charge Carrier Concentration: A Case Study of Nonadiabatic Molecular Dynamics in Graphitic Carbon Nitride Monolayers," *J. Phys. Chem. C*, 2023.

Chapter 5: Capacitive and Memristive Responses of Papain based Bio-realistic MIM Structures

5.1. Introduction

In the previous chapter, 'Proteotronic' capacitor and UV photoactive device fabricated with BSA as dielectric layer have been studied. BSA, a protein sourced from animal blood has unique mechanical and chemical properties to be used as an excellent dielectric material in bio-functional electronics that can easily replace traditional inorganic devices in near future. Our main aim in this dissertation was to study the application of both plant and animal based proteins in charge storage devices and to discuss their dielectric mechanisms. In this chapter, characteristics of plant based protein papain will be explored and its applications in capacitive, and memristive devices will be investigated. Plant based protein can be obtained much more easily and the processing to extract pristine protein from raw material is uncomplicated compared to extraction of animal proteins. Hence, this chapter will show that in order to attain a sustainable electronic world in future, proteins procured both from plant and animal sources will play a key role.

Papain has been used as capacitive storage device and its dielectric properties has been studied by few researchers. György et. al performed matrix assisted synthesis of papain thin films using pulse laser deposition techniques. Frozen papain solution was used as deposition target instead of conventional powder deposition target. The bulk dielectric constant of papain was determined by conductivity study of papain pellet and was reported as 74.44 F/m by Muthulakshmi et. al. Study of the impact of temperature on dielectric constant of papain has shown that increase in temperature enhances dielectric properties of papain. It was seen that AC conductivity of papain is frequency dependent and papain obey large polaron tunneling model.

In this article, an attempt is made to address the origin of the resistive switching (RS) as well as capacitive behavior, observed in papain. In the first part the physical, optical and morphological characteristics of the film are studied. In the second part capacitance voltage property of papain thin film based MIM device is investigated and the mechanism of charge storage in the protein film is analysed. In the third part papain based memristor has been fabricated using various top electrodes and their impact on device performance has been discussed. The RS behavior has been explained using suitable current conduction mechanism. The IETS measurement of papain was obtained at low temperature. Finally, a model for explaining the switching mechanism in papain memristor has been proposed.

5.2. Materials and Methods

The papain solution was procured from Sigma-Aldrich as a buffered aqueous suspension solution (P3125) prepared from papaya latex. ITO (~100 nm) coated glass substrate was taken as the starting material for the fabrication of papain based devices. Initially substrate cleaning was performed using acetone and methanol consecutively under constant ultrasonication. After cleaning the substrate was rinsed in DI water. The papain was then spin-coated (3000 rpm, 60 sec.) onto ITO-glass, and the coated film was left to dry at 40°C for 30 mins. Finally, different top electrodes (Al, TiN, Pt and ITO) were deposited using circular shadow mask of 1.96×10^{-3} cm^2 area.

XPS was performed using the VG ESCALAB 220i-XL system. The film was optically characterized using UV-Vis Spectrophotometer (Shimadzu UV-1800) and the electrochemical analyses were performed using a Portable Potentiostat CS100. FTIR-ATR study was performed on the papain film within wavenumbers 4000–650 cm^{-1} using Agilent Cary 630 to inspect the chemical bonds present in the protein. Thickness of the film was measured by SUPRA 40 FESEM. AFM image was obtained using NanoSurf easy Scan 2. Photoluminiscence spectra were measured using a He-Cd laser, operating at 325 nm, and Raman spectroscopy analysis was performed with 532 nm laser, both employing Horiba T64000 instrument.

IETS was used to observe the traps in the film at 77 K. Agilent E5263A 2-channel source monitor, SR830 lock-in amplifier were used in the IETS measurement. CV and IV characteristics of the devices were studied using Agilent E4980A LCR meter and the Keithley 2604B source meter. The bottom electrodes were connected to the ground during all electrical measurements.

5.3. Results and discussion

The results obtained after physical characterizations, and electrical characterizations of papain based devices are discussed below:

5.3.1. Physical characterizations

The chemical bonds of the protein film papain can be investigated using XPS analysis. The high-resolution spectra of C $1s$, N $1s$, and O $1s$ were background corrected using Shirley backgrounds and deconvoluted using Gaussian–Lorentzian functions. The C $1s$ spectra (as shown in FIG. 5.1(a)) obtained from the papain film indicates four chemical bonds of C, by showing profile of four peaks. These four peaks involve C–C aliphatic bonds (C-1), C–NH$_2$ amino group (C-2) and two other amide groups CH$_2$–NCO (C-3) and NH–C=O (C-4), respectively [1,2].

The N $1s$ spectra deconvoluted and shown in FIG. 5.1(b) represents a single amide bond (N-1) (-NH$_2$) at 400.3 eV and a protonated amino groups, NH$_3^+$ (N-2) at 402.97 eV [3,4]. FIG. 5.1(c) presents the O$1s$ spectra with its two components. The O-1 peak (C-O) (~530.23 eV) may be linked with carbon and oxygen atom joined with a single bond whereas the O-2 peak (C=O) at 531.9 eV indicates the presence of a double bond between carbon and oxygen [2].

To obtain the optical bandgap of the protein film; the absorption spectrum (shown in FIG. 5.1(d), which corresponds to electron excitation across electronic bands, was measured along wavelength range of 300 to 900 nm [5]. To extract the optical band gap, the baseline correction method was used initially [6]. The extracted energy bandgap was found to be ~2.31 eV. The film exhibited high transparency with transmittance reaching the value of 86 % in the visible region

(inset of FIG. 5.1(d)). The electron transfer in papain has been studied using cyclic voltammetry, where the onset potential observed was around 0.35 V, corresponding to electron removed from highest occupied molecular orbital (HOMO) due to oxidation, and is shown in FIG. 5.1(e). The HOMO energy level of papain may be estimated using onset potential [7], and the lowest unoccupied molecular orbital (LUMO) level can also be deduced using the HOMO energy level and optical bandgap. The HOMO level is found to be 4.85 eV and LUMO level calculated using optical bandgap is 2.25 eV. The proposed band diagram of papain is shown in FIG. 5.1(f); this finding can provide an idea of charge transfer process in papain in ground state as well as in higher energy levels.
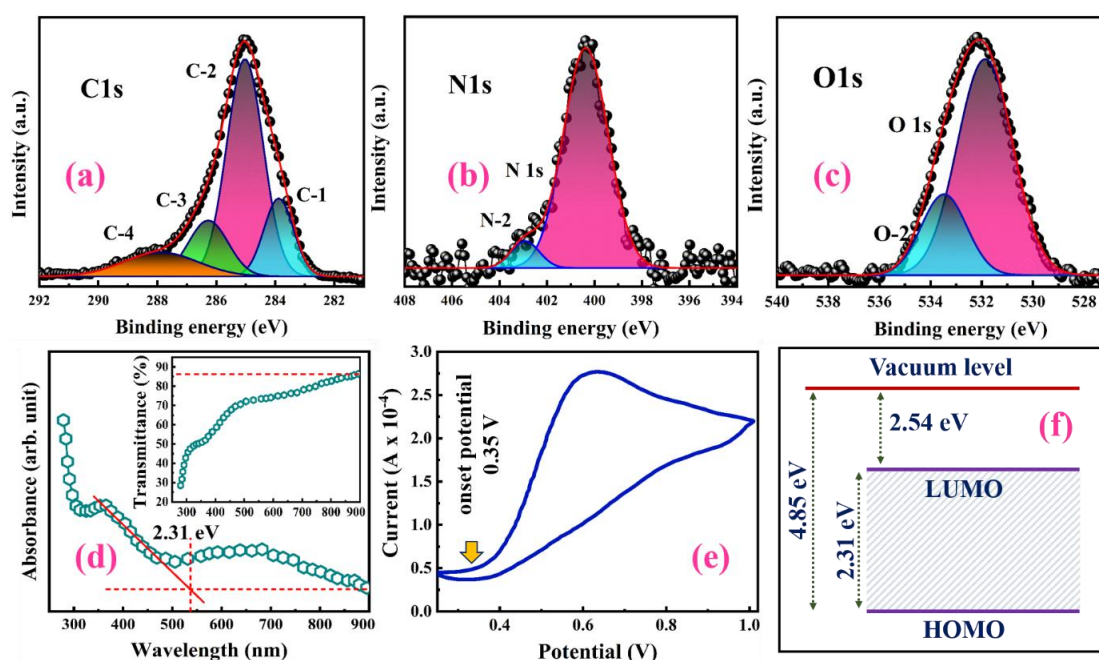
FIG. 5.1. XPS spectra of individual element photo lines of (a) C 1s, (b) N 1s, and (c) O 1s; (d) Band gap energy (Eg) of 2.31 eV was determined from the absorption spectra, transmittance close to 90% was observed (inset); (e) Cyclic Voltammetry (CV) characteristics of papain where the onset potential observed was around 0.35 V; (f) The proposed energy levels of papain used as an insulator where the electron affinity was found to be 2.54 eV.

FTIR absorption curve of papain showing region of static amide-I as well as other secondary structures is shown in FIG. 5.2(a). The backbone of papain structure can be observed by amide-I absorption which consists of major and

minor contribution from stretching vibration of C=O, and C–N respectively [8,9]. The major peaks obtained after deconvolution are estimated at 1622, 1633, 1650, 1667 and 1682 cm^{-1}. The peaks found at 1650 and 1633 cm^{-1} originate from the *a*-helical and *β*-sheet structure, respectively [10]. The peaks at 1622 and 1682 cm^{-1} are also related to the structure of *β*-sheet. The peak at 1667 cm^{-1} represents 'Turn'. To identify the secondary structures more distinctly, second order-derivative of the FTIR spectra was carried out and is shown in FIG. 5.2(b), where it is found that *a*-helical structure is predominately present in the film. However, *a*-helical, *β*-sheet and 'Turn' combinedly represent the structure of papain. The XPS and FTIR study thus reveals that papain is protein in nature.
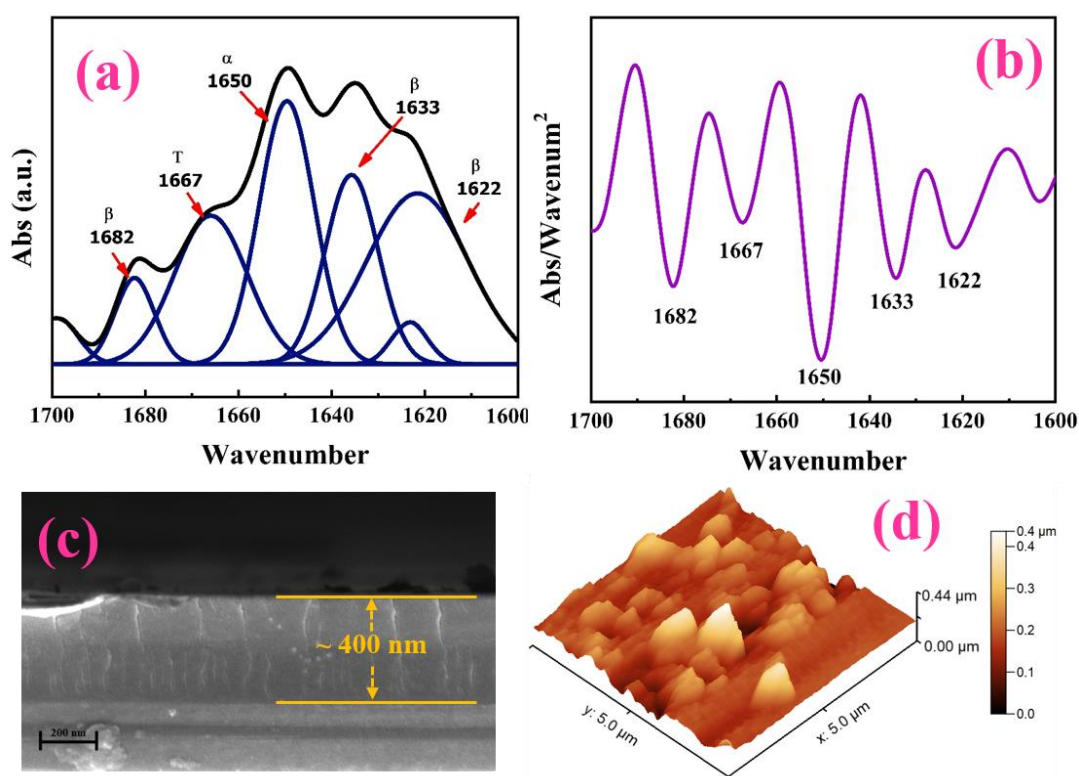
FIG. 5.2. (a) The amide I region of papain shown in FTIR-ATR spectrum; (b) Second order-derivative of spectra confirms the presence of α-helical, and β-sheets; (c) The FESEM cross-sectional image of the spin coated papain film shows the thickness to be ~400 nm; (d) AFM 3-D micrograph of the papain film across an area of 5×5 µm².

FIG. 5.2(c) shows the cross-sectional FESEM image of the papain film which was found to be ~ 400 nm thick. FIG. 5.2(d) reveals the surface morphology of the papain film on Glass/ITO substrate across 5×5 µm² area. The r.m.s. value was

found as ~102 ± 10 nm which project the presence of some undulations in the film. This morphology may be due to the presence of some non-spherical granules with varying sizes grains in the films, that can lead to polycrystallinity, the main reason for large hysteresis in the memristor.
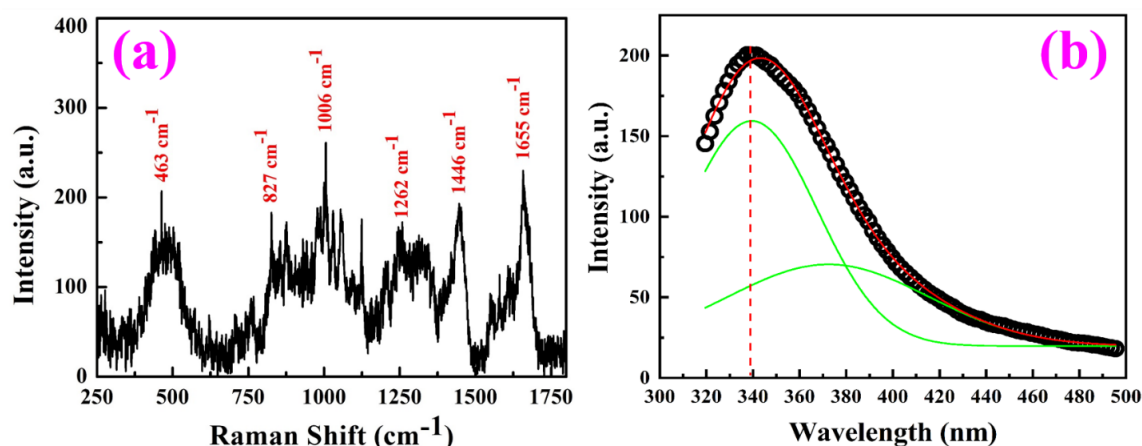
FIG. 5.3. (a) Raman spectra shows peaks corresponding to secondary structure of papain; (b) The PL spectra of papain shows absorption peak as well as a defect peak.

Raman spectroscopy analyses vibrational modes in papain structure. Amide I (C=0 stretching vibration), amide II (C-N stretching) and amide III (N-H bending) are of main interest. The other amides that were not visible correspond to amide IV, V ,VI associated with OCN bending, out-of-plane NH bending, and out-of-plane C=O bending respectively [11]. The Raman spectrum of papain is shown in FIG. 5.3(a). The peak visible at 1650 cm-1 corresponds to amide I band and a weak amide II band (substantial C-N stretching) is seen around 1550 cm^{-1}, whose intensity depends on α-helical content. Amide III (α helix, random coil, β sheet) bands are moderately visible around 1300 cm^{-1}. The room temperature PL spectrum of papain film is shown in FIG. 5.3(b). There is one broad peak at 340 nm. The deconvoluted spectrum reveals peaks at 340 nm and at 372 nm that shows presence of some defects in the dielectric.

5.3.2. Electrical Characterizations

5.3.2.1. Capacitance voltage characteristics

The capacitance voltage characterizations were performed using 3 μm thick papain film as dielectric. The plot of normalized capacitance against applied

voltage across 100 kHz to 1 MHz frequency is shown in FIG. 5.4(a). The value of VCC-α is of great significance in the capacitance curve and here a downward curvature is observed in the capacitance curve that attributes to the negative value of VCC-α. The variation of magnitude of VCC-α with change in frequency is shown in FIG. 5.4(b). VCC-α value at 200 kHz frequency is 0.095 ppm/V^2 that changes to 0.075 ppm/V^2 at 1MHz. Polarization of the dielectric film that result into different dipole orientation results into negative value of VCC-α. As per "The International Technology Roadmap for Semiconductors (ITRS)" lower value of VCC-α is desirable (lower than 100) [12, 13]. Thus, papain having negative VCC-α value can be stacked with other inorganic dielectric having high value of VCC-α , such that the net VCC-α can be lowered within desired limit [14,15]. The relative permittivity is varied with frequency (FIG. 5.4(b)), and the value of permittivity obtained is very high 300.4 at 1 MHz.
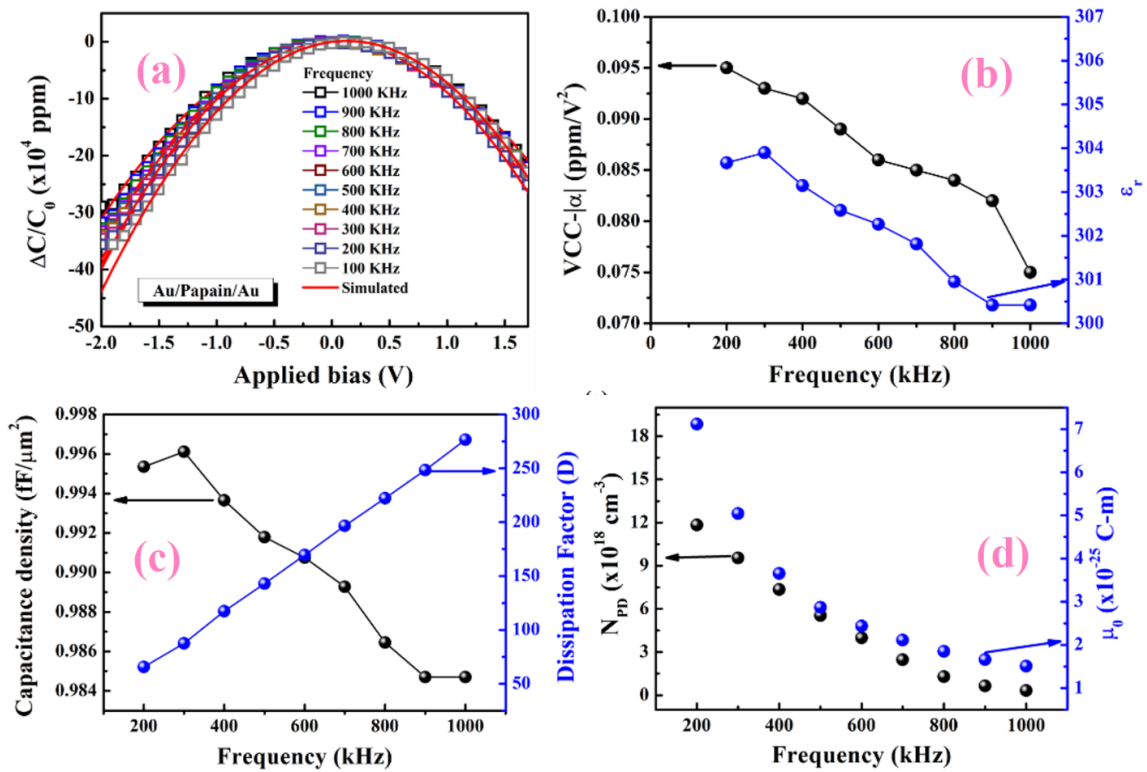
FIG. 5.4. (a) Normalized capacitance with negative slope plotted against applied voltage; (b) Frequency dispersion of VCC-$|\alpha|$ and dielectric constant of papain; (c) Capacitance density variation with frequency and change of dissipation factor with frequency; (d) Variation of number of dipoles (N_{PD}) and permanent dipole moment (μ_0) with frequency.

The capacitance density and the dissipation factor are plotted with frequency and illustrated in FIG. 5.4(c). The capacitance density non-linearly degrades with frequency that demonstrates the presence of traps in the dielectric, at higher frequency the traps are unable to track change in the AC input signal, thus the capacitance value decreases. The capacitance density decreased from 0.995 fF/μm^2 at 200 KHz to 0.9847 fF/ μm^2 at 1 MHz. The dissipation factor increases with frequency (FIG. 5.4(c) and a similar phenomenon is reported and explained in earlier literature [16–19]. The reasons of dielectric loss are mainly high surface roughness, electrode resistance, improper grain boundaries [20]. The equation of VCC-α is reported by Sanal et.al. [13]. With the help of an analytical model, the dipole density along with the permanent dipole moment were estimated as 3.328x10^{17} cm^{-3} and 1.5x10^{-25} C-m respectively at 1 MHz frequency, the equations are already described in chapter 4. The corresponding values are plotted and is shown in FIG. 5.4(d).

5.3.2.2. Charge storage mechanism

The electrical characteristics of papain can be explained using ionic double layer model. The peptide bond is a covalent bond that join amino group and carboxyl group of two adjacent amino acids by removing water molecules. In an aqueous solution of papain the acidic and basic amino acids react with water and can generate mobile ions [21].
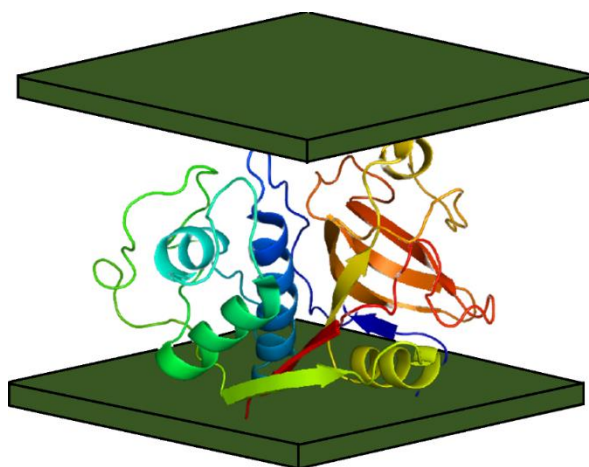
FIG. 5.5. Side chains (positive and negative) of hydrated papain in between electrodes.

Upon interaction with water, the carboxyl group deprotonates and produce H_3O^+ ions, while the amino group protonates to produce OH- mobile ions [22]. Both positive and negative side chains of papain (FIG. 5.5) fail to respond to applied voltage due to long chain structure and thus the H_3O^+ and OH- ions move towards negative and positive electrodes resulting in ionic double layer. This may take place using Grotthuss transfer that is explained as transport of free proton (H^+) that hops by exchanging hydrogen bond with covalent bond towards the electrodes that may be considered analogous to semiconductor transport of electrons and holes [23].

5.3.2.3. Current-voltage characteristics
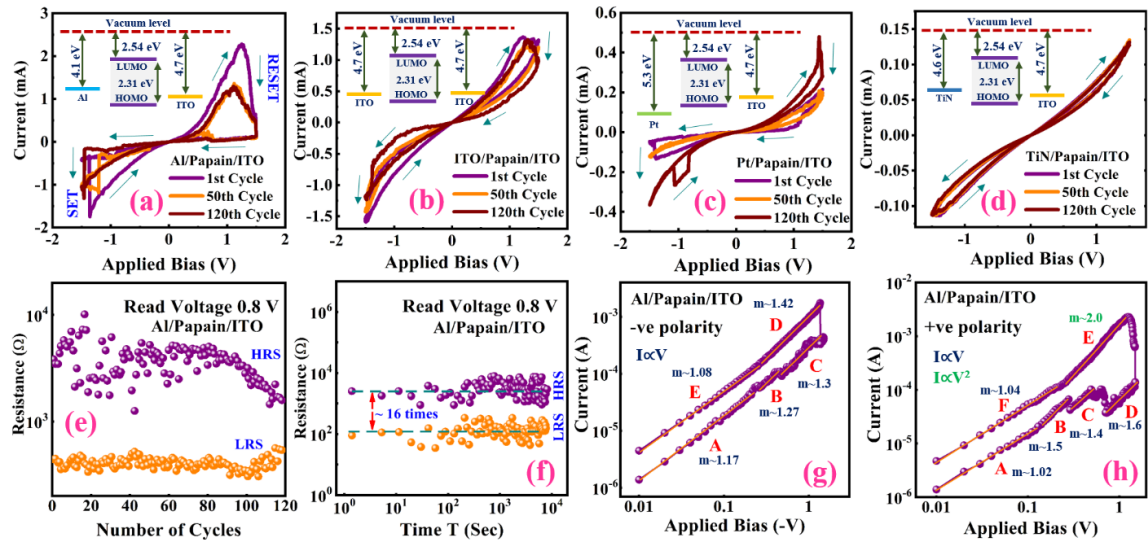
FIG. 5.6. (a) The IV characteristics of papain devices with (a) Al (b) ITO (c) Pt and (d) TiN top electrodes. The corresponding energy level diagrams of the four devices are shown in the inset where the φB0 was found to be 1.56 eV, 2.16 eV, 2.76 eV and 2.06 eV respectively; (e) Repetitive switching cycles dependent resistance of two states (LRS and HRS) with Al/papain/ITO structure at 0.8V read out voltage; (f) Data retention properties of Al/papain/ITO, measured in room temperature having ~16× times resistance ratio; The current-voltage characteristics of Al/papain/ITO in log-log scale for (g) ON state and (h) OFF state.

The current-voltage characteristic of Al/papain/ITO RS device is seen in FIG. 5.6(a). The device was primarily in the state of high resistance (HRS).

However, as a negative bias was applied on Al a rapid increase in current was observed after a specific voltage (V_{SET} ~ -1.35 V), driving the device towards a state of low resistance (LRS), known as SET. On the other hand, when a positive bias is applied, higher than a specific voltage (V_{RESET} ~ 1.3 V), the device goes back to its HRS, which is known as RESET. The SET and RESET occurs at the opposite polarity sites, which signify bipolar clockwise RS nature of the bio-memristor. Almost similar effects were seen in ITO/papain/ITO, Pt/papain/ITO and TiN/papain/ITO bio-memristor devices in FIG. 5.6(b-d), respectively. However, it is seen that hysteresis in IV characteristics, *i.e.,* ON/OFF ratio is poor in these devices as compare to the Al/papain/ITO device. While, Al work function is closer to ITO and TiN, but devices with ITO and TiN as top electrode does not show good RS behavior. It may suggest that metal electrode's work function might not be the decisive factor for injection of charge carrier and to maintain high ON/OFF ratio. Rather due to high negative Gibbs energy the reaction of Al with the existing O^{2-} or hydroxyl groups would be spontaneous, which gives rise to AlO_x layer beneath the top electrode in metal-insulator heterojunction [24,25]. As in the present metal-protein heterolayer, Al as the top electrode acts as a tetradentate ligand by sharing electrons with amino acid contained in papain, forming a bio-metallic interface. Hence, serving the prime purpose of stabilizing the heavy molecular weight peptides and low molecular weight chelants and overall achieving a bio-compatibility [26]. The corresponding energy band diagrams of the four structures differing in top electrodes are shown in the inset of FIG. 5.6(a –d), where the ϕ_{B0} was found to be 1.56 eV, 2.16 eV, 2.76 eV and 2.06 eV respectively. The details of the switching mechanism have been discussed in the next section.

It has been reported that a high dc voltage or pulse are required to electroform most of the RS devices. These initial processes can sometime lead to partial degradation of the device [27–29]. However, papain based devices do not require any initiation to exhibit RS phenomenon. This implies the advantage of using a protein as dielectric in a RS device. Also electroforming free resistive

memory device is cost effective as one extra (forming) process can be excluded from the operation. To study the non-volatile performance, the dc sweeping cycling and retention test were performed in Al/papain/ITO devices. Repetitive dc sweeping cycles dependent resistance of two states (LRS and HRS) are seen in FIG. 5.6(e). It is observed that HRS state is more unstable compare to LRS state, owing to the presence of conducting filament residues in the HRS state. The data retention properties were also studied in room temperature and shown in FIG. 5.6(f). Two distinct resistance states with ~16× times resistance ratio is observed in the measurement time frame.

The switching ratio is low in 2-D devices compared to 3-D structures, as in 3-D materials the 'sneak path' effect may come into the play [30]. In this regard, the low switching ratio from the 2-dimensional planer bio compatible papain based device is expected. Consequently, it is already reported that HRS/LRS >10 is necessary to fabricate a memory device with high efficiency [31].

In order to understand the RS origin in the papain memristive device, the conduction mechanism is also studied to evaluate the charge transport process. The current-voltage values of Al/papain/ITO are plotted again in log-log scale shown in FIG. 5.6(g) for positive applied bias and FIG. 5.6(h) for negative applied bias for evaluating the conduction mechanism. It is clear from the plot that multiple charge transport mechanism exists in the device in different region.

For the OFF state in FIG. 5.6(g), it is observed that, the slope (m) of the linear curve fitting at low as well as high voltage regions (denoted from "A" to "E") are close to 1, suggesting that the variation of current is almost linear with input voltage, *i.e.*, Ohmic type conduction process. It is also suggesting that the thermionic emission limited conduction process, where the injection of carrier from the electrodes, has an insignificant role [32]. In LRS, the Ohmic process, leads to conducting filament formation and subsequent high current [33]. However, "tiny conducting filaments", or "residual filaments" exists after dc cycles in the protein film during HRS state, resulting the linear conduction under low-field

region. However, in the higher field region for both resistance states, the electron transport mechanism shows some mysterious behaviors and it seems an entirely different charge transport mechanism. Here increased slope in double logarithmic scale is observed, which may be attributed to increase in the number of electrons trapped after applying high field. The slope "E" in LRS is ~2, which suggest the existence of trap-full space charge conduction region which is explained using the Child's law ($I \propto V^2$) [34]. Again, at high input voltage, the conduction path *i.e.*, conducting filaments dissolution occurs via redox process of the filaments and as well as by Joule heating process inside each and every conducting filament. As a result, a rapid fall in the current level was obtained, which is denoted as RESET process of the device. The slopes from the linear curve fitting in moderate field region of HRS ("B", "C" and "D") are in the range of ~ 1.4 to 1.6, which suggests the Poole–Frenkel (PF) conduction process [35,36]. Thus, we can say that in OFF state the current conduction process of Al/papain/ITO memristor consists of combination of various mechanisms.

IETS is a powerful nondestructive process of studying the structure and defect states of a material. The method analyses the peaks obtained from second derivative of the voltage current characteristics, obtained due to carriers tunneling through the insulator [37–41]. The tunneling occurs in the LRS (ON state) by intermolecular hoping after overcoming carrier scattering within the traps. The tunneling process is aided by the reduction of barrier height due to formation of conducting filament. The tunneling also takes place in OFF state, but here it is assisted by Poole-Frenkel (PF) mechanism occurring due to the reduced protein film. The IETS spectra observed in papain at 77 K are seen in FIG. 5.7(a) for +ve voltage and FIG. 5.7(b) for –ve voltage swipe respectively. The peaks obtained in the 100-460 mV range of the deconvoluted spectra for both bias polarities show the presence of three amide groups (I-III). The peaks at both bias polarities are found in comparatively similar locations; while insignificant peak shift was observed, which may be due to shift in vibrational energy caused by barrier height

changes under bias. The peaks related to vibrations of amide I, II, III are found at ~208.3, 195.6 (forward bias) and 191.3 (reverse bias), and ~ 160 mV, respectively.
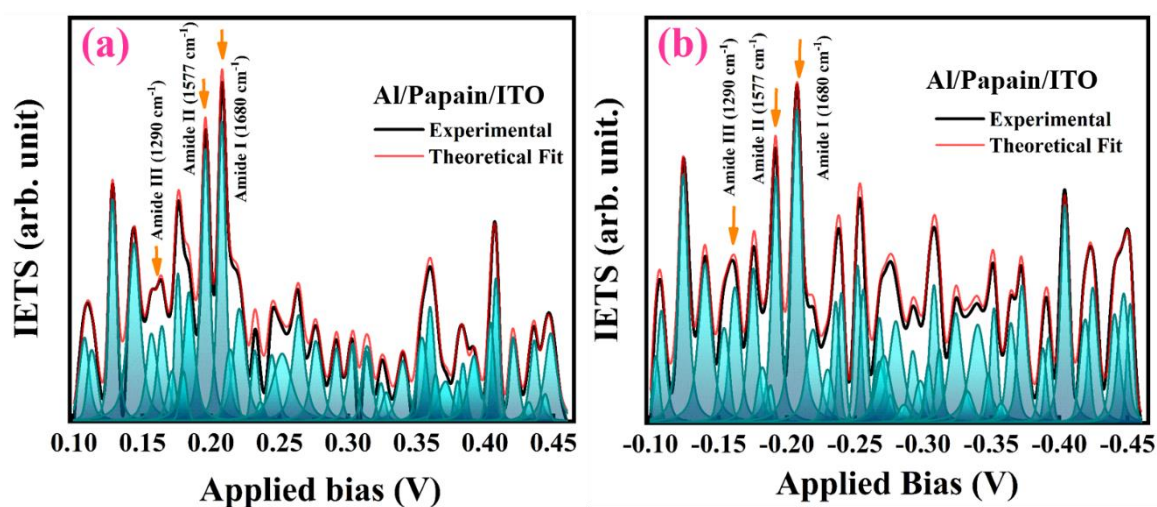
FIG. 5.7. The tunneling spectra of papain at low temperature in both (a) positive and (b) negative bias polarities revealing the existence of amide I, II and III vibrations.

Other vibrations obtained from bending and wagging of C–H, C–C and H-bonds were also observed. The switching event can be observed prominently in the bias range of 0.13-0.2 V in both bias polarities, which reveals that the switching mechanism is primarily governed by β turns and β sheets. During negative bias, the local vibration of these two modes assist in trap induced conduction resulting in LRS. During positive bias, the same molecules play the role of traps and breaks the filament leading to HRS.

5.3.2.4. Mechanism of resistive switching

Based on the above observations, a model for explaining the switching mechanism in the Al/papain/ITO memristor device is proposed with three different possible stages. Before application of any bias, the device is in virgin stage, which is shown in FIG. 5.8(a). However, when the Al is negatively biased, an electrochemical reaction in terms of redox process occurs inside the papain film. In addition, it is observed from the electrical characteristics that the electrodes contribute significantly in the RS characteristics.
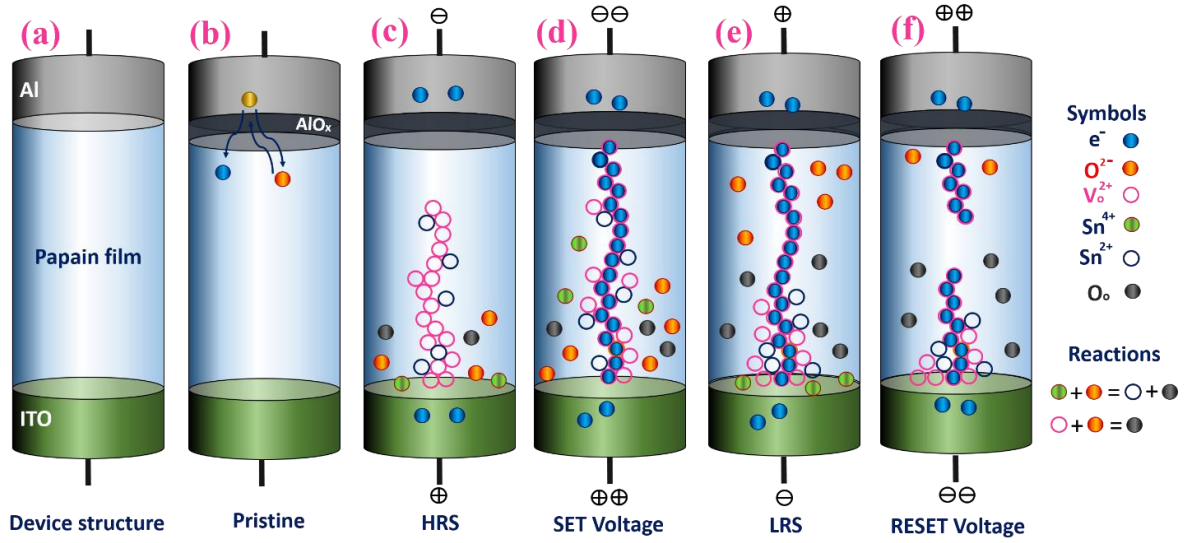
FIG. 5.8. The schematic illustration of the switching mechanism of Al/papain/ITO memristor device under different conditions, such as (a) in virgin, (d) under SET operation and (f) under RESET operation.

For all the devices ITO is used as bottom electrode. ITO acting as source of oxygen ions (O^{2-}) as well as oxygen vacancies has been observed by Yang *et. al.* [42]. At negative bias, O^{2-} drift towards the ITO electrode resulting in oxygen vacancies (V_O^{2+}) in the protein film. It is also reported that ITO has the active Sn^{4+} ions, which plays an important role during the device operation [43].

When negative voltage is applied on Al, several individual mechanisms may come into play to control the output current characteristics of the device. First, an oxidation process will start in the papain film near the top electrode after losing electrons from different molecules, making the film partially positively charged. Secondly, V_O^{2+} from the ITO will start drifting towards the direction of the opposite electrode and get accumulated. Third, the active Sn^{4+} will also enter into the protein film from the ITO. As a result, total positive charge in the protein film will increase and these will form a conducting channel from top to bottom electrode, *i.e.*, conducting filaments at V$_{SET}$, leading the device to its ON or LRS state (see FIG. 5.8(d)). When under positive bias, the migration of O^{2-}, electrons

like negative charged elements towards the top electrode from the ITO is expected. In the meantime, the migration of positive charge elements, such as V_O^{2+} and Sn^{4+} will take place towards the ITO. In this process, a reduction process will occur in the protein film after capturing electrons. Also another reaction will occur between the V_O^{2+} and O^{2-} resulting in formation of neutral oxygen molecules, O_0 ($V_0^{2+} + O^{2-} \rightarrow O_0$). As a result, a rupture mechanism will break the filament and bring the device back to OFF state (FIG. 5.8(f)). However, in this process, the top electrode materials play an important role towards better device performance. In this study Al has higher oxygen affinity compare to all other metal electrodes (ITO, Pt, TiN). Hence, under the application of the positive bias an AlO_x barrier film was formed due to absorption of the migrated O^{2-} ions towards Al/papain interface. Existence of AlO_x layer can also be expressed in terms of Gibbs free energy as the value for Al is more negative (−1582.3 kJ/mol) compare to the other metal electrodes used in this study. This AlO_x layer lowers the current during positive bias. Also, in this stage the conducting filaments are dissolved by means of redox process at the filaments and hence the conducting bridge breaks. As an effect of this two, the current level decreases switching back to HRS. However, at negative bias the dissolution of this barrier layer (AlO_x) results in higher current in the LRS state. Hence, absence and presence of the AlO_x layer along with the formation of conducting filaments are the driving forces for switching mechanism in the protein memristor devices. Table 5.1 shows the comparison of the experimental parameters and Table 5.2 shows the comparison of electrical parameters of the device structure with the reported values of different proteins to find the potential of the performed research.

Table 5.1. The comparison of the experimental parameters of different protein based Memristors

Protein	Substrate	Electrode (s)	Rpm of spin coating	Spinning Time (sec)	Film thickness (nm)	Surface Roughness (nm)	Drying time and temperature	Method used for Deposition of top electrode	Top electrode Thickness (nm) and Area (cm²)	Ref.
Chicken Egg Albumen	ITO/PEN	Top: Al Bottom: ITO	4000	-	~377	-	20 min 120°C	Thermal Evaporation	150 -	[44]
Spider Silk	SiO₂/Si	Top: Ag Bottom: Au	-	-	150	-	-	-	- 4.9×10^{-6}	[45]
Silkworm Hemolymph Proteins	ITO/Glass	Top: Al Bottom: ITO	3000	60	357	-	20 min 100°C	Thermal Evaporation	180 7×10^{-4}	[46]
Silk fibroin	ITO/Glass	Top: Al Bottom: ITO	-	-	400	-	-	Thermal Evaporation	- 1.96×10^{-3}	[7]
DNA	Si	Top: Au Bottom: Au	1000	20	11	0.81	-	Laser MBE	30 1×10^{-2}	[47]
Fructose	ITO/Glass	Top: Al Bottom: ITO	3000	90	110	-	2 hr 50°C	-	200 -	[48]
Fructose	ITO/Glass	Top: Ag Bottom: ITO	3000	90	110	-	2 hr 50°C	-	100 -	[48]
Aloe Vera	ITO/Glass	Top: Al Bottom: ITO	1000	30	350	-	1 hr 50°C	Thermal Evaporation	100 5.03×10^{-3}	[49]
Papain	ITO/Glass	Top: Al Bottom: ITO	3000	60	400		30 min 40°C	Thermal Evaporation	80 1.96×10^{-3}	This work

Table 5.2. The comparison of electrical parameters of different protein based Memristors

| Proteins | V_{SET} (V) | V_{RESET} (V) | Endurance (cycles) | Retention (s) | ON/OFF ratio | Dominating conduction mechanism *HV- High Voltage *LV- Low Voltage | | Resistive switching mechanism | Ref. |
						LRS (ON STATE)	HRS		
Chicken Egg Albumen	-1.0	3.3	>100	>10^4	>10^5	Ohm's Law(L-V), Mott-Gurney law, Child's law (HV)	Ohm's law(L-V), Trap-controlled space-charge-limited current (TC-SCLC) and the trap-filling process (HV)	Formation and rupture of Fe ions based filament	[44]
Spider silk	-4.8	4.2	>100	>500	~60	Ohm's Law	Ohm's Law (LV), Space-charge limited (SCL) (HV)	Migration of Ag ions	[45]
Silkworm Hemolymph	3.49	-1.16	>500	>10^4	>10^3	Ohm's Law	Ohm's Law (LV), Child's law (space-charge-limited current (SCLC)) (HV).	The capture and emission of electrons in conductive filaments	[46]
Silk fibroin	10.4	-11.5	>10	>10^3	~11	-	-	Formation and rupture of metallic filament	[7]
DNA	0.73	-0.85	>100	>10^5	~20	Ohm's Law	Ohm's Law (LV), Trap-controlled space charge limited conduction (SCLC)(HV)	Charge trapping/detrapping in DNA layers	[47]
Al/Fructose	4.2	-1.61	100	10^4	10^6	Ohm's Law	Ohm's Law (LV), space charge limited conduction (SCLC) (HV)	Formation and rupture of metallic filament	[48]
Ag/Fructose	3.4	-1.45	100	10^4	10^5	Ohm's Law (HV), Trap Fill Limited Conduction (LV)	Ohm's Law (LV), space charge limited conduction (SCLC) (HV)	Formation and rupture of metallic filament	[48]
Aloevera	-0.9	3.1	>10^2	>10^4	10^3	space charge limited conduction (SCLC)	space charge limited conduction (SCLC)	-	[49]
Papain	-1.35	1.3	>100	>10^4	~16	Ohm's Law	Ohm's Law (LV), Poole–Frenkel (PF) conduction, Child's law (HV)	Formation and dissolution of the AlO_x layer	This work

In summary, papain from papaya latex based organic, transparent, capacitor has been fabricated with ITO as top and bottom electrode. Papain is found to be a mixture of all the secondary structure characteristics of protein backbone, although *a*-helical groups are found to be the major component. Negative VCC-α and very high dielectric constant ~ 300.4 was observed. The dissipation factor was found to be considerably high which may be due to poor contact adhesion and dielectric defects. The density of dipoles and their permanent dipole moment is estimated using analytical modeling. The charge storage mechanism resembles ionic double layer model that can be further explained using Grotthuss transfer and shows analogy with inorganic MIM capacitors. Papain based memristor has been fabricated with different top electrodes. Bipolar RS have been observed in papain memristor with prominent stability in HRS and LRS states. The conducting filament formation and dissolution by means of the redox process in bulk papain film and the thin AlO_x layer supposed to be the primary cause of the RS behaviour in papain. However, the multiple charge transport mechanism has also been observed. Hence, bipolar RS behavior observed in papain may find its application in bio-inspired memory circuit applications.

Reference:

[1]   O. Olivares *et al.*, "Electrochemical and XPS studies of decylamides of α-amino acids adsorption on carbon steel in acidic environment," *Appl. Surf. Sci.*, vol. 252, no. 8, pp. 2894–2909, 2006.

[2]   S. Barazzouk and C. Daneault, "Amino acid and peptide immobilization on oxidized nanocellulose: spectroscopic characterization," *Nanomaterials*, vol. 2, no. 2, pp. 187–205, 2012.

[3]   R. J. J. Jansen and H. Van Bekkum, "XPS of nitrogen-containing functional groups on activated carbon," *Carbon N. Y.*, vol. 33, no. 8, pp. 1021–1027, 1995.

[4]   Y. Zubavichus *et al.*, "Soft X-ray induced decomposition of phenylalanine and tyrosine: a comparative study," *J. Phys. Chem. A*, vol. 108, no. 20, pp. 4557–4565, 2004.

[5]   S. C. Ezugwu, F. I. Ezema, and P. U. Asogwa, "Synthesis and characterization of ternary CuSbS 2 thin films: effect of deposition time," *Chalcogenide Lett.*, vol. 7, no. 5, pp. 341–348, 2010.

[6]   R. Schlaf *et al.*, "Determination of interface dipole and band bending at the Ag/tris (8-hydroxyquinolinato) gallium organic Schottky contact by ultraviolet photoemission spectroscopy," *Surf. Sci.*, vol. 450, no. 1–2, pp. 142–152, 2000.

[7]   M. K. Hota, M. K. Bera, B. Kundu, S. C. Kundu, and C. K. Maiti, "A Natural Silk Fibroin Protein-Based Transparent Bio-Memristor," *Adv. Funct. Mater.*, vol. 22, no. 21, pp. 4493–4499, Nov. 2012.

[8]   J. C. Kendrew, G. Bodo, H. M. Dintzis, R. G. Parrish, H. Wyckoff, and D. C. Phillips, "A three-dimensional model of the myoglobin molecule obtained by x-ray analysis," *Nature*, vol. 181, no. 4610, pp. 662–666, 1958.

[9]   D. M. Byler and H. Susi, "Examination of the secondary structure of proteins by deconvolved FTIR spectra," *Biopolym. Orig. Res. Biomol.*, vol. 25, no. 3, pp. 469–487, 1986.

[10]   B. D. Hilton and C. K. Woodward, "Nuclear magnetic resonance measurement of hydrogen exchange kinetics of single protons in basic

pancreatic trypsin inhibitor," *Biochemistry*, vol. 17, no. 16, pp. 3325–3332, 1978.

[11]   A. Rygula, K. Majzner, K. M. Marzec, A. Kaczor, M. Pilarczyk, and M. Baranska, "Raman spectroscopy of proteins: a review," *J. Raman Spectrosc.*, vol. 44, no. 8, pp. 1061–1076, 2013.

[12]   T. H. Phung, P. Steinmann, R. Wise, Y.-C. Yeo, and C. Zhu, "Modeling the Negative Quadratic VCC of $\hbox{SiO}_{2}$ in MIM Capacitor," *IEEE electron device Lett.*, vol. 32, no. 12, pp. 1671–1673, 2011.

[13]   A. Sanal, P. Sathyanarayanan, V. Velmurugan, and D. Kannadassan, "Negative VCC in MIM capacitors: modeling and experiments," *J. Comput. Electron.*, vol. 17, no. 1, pp. 458–462, 2018.

[14]   C. Jorel, C. Vallée, P. Gonon, E. Gourvest, C. Dubarry, and E. Defay, "High performance metal-insulator-metal capacitor using a SrTiO 3/ZrO 2 bilayer," *Appl. Phys. Lett.*, vol. 94, no. 25, p. 253502, 2009.

[15]   S. J. Kim *et al.*, "Improvement of voltage linearity in high-/spl kappa/ MIM capacitors using HfO2-SiO2 stacked dielectric," *IEEE Electron Device Lett.*, vol. 25, no. 8, pp. 538–540, 2004.

[16]   M. K. Hota, C. K. Sarkar, and C. K. Maiti, "Frequency-dependent dielectric response of HfTaOx-based metal–insulator–metal capacitors," *Semicond. Sci. Technol.*, vol. 27, no. 8, p. 85002, 2012.

[17]   A. Goswami and A. P. Goswami, "Dielectric and optical properties of ZnS films," *Thin Solid Films*, vol. 16, no. 2, pp. 175–185, 1973.

[18]   C. Y. Kim *et al.*, "Frequency-dependent capacitance-voltage and conductance-voltage characteristics of low-dielectric-constant SiOC (-H) thin films deposited by using plasma-enhanced chemical vapor deposition," *J. Korean Phys. Soc.*, vol. 57, 2010.

[19]   R. K. Goyal and A. B. Kulkarni, "Electrical properties of novel three-phase polymer nanocomposites with a high dielectric constant," *J. Phys. D. Appl. Phys.*, vol. 45, no. 46, p. 465302, 2012.

[20] R. Thomas, D. C. Dube, M. N. Kamalasanan, S. Chandra, and A. S. Bhalla, "Structural, electrical, and low-temperature dielectric properties of sol–gel derived SrTiO 3 thin films," *J. Appl. Phys.*, vol. 82, no. 9, pp. 4484–4488, 1997.

[21] A. L. Lehninger, *Lehninger Principles of Biochemistry: David L. Nelson, Michael M. Cox*. Recording for the Blind & Dyslexic New York, 2004.

[22] J. E. Nielsen and G. Vriend, "Optimizing the hydrogen-bond network in Poisson–Boltzmann equation-based pKa calculations," *Proteins Struct. Funct. Bioinforma.*, vol. 43, no. 4, pp. 403–412, 2001.

[23] A. Noy, "Bionanoelectronics," *Adv. Mater.*, vol. 23, no. 7, pp. 807–820, 2011.

[24] M. Z. Iqbal, F. Wang, H. Zhao, M. Y. Rafique, J. Wang, and Q. Li, "Structural and electrochemical properties of SnO nanoflowers as an anode material for lithium ion batteries," *Scr. Mater.*, vol. 67, no. 7–8, pp. 665–668, 2012.

[25] M. K. Hota, M. N. Hedhili, Q. Wang, V. A. Melnikov, O. F. Mohammed, and H. N. Alshareef, "Nanoscale Cross-Point Resistive Switching Memory Comprising p-Type SnO Bilayers," *Adv. Electron. Mater.*, vol. 1, no. 3, p. 1400035, 2015.

[26] A. H. D. Graham, C. R. Bowen, J. Robbins, G. Lalev, F. Marken, and J. Taylor, "Nanostructured electrodes for biocompatible CMOS integrated circuits," *Sensors Actuators B Chem.*, vol. 147, no. 2, pp. 697–706, 2010.

[27] C.-Y. Lin, C.-Y. Wu, C.-Y. Wu, C. Hu, and T.-Y. Tseng, "Bistable resistive switching in Al2O3 memory thin films," *J. Electrochem. Soc.*, vol. 154, no. 9, p. G189, 2007.

[28] Y. H. Do, J. S. Kwak, J. P. Hong, K. Jung, and H. Im, "Al electrode dependent transition to bipolar resistive switching characteristics in pure TiO 2 films," *J. Appl. Phys.*, vol. 104, no. 11, p. 114512, 2008.

[29] Y.-T. Tsai *et al.*, "Effect of Top Electrode Material on Resistive Switching Characteristics in MnO2 Nonvolatile Memory Devices," *ECS Trans.*, vol. 41, no. 3, p. 475, 2011.

[30] E. Linn, R. Rosezin, C. Kügeler, and R. Waser, "Complementary resistive switches for passive nanocrossbar memories," *Nat. Mater.*, vol. 9, no. 5, pp. 403–406, 2010.

[31] R. Waser, R. Dittmann, G. Staikov, and K. Szot, "Redox-based resistive switching memories–nanoionic mechanisms, prospects, and challenges," *Adv. Mater.*, vol. 21, no. 25–26, pp. 2632–2663, 2009.

[32] S. Mondal, J.-L. Her, F.-H. Ko, and T.-M. Pan, "The effect of Al and Ni top electrodes in resistive switching behaviors of Yb2O3-based memory cells," *ECS Solid State Lett.*, vol. 1, no. 2, p. P22, 2012.

[33] D.-H. Kwon *et al.*, "Atomic structure of conducting nanofilaments in TiO2 resistive switching memory," *Nat. Nanotechnol.*, vol. 5, no. 2, pp. 148–153, 2010.

[34] Y.-S. Fan, P.-T. Liu, L.-F. Teng, and C.-H. Hsu, "Bipolar resistive switching characteristics of Al-doped zinc tin oxide for nonvolatile memory applications," *Appl. Phys. Lett.*, vol. 101, no. 5, p. 52901, 2012.

[35] S. Jung *et al.*, "Resistive switching characteristics of solution-processed transparent TiO x for nonvolatile memory application," *J. Electrochem. Soc.*, vol. 157, no. 11, p. H1042, 2010.

[36] C. Mukherjee, M. K. Hota, D. Naskar, S. C. Kundu, and C. K. Maiti, "Resistive switching in natural silk fibroin protein-based bio-memristors," *Phys. status solidi*, vol. 210, no. 9, pp. 1797–1805, 2013.

[37] R. C. Jaklevic and J. Lambe, "Molecular vibration spectra by electron tunneling," *Phys. Rev. Lett.*, vol. 17, no. 22, p. 1139, 1966.

[38] I. Giaever and K. Megerle, "Study of superconductors by electron tunneling," *Phys. Rev.*, vol. 122, no. 4, p. 1101, 1961.

[39] A. G. Chynoweth, R. A. Logan, and D. E. Thomas, "Phonon-assisted tunneling in silicon and germanium Esaki junctions," *Phys. Rev.*, vol. 125, no. 3, p. 877, 1962.

[40] C. Petit and G. Salace, "Inelastic electron tunneling spectrometer to characterize metal–oxide–semiconductor devices with ultrathin oxides," *Rev. Sci. Instrum.*, vol. 74, no. 10, pp. 4462–4467, 2003.

[41] W. He and T. P. Ma, "Inelastic electron tunneling spectroscopy study of traps in ultrathin high-k gate dielectrics," *Appl. Phys. Lett.*, vol. 83, no. 26, pp. 5461–5463, 2003.

[42] M. Yang *et al.*, "Enhanced resistance switching stability of transparent ITO/TiO2/ITO sandwiches," *Chinese Phys. B*, vol. 19, no. 3, p. 37304, 2010.

[43] C. Ye *et al.*, "Low-power bipolar resistive switching TiN/HfO2/ITO memory with self-compliance current phenomenon," *Appl. Phys. Express*, vol. 7, no. 3, p. 34101, 2014.

[44] C. H. Bok, S. J. Woo, C. Wu, J. H. Park, and T. W. Kim, "Flexible bio-memristive devices based on chicken egg albumen:Au@SiO(2) core-shell nanoparticle nanocomposites.," *Sci. Rep.*, vol. 7, no. 1, p. 12033, Sep. 2017.

[45] B. Sun, D. Liang, X. Li, and P. Chen, "Nonvolatile bio-memristor fabricated with natural bio-materials from spider silk," *J. Mater. Sci. Mater. Electron.*, vol. 27, no. 4, pp. 3957–3962, 2016.

[46] L. Wang and D. Wen, "Nonvolatile Bio-Memristor Based on Silkworm Hemolymph Proteins," *Sci. Rep.*, vol. 7, no. 1, p. 17418, 2017.

[47] S. Qin, R. Dong, X. Yan, and Q. Du, "A reproducible write–(read)n–erase and multilevel bio-memristor based on DNA molecule," *Org. Electron.*, vol. 22, pp. 147–153, 2015.

[48] Y. Xing, B. Sueoka, K. Y. Cheong, and F. Zhao, "Nonvolatile resistive switching memory based on monosaccharide fructose film," *Appl. Phys. Lett.*, vol. 119, no. 16, p. 163302, 2021.

[49] Z. X. Lim and K. Y. Cheong, "Effects of drying temperature and ethanol concentration on bipolar switching characteristics of natural Aloe vera-based memory devices," *Phys. Chem. Chem. Phys.*, vol. 17, no. 40, pp. 26833–26853, 2015.

Chapter 6: Highly Transparent Soluble Substrates from Waste Material for Green Electronic Device Applications

6.1. Introduction

In the previous two chapters the functionality of 'Proteotronic' devices using animal protein (BSA) and plant protein (Papain) as dielectric materials, has been demonstrated as a solution for sustainable electronics. However, the protein-based devices were fabricated on plastic PET (BSA based device) and glass (papain based device), both of which are transparent inorganic substrates. In the way to green electronics, it is necessary to fabricate devices made entirely of biocompatible or green materials that are transient and bio-degradable at the same time. Here, in this chapter the fabrication of a novel, transient, bio-degradable, transparent protein bio-polymer substrate made of gelatin obtained from fish scales is discussed in detail. Finally, the study of the electrical characteristics of MIM capacitor fabricated on the bio-polymer substrate using BSA as dielectric layer is investigated. The chapter will provide a new dimension to all-green device electronics that will be of immense importance in future eco-friendly campaigns.

Gelatin is a translucent, brittle, and colourless protein bio-polymer hydrogel obtained from collagen i.e. the main component of fish scales. Fish industry widely produces fish scales as a by-product, which entirely contributes to waste materials. Fish scales comprise of 3% of fish produced annually. Collagen seen under microscope shows amino acid bounded elongated fibrils of triple helix structure [1], arranged orthogonally in a hydroxyapatite matrix [2]. Collagen has the property of moisture activated adhesion, and excellent micro-molding making it suitable for solid devices.

Collagen denaturates mainly by altering its secondary and tertiary structure, and partially its primary structure to form gelatin. Gelatin has hydrogen

bond which can be broken easily to exhibit a sol-gel transition property. Gelatin gel is highly viscous and has good mechanical strength [3].

Gelatin has been previously used in various electronic devices. Gelatin has been used in production of microneedles with fish scales [4-6], using a mechanical press method. The micro-needles had enough strength to be used in drug delivery, cosmetic industry by piercing animal skin. pH modified gelatin has been used in organic electrochemical transistor for various electronic sensing applications [7]. Gelatin has also been used in alternate current electroluminescent device that showed a 56 cd m^{-2} luminescence at 300 V applied and 400 Hz frequency [8].

In this chapter, the gelatin obtained from fish scales have been used to fabricate biopolymer substrate (BPS) using hydrolysis method. The structural, morphological, and optical characteristics of the fabricated substrate were studied. Flexural, and tensile properties of the BPS were studied. The substrate was subjected to dissolvability and biodegradability tests. Finally, BPS was used to fabricate a novel organic MIM capacitor using bovine serum albumin (BSA) as dielectric. The electrical characteristics of the device were studied that included the capacitance voltage characteristics and the leakage current. The possible potential applications of BPS in future device electronics are discussed.
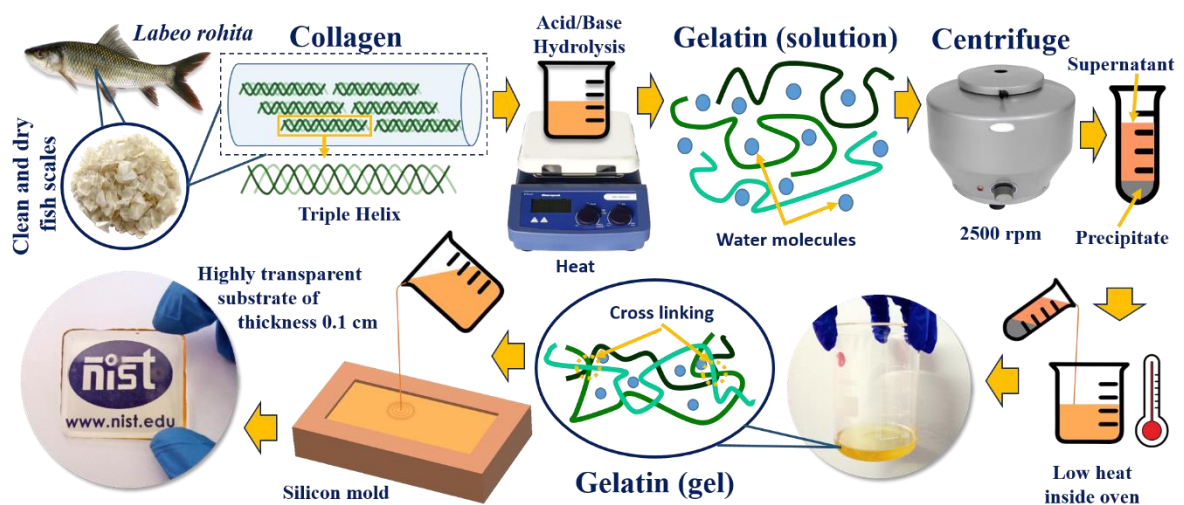
6.2. Methods and Materials

FIG. 6.1. Fabrication process of BPS starting from raw material fish scales.

BPS fabrication process from fish scale is shown in FIG. 6.1. Gelatin extracted from Rohu (Labeo Rohita sp.) fish scales was used to fabricate the BPS. At first, visible impurities such as dirt, skin were washed using normal water. Then the scales were kept under sun for drying, followed by storage in freezer for further usage. The thawed scales (100 gms) were then processed to eliminate non-collagen materials by treating with 0.1M NaOH. NaoH treated scales were washed in DI water and the treated scales were dipped into 10% HCl solution for removing traces of minerals such as calcium carbonate, and hydroxyapatite etc. found in fish scales. After further washing with DI water, the scales were dried again. Dried scales were hydrolysed in an airtight container at a temperature of 80 ^{0}C. After hydrolysis the supernatant was separated and then centrifuged (REMI C) for 15 minutes at 2500 rpm. Silicon molds were used to pour the centrifuged fluid and kept at room temperature for 48 hours. The substrate, thus solidified was peeled off from the mold cautiously. Substrate transmittance was investigated using spectrophotometer (Shimadzu UV-1800) operating in UV and visible wavelength range (300-800 nm). Optical microscope (OLYMPUS – ESAW Optoscopes Classic) was used to observe the surface profile, while AFM (Nano surf easyscan2) was used to estimate the surface roughness. FTIR spectrometer (Alpha II, Labindia Analytical instruments Pvt. Ltd.) was used to study the film's structural characteristics in 900-4000 cm^{-1} wavenumber range. The contact angle was measured employing contact angle metre (Kyowa Interface Science Co. Ltd. DMs-401) equipped with video capture. 3D printer (Flashforge Creator Pro2) prepared molds for substrate preparation for mechanical testing, which is then studied by using the universal tensing equipment (Deesha Impex, model no-DTD10KN). The surface of the fabricated BPS was cleaned using Argon (Ar) plasma of 24 W power at 2×10^{-2} Torr pressure ambience [9]. Titanium (Ti) layer of 20 nm was deposited immediately after cleaning, followed by 100 nm Platinum (Pt) deposition using Cressington Sputter Coater 108auto/SE at a pressure of 10^{-3} in Ar atmosphere. The metal coated substrate was then kept in vacuum for 72 hours. Deposited Pt film's sheet resistance was found to be 1.06 Ohm/sq using

four probe method. BSA was procured from Sigma Aldrich (A2058). Aqueous solution of BSA was deposited on the Pt coated BPS by spinning at 2500 rpm for 30 secs. The coated sample was dried for 2 hr at 40 ^{0}C. The coated sample was then metalized with Al dot masks in thermal evaporator (Hind High Vac BC 300), with circular dot area of 1x10^{-3} cm^2 each. Agilent E4980A precision LCR meter and Keithley 2604B Source meter were used to study the capacitance density and leakage current of the device.

6.3. Results and Discussions

6.3.1. Physical Characterizations

Mass of the produced BPS can be correlated with mass of the raw fish scales to calculate the process yield (η) as shown in equation (6.1). It is the numerical ratio of dry mass of substrate (mass$_{sub}$) to the dry mass of the fish scales (mass$_{scales}$) used [4]. The yield in this process was found to be 30±1 %.

$$\eta(\%) = \frac{mass_{sub}}{mass_{scales}} \times 100 \qquad (6.1)$$

The mass of the gelatin liquid deposited in the mold was plotted with time as shown in FIG. 6.2(a). The decrease in mass with time indicates initial presence of moisture that gradually reduces. The solidified substrate was initially flexible in nature with 28.5 HA value of shore hardness, but gradually hardened with time, changing to 90 HA shore value in 7 days. Moisture content analysis was done with a BPS of mass 3.34 gm, oven-heated at 60 $^{\circ}$C and weighed every 20 mins, until a constant weight is observed. Using the equation below, the moisture content was calculated in percentage [6], and was found to be 24±1%.

$$M(\%) = \frac{\left(wt_{initial} - wt_{final}\right)}{wt_{final}} \times 100 \qquad (6.2)$$

The surface of BPS was observed with an optical microscopic operated in reflectance mode at 20X resolution as shown in FIG. 6.2(a) (inset). The surface

exhibited continuous and homogeneous morphology suggesting good adhesion of liquid gelatin. The study of transparency of the BPS is shown in FIG. 6.2(b), where four substrates of different thicknesses viz. 0.1 cm, 0.11cm, 0.17 cm, and 0.3 cm were observed using UV-Vis spectrophotometer and the percentage transmittances were calculated. The substrate of thickness 0.1 cm showed highest transparency of 90%, with the corresponding absorption co-efficient value 5.29 cm^{-1} at 3.5 eV. The penetration length before absorption of light can be estimated using absorption co-efficient, and its low value denotes nearly transparent material.
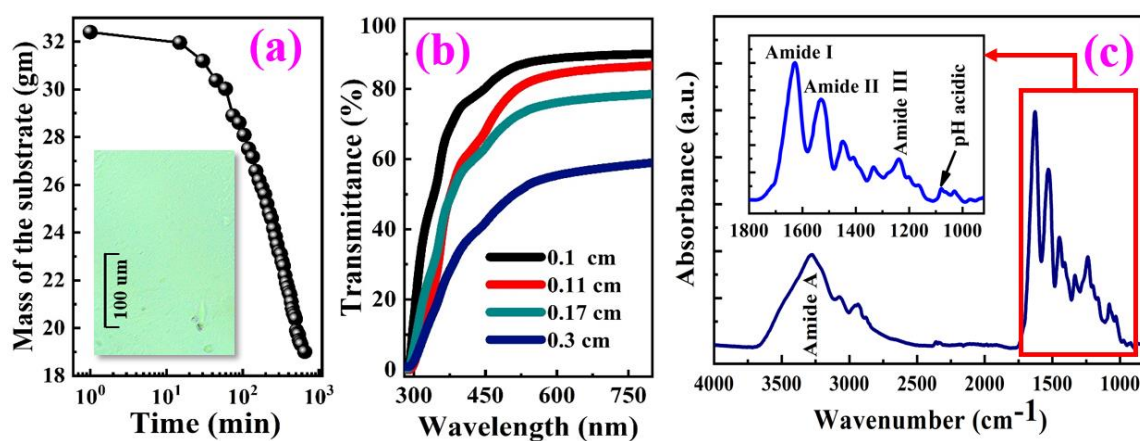
FIG. 6.2. (a) Mass of BPS measured at different time intervals right after deposition, image of the surface of BPS obtained using optical microscopic (inset); (b) Percentage transmittance of BPS of different thicknesses 0.1,0.11cm, 0.17 cm, 0.3 cm plotted against wavelength; (c) FTIR-ATR absorbance spectra of the BPS plotted against wavenumber.

The structural characteristics of the BPS is studied using FTIR–ATR and the resultant spectrum is shown in FIG. 6.2(c). The major peaks are found at 3282, 1623, 1526, and 1236 cm^{-1}, while small peaks are observed at 3072, 2936, 2356, 1448, 1077, and 507 cm^{-1}. The peaks at 3282, 1623, 1526, 1236 cm^{-1} correspond to amide A (hydroxyl and amino group), amide I, amide II, and amide III denoted by C=O stretching, N-H bending or C-N stretching, and C-N or N-H or CH$_2$ vibration, respectively, which is similar to previous reported values of gelatin [8], [10–12].
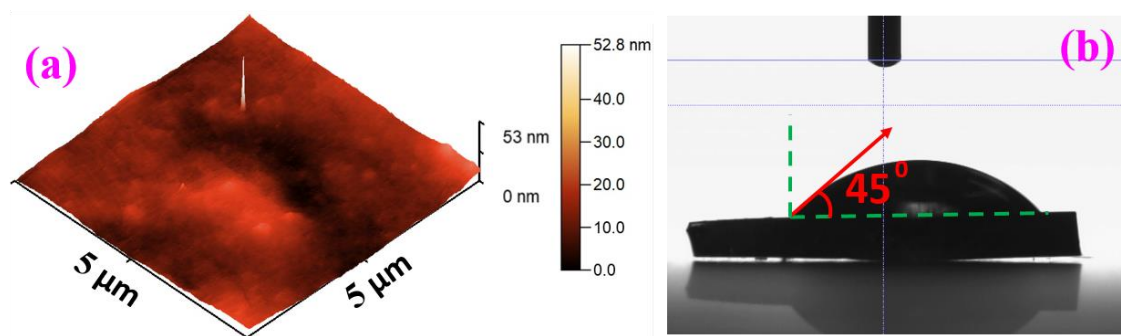
FIG. 6.3. (a) Surface morphology of the BPS studied using AFM in 5μm x 5μm area; (b) Contact angle measurement on the surface of BPS.

Intensity of amide A bond at 3282 cm^{-1} is found to be diminished compared to amide II bond at 1526 cm^{-1}, owing to little presence of moisture in the substrate [5]. The small peak at 1077 cm^{-1} (FIG. 6.2(c) inset) denote the substrate to be acidic due to the presence of carboxyl group [7].

Surface properties of the BPS is crucial in deciding the quality of the metal contact deposition on the substrate. The surface topography of the BPS in 5μm × 5 μm area is shown in FIG. 6.3(a), where the mean surface roughness (r.m.s.) was found to be 1.9 nm, much lower than the roughness of cellophane paper (r.m.s. value 3.2 nm) [8]. Comparatively small value of surface roughness of the BPS makes it suitable for the electronic substrate application.

Contact angle (CA) on the surface of BPS was measured using the method termed as Sessile drop. A 5 L droplet of distilled water and the method of half angle fitting was used for measuring the static contact angle values. The result taken was the average of ten measurements for each set of samples. The 45°±5° contact angle was obtained on BPS surface using goniometer, which indicates its hydrophilic nature (FIG. 6.3(b)), which has also been observed from the FTIR analysis as well. FTIR analysis (FIG. 6.2(c)) already showed the presence of different functional hydrophilic groups such as amide, carbonyl. Moreover, from AFM investigation, low surface roughness was estimated around 1.91 nm. Surface chemistry and morphological analysis both have confirmed that the surface of the BPS was quite smooth as well as hydrophilic in nature.

6.3.2. Solubility and bio-degradability

The dissolution of BPS in water at room temperature is shown in FIG. 6.4(a-d). The substrate completely dissolved in 30 minutes at room temperature. Dissolution of BPS may be attributed to breakdown of hydrogen bonds that is responsible for cross-linking of the polypeptide chains. BPS dissolved much faster at higher temperature (60 ^{0}C), it was found to dissolve in 15 mins as shown in FIG. 6.5(a-d), this may be due to accelerated breakage of polypeptide chains with increase in water temperature [8]. The dissolved BPS can be regained by re-solidification. The recycled substrate has similar transparency and other properties as the pristine substrate. Solidification of gelatin can be explained as loss of water molecules and also intra crosslinking of protein chains from micro to macrostructure.
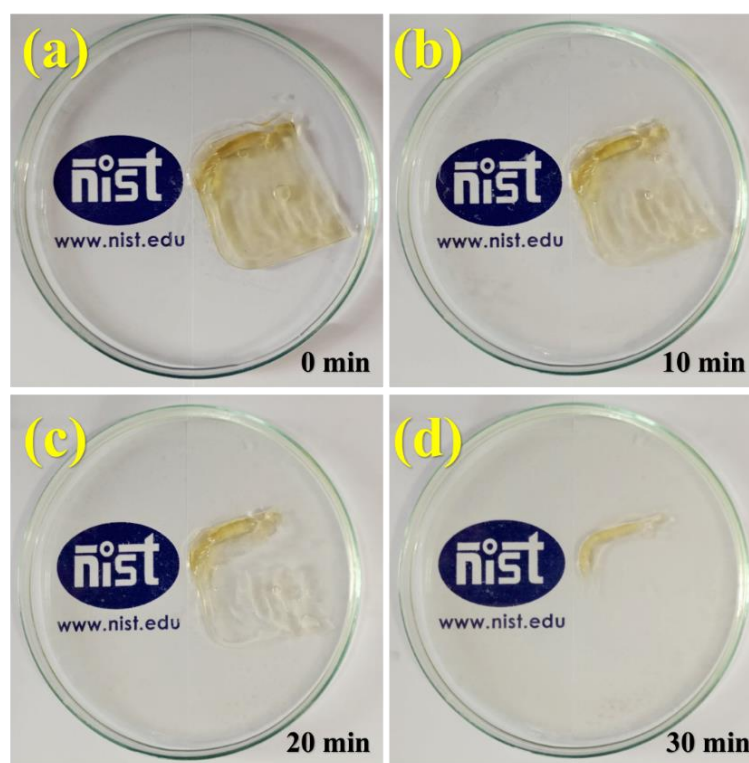
FIG. 6.4. BPS dissolution in water at room temperature noted (a) at immersion; (b) after 10 mins; (c) after 20 mins; (d) after 30 mins.
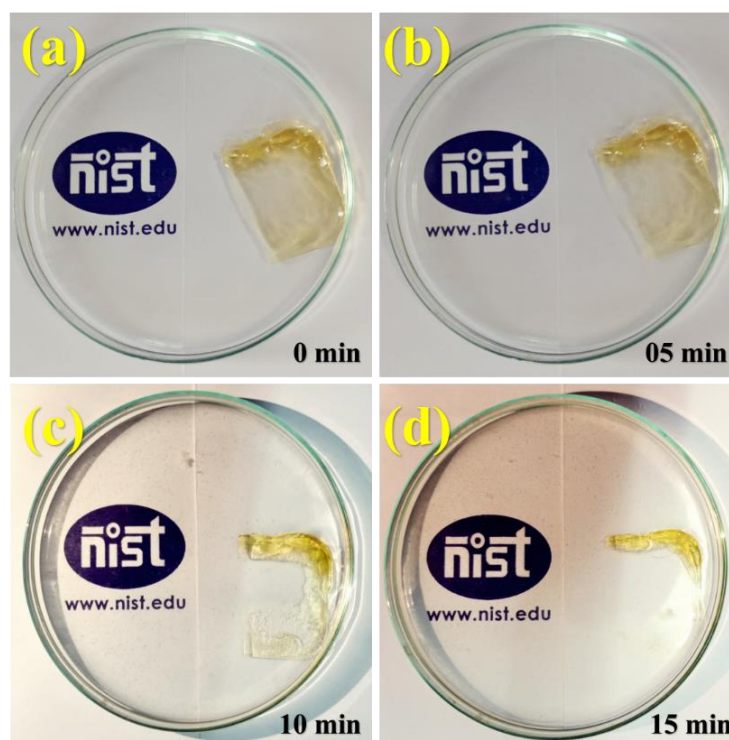
FIG. 6.5. Dissolution of fish BPS in water at 60 ^{0}C temperature shown at different time duration (a) at immersion; (b) after 5 mins; (c) after 10 mins; (d) after 15 mins.

The solubility of fish BPS is compared with other existing organic and inorganic flexible substrates and shown in Table 6.1.

Table 6.1. Comparison between properties of different flexible electronic substrates

Substrates	Properties				
	Thickness	soluble	Solvent	Time to dissolve	Ref.
1. Fish BPS	1 mm	yes	water at 60 ^{0}C	15 min	This work
2. PET	0.2 mm	no	-	-	[13]
3. PDMS	4.5 mm	yes	pentane, xylenes.	-	[14]
4. Cellulose paper	200 µm	yes	water	30 min	[15]
5. Silk	20-60 µm	yes	water	15 min	[16]
6. PLGA	2 mm/10-20 µm	yes	PBS	Few months	[17]
7. PVA	30 µm	yes	water	1800 sec	[18]
8. c-PPA	40 µm	yes	UV light and HCl	230 min	[19]
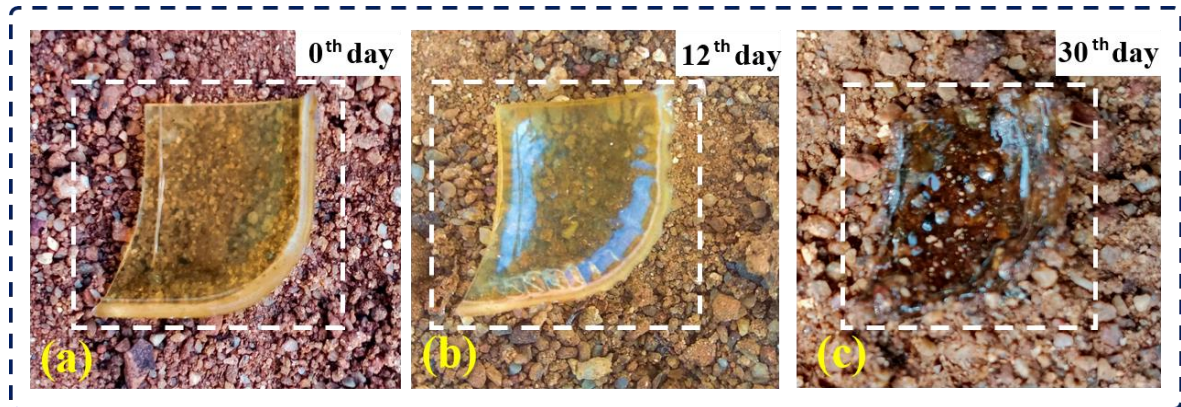
FIG. 6.6. Bio-degradation of BPS in natural soil at natural cloudy environment in (a) day 0; (b) day 12; and (c) day 30.

BPS has natural bio-degradable property as shown in FIG. 6.6(a-c). The study was conducted at average 21°C temperature (max.: 25°C; min.: 16°C) on natural soil in a cloudy environment. It was observed on the 12th day that the substrate has become significantly transparent (FIG. 6.6(b)). It was seen that the BPS degraded more than 90% in 30 days that may also be due to presence of moisture owing to the cloudy environment. The bio-degradability can be explained as the compatibility with micro-organisms present in the soil and also to environmental humidity.

6.3.3. Mechanical Characterizations

Tensile and flexural tests were done to study the mechanical properties of BPS. To carry out the experiments two molds of dimensions 65×15×3 mm (l×b×w), and 40×20×3 mm (l×b×w) were prepared as shown in FIG. 6.7(a) using 3D printer shown in FIG. 6.7(a) (inset) for tensile, and flexural characterizations, respectively. These molds were used to solidify and pertain desired shapes to the deposited liquid substrate as shown in FIG. 6.7(b). The solidification was done at room temperature. The solidified substrates were detached from the mold and used as samples to perform mechanical experiments as shown in FIG. 6.7(c).
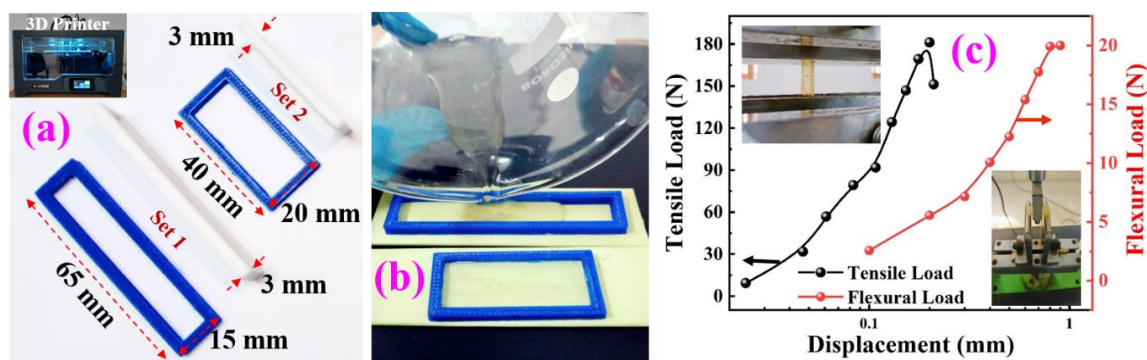
FIG. 6.7. (a) 3D printer Flashforge Creator Pro2 (inset); sample preparation molds used for mechanical characterization experiments prepared with 3D printer; (b) Picture of liquid substrate deposition onto the polymer molds; (c) Graph showing relation between tensile and flexural load with displacement; images of flexural and tensile measurement of BPS (inset).

The ductility, stiffness and strength of the BPS were studied using the tensile test that may give an insight of the appropriateness of BPS for device applications. A moveable jaw with displacement rate of 1.5 mm/min was used at room temperature. The 60×15×3 mm substrate obtained after solidification was cut to resemble test settings of ASTM standard, as it is required to simulate the real conditions for a tensile test [20,21].

The result obtained was the average values of three specimens measured separately and the values were found to be consistent. One movable and another fixed jaw were used to hold the sample for testing such that the gauge length is suitable. Care was taken to avoid slipping of sample and introduction of unnecessary frictional force by consciously adjusting the clamping.

Tensile strength was calculated using the equation $\sigma = P/WT$, where tensile strength of the specimen is denoted by σ, maximum tensile load is P, specimen's width and thickness are W and T, respectively. The tensile behavior shows (FIG. 6.7(c)) that BPS is fully brittle in nature, and prone to cracking and breaking under stress like many other natural resins. The measurement image during tensile test is shown in FIG. 6.7(c) (left inset). The ultimate tensile force was found to be 180±2 N, with 0.2 mm displacement. Based on the above equation, tensile strength of 4 MPa was calculated.

To determine the substrate's resistance to bending force and to deformation, flexural study is important. Performance of various composite organic materials can also be compared using this test. The BPS samples used for flexural test were cut according to the dimension of 35×14×3 mm as specified in the ASTM standard [22]. Three specimens were used to consider average of the three measurements. Flexural strength can be determined using the equation $\sigma_b=3PL/2WT^2$, where flexural strength is denoted by σ_b, the maximum bending load is P at which the specimen is subjected to maximum stress, the specimen's thickness, width, and length are T, L, and W respectively. FIG. 6.7(c) shows the relationship between flexural load and corresponding displacement for BPS. As seen from the graph the substrate lacks mechanical flexibility and is brittle in nature. At the end of the experiment the substrate broke with a loud shattering noise. However, it was noted that, inspite of significant level of deformation along the direction of the applied load, there was minor change in dimension. The sample in flexural test under strain is shown in right inset of FIG. 6.7(c). The maximum deformation value was 0.91 mm corresponding to maximum load of 20±3 N. It was calculated that the BPS exhibited a flexural strength of 8.33 MPa. The mechanical properties of other green materials are compared in Table 6.2.

Table 6.2. Comprehensive mechanical properties of Green materials

Material	Type	Biodegradable	Sample dimensions (mm)		Tensile Strength (MPa)	Flexural Strength (MPa)	Ref.
			Tensile	Flexural			
Cochlospermum Gossypium (CG)	Plant protein	Yes	165×19× 3	127 ×12.7×3	1.6	1.04	[23]
Soy Protein Resin	Plant protein	Yes	165×13× 4	12.7×64 ×3.2	7.19	12.41	[24]
Polylacticacid (PLA)	Plant protein	Yes	120×20/13×3	70×15×8	14.68	27.87	[25]
BPS	Fish scales	Yes	65×15×3	40×20×3	4	8..33	This work

6.3.4. Biopolymer substrate in electronic device fabrication

The image of BPS coated with 100 nm Pt film is shown in FIG. 6.8(a), and the surface properties of the Pt film was studied by AFM as shown in FIG. 6.8(b). 10×10 μm² surface area was used for scanning and it does not show any discontinuity or cracks. 5.69 nm (r.m.s. value) is the average roughness obtained on the surface, that denotes a significant high quality of the metallized surface for device fabrication. Al/BSA/Pt/BPS device was fabricated to study its characteristics as MIM capacitor as shown in FIG. 6.8(c). The capacitance density was plotted against applied voltage at 200 kHz to 1 MHz frequency as shown in FIG. 6.8(d). 1.2 fF/μm² capacitance density was found at 1MHz applied frequency at 1 V. The frequency dispersion seen in the CV characteristics is similar to other inorganic MIM structures [13].
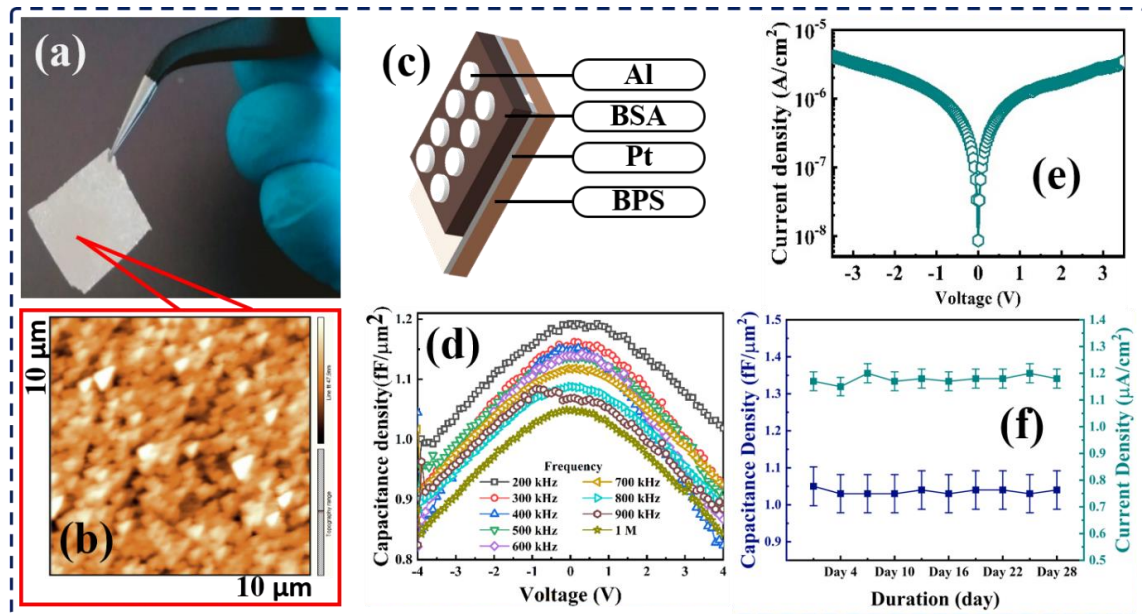
FIG. 6.8. (a) Image of Pt coated BPS post-sputtering; (b) The surface morphology of the Pt film on BPS; (c) Schematic diagram of the Al/BSA/Pt MIM device structure used as MIM capacitor; (d) Capacitance density versus voltage curve (CV) of the fabricated MIM capacitor at different frequencies (200 KHz – 1MHz); (e) Current density plotted against applied voltage for the MIM device; (f) the capacitance and current density plotted against time for the duration of 28 days.

The leakage current density was plotted against applied voltage and is shown in FIG. 6.8(e), the value of leakage current density at 1 V was found to be 1.15 $\mu A/cm^2$. This denotes even metal contact formed on the substrate. The time-dependent current density and capacitance is shown in FIG. 6.8(f) studied on the fabricated MIM structure for 28 days. The values of capacitance and current density were found to be nearly constant and no major degradation was observed. This indicates that the device exhibits good reliability and can be used in future electronic applications. A comparison of electrical properties of the BSA based MIM structure fabricated on ITO-PET [13], and BPS is shown in Table 6.3.

Table 6.3. A comparison between BSA based MIM structures fabricated on ITO-PET and BPS

Device Structure	Coating method	Bottom electrode roughness (nm)	Capacitance density @ 1 MHz ($fF/\mu m^2$)	Current density at 1 V ($\mu A/cm^2$)	Ref.
Al/BSA/ITO/PET	Spin Coating	4.8	0.26	0.12	[13]
Al/BSA/Pt/BPS	Spin Coating	5.69	1.05	1.15	This work

In Summary, we have successfully fabricated gelatin based transparent, transient and bio-degradable polymer substrate from raw fish scales (Labeo Rohita sp.). The substrate was prepared by simple solution casting method at room temperature. The morphological property of the prepared substrate was good with surface roughness of 1.91 nm which is lower than cellophane paper. The substrate also exhibited very high transparency showing 90 % transmittance value. The mechanical properties of BPS are suitable for application as non-flexible substrate in electronic devices. It was shown that the substrate was renewable and can give an edge to re-usable electronics. The MIM structure fabricated as Al/BSA/Pt/BPS, showed good electrical characteristics similar to previously reported MIM structures, confirming the substrate's feasibility in electronic devices. The study of exploring a waste material in production of a promising substrate for electronic devices, not only helps in waste management

but also adds value to aquatic resources. It is hoped that in near future ITO coated glass substrates commercially available will be eventually replaced with metal coated BPS. 4 MPa tensile strength, and 8.33 MPa flexural strength were found in the mechanical tests, which denote brittle nature of the substrate. There is a scope for engineering mechanical properties of the BPS to be applied in flexible electronics domain in near future. Transient materials are hydrophilic and can readily dissolve in water and thus special caution is required during device fabrication. Overall, the concept of transient electronics and disposal of electronic wastes, will increase environmental affability with the ecosystem in long term.

Reference:

[1]   L. E. R. O'leary, J. A. Fallas, E. L. Bakota, M. K. Kang, and J. D. Hartgerink, "Multi-hierarchical self-assembly of a collagen mimetic peptide from triple helix to nanofibre and hydrogel," *Nat. Chem.*, vol. 3, no. 10, pp. 821–828, 2011.

[2]   T. Ikoma, H. Kobayashi, J. Tanaka, D. Walsh, and S. Mann, "Microstructure, mechanical, and biomimetic properties of fish scales from Pagrus major," *J. Struct. Biol.*, vol. 142, no. 3, pp. 327–333, 2003.

[3]   F. Zhang, S. Xu, and Z. Wang, "Pre-treatment optimization and properties of gelatin from freshwater fish scales," *Food Bioprod. Process.*, vol. 89, no. 3, pp. 185–193, 2011.

[4]   O. Olatunji, C. C. Igwe, A. S. Ahmed, D. O. A. Alhassan, Gg. O. Asieba, and B. Das Diganta, "Microneedles from fish scale biopolymer," *J. Appl. Polym. Sci.*, vol. 131, no. 12, 2014.

[5]   O. Olatunji and R. T. Olsson, "Microneedles from fishscale-nanocellulose blends using low temperature mechanical press method," *Pharmaceutics*, vol. 7, no. 4, pp. 363–378, 2015.

[6]   O. Olatunji, M. Olubowale, and C. Okereke, "Microneedle-assisted transdermal delivery of acetylsalicylic acid (aspirin) from biopolymer films extracted from fish scales," *Polym. Bull.*, vol. 75, no. 9, pp. 4103–4115, 2018.

[7]   Y. J. Jo, K. Y. Kwon, Z. U. Khan, X. Crispin, and T. Kim, "Gelatin hydrogel-based organic electrochemical transistors and their integrated logic circuits," *ACS Appl. Mater. Interfaces*, vol. 10, no. 45, pp. 39083–39090, 2018.

[8]   X. Zhang *et al.*, "Sustainable and transparent fish gelatin films for flexible electroluminescent devices," *ACS Nano*, vol. 14, no. 4, pp. 3876–3884, 2020.

[9]   Y. Xiang, T. Li, Z. Suo, and J. J. Vlassak, "High ductility of a metal film adherent on a polymer substrate," *Appl. Phys. Lett.*, vol. 87, no. 16, p. 161910, 2005.

[10] S. M. Pawde and K. Deshmukh, "Characterization of polyvinyl alcohol/gelatin blend hydrogel films for biomedical applications," *J. Appl. Polym. Sci.*, vol. 109, no. 5, pp. 3431–3437, 2008.

[11] Q. Xing, K. Yates, C. Vogt, Z. Qian, M. C. Frost, and F. Zhao, "Increasing mechanical strength of gelatin hydrogels by divalent metal ion removal," *Sci. Rep.*, vol. 4, no. 1, pp. 1–10, 2014.

[12] M. C. Chang, C.-C. Ko, and W. H. Douglas, "Preparation of hydroxyapatite-gelatin nanocomposite," *Biomaterials*, vol. 24, no. 17, pp. 2853–2862, 2003.

[13] P. Kumar *et al.*, "Flexible BSA MIM capacitor with negative voltage coefficient for RF applications," *Appl. Phys. Lett.*, vol. 116, no. 17, p. 171904, 2020.

[14] J. N. Lee, C. Park, and G. M. Whitesides, "Solvent compatibility of poly (dimethylsiloxane)-based microfluidic devices," *Anal. Chem.*, vol. 75, no. 23, pp. 6544–6554, 2003.

[15] Y. H. Jung *et al.*, "High-performance green flexible electronics based on biodegradable cellulose nanofibril paper," *Nat. Commun.*, vol. 6, no. 1, pp. 1–11, 2015.

[16] S. Mohanty *et al.*, "Potential soluble substrates for transient electronics applications: A review," *AIP Adv.*, vol. 12, no. 5, p. 50701, 2022.

[17] S. Hwang *et al.*, "High-performance biodegradable/transient electronics on biodegradable polymers," *Adv. Mater.*, vol. 26, no. 23, pp. 3905–3911, 2014.

[18] S. H. Jin *et al.*, "Solution-processed single-walled carbon nanotube field effect transistors and bootstrapped inverters for disintegratable, transient electronics," *Appl. Phys. Lett.*, vol. 105, no. 1, p. 13506, 2014.

[19] H. L. Hernandez *et al.*, "Triggered transience of metastable poly (phthalaldehyde) for transient electronics," *Adv. Mater.*, vol. 26, no. 45, pp. 7637–7642, 2014.

[20] A. Ekinci, A. A. Johnson, A. Gleadall, and X. Han, "The effect of geometry on tensile strength of biodegradable polylactic-acid tensile-test specimens by material extrusion," *Int. J. Rapid Manuf.*, vol. 10, no. 1, pp. 23–35, 2021.

[21] M. Hervy, A. Santmarti, P. Lahtinen, T. Tammelin, and K.-Y. Lee, "Sample geometry dependency on the measured tensile properties of cellulose nanopapers," *Mater. Des.*, vol. 121, pp. 421–429, 2017.

[22] S. ASTM, "Standard test methods for flexural properties of unreinforced and reinforced plastics and electrical insulating materials. ASTM D790," *Annu. B. ASTM Stand.*, 1997.

[23] V. Srikanth and K. R. N. Reddy, "Investigation of thermo-mechanical properties of Cochlospermum Gossypium composite materials with inserted OPM fibre," *Proc. Inst. Mech. Eng. Part E J. Process Mech. Eng.*, p. 09544089231152714, 2023.

[24] P. Saenghirunwattana, A. Noomhorm, and V. Rungsardthong, "Mechanical properties of soy protein based 'green' composites reinforced with surface modified cornhusk fiber," *Ind. Crops Prod.*, vol. 60, pp. 144–150, 2014.

[25] R. Siakeng, M. Jawaid, H. Ariffin, and S. M. Sapuan, "Mechanical, dynamic, and thermomechanical properties of coir/pineapple leaf fiber reinforced polylactic acid hybrid biocomposites," *Polym. Compos.*, vol. 40, no. 5, pp. 2000–2011, 2019.

Chapter 7: Conclusion and Future Scope

An emerging domain of electronics called 'Proteotronics' has already been developed to study the electronic applications of proteins. This thesis reports protein based electronic charge storage devices as well as UV photoactive device, eventually leading to complete protein based green gadgets, as mentioned in our objective. To learn more about the topic at hand, a lot of literature research has been done. The enormous potential of transient electronics and the potential for creating a wide range of devices on transient substrates, including organic and polymer substrates, have been reviewed. In chapters 4 and 5, the characteristics of MIM and memristor devices based on animal and plant proteins are studied. In chapter 4 BSA based UV photoactive device has also been investigated. Chapter 6 examines biodegradable protein substrate and its device applications, and shows the path to green electronics. The thesis concludes with observations on the prospects for the major research areas discussed in this work.

With an eye towards future implantable biocompatible integrated circuits and creative healthcare applications, we hope that this study will encourage multidisciplinary debates and investigations on subjects like bio- and bio-inspired electronics.

7.1. Main conclusions of this dissertation

Electronic-grade BSA was used to create flexible organic metal-insulator-metal capacitors that display high transparency over the majority of the visible spectrum. Spin coating was used to create the thin BSA films on the ITO-coated PET substrate. With negative VCC-α value, a good capacitance density of 0.26 fF/m^2 was attained. Additionally, an analogous model was used to illustrate the charge storage mechanism. Under various stress voltages, it was discovered that the value of $\Delta C/C_0$ was less by only 1.0% for a lifetime of 10-years. Due to their strong ductility, thin BSA films exhibit high flexibility when repeatedly bent at various radii. The characteristics seen in these protein based MIM structures may be used in the manufacturing of cutting-edge, bio-inspired VLSI circuits. To investigate BSA's potential use as a UV photoactive material, a device with flexible

trace-on paper as the substrate and pencil-drawn interdigitated graphite electrodes were fabricated. A photoresponsivity of 10^{-3} A/W was observed at 232 nm wavelength.

A transparent, organic, papain based MIM capacitor has been fabricated using ITO as the top and bottom electrodes. Although α-helical groups are discovered to be the main component, papain is found to be a mixture of α-helical, β-sheet, 'Turn', etc. We reported negative VCC-α also for papain and a very high dielectric constant of 300.4. It was seen that the dissipation factor was remarkably high, which may have been caused by poor contact adhesion and dielectric defects. Analytical modeling is used to estimate the number of dipoles and their permanent dipole moment. The charge storage process has similarities to the Grotthuss transfer-explained ionic double layer model observed in inorganic MIM capacitors. Resistive switching devices were also fabricated with papain using different top electrodes. In both the HRS and LRS modes, bipolar resistive switching events have been clearly seen to be stable. The redox process that creates and destroys the conducting filaments in the thick papain film as well as the presence of thin AlO_x layer are thought to be the causes of the resistive switching in papain. Multiple current conduction methods were also noted in the device. Papain's bipolar resistive switching nature may be used in bio-inspired memory circuit applications in future.

Transient electronics can result in environmental compatibility with the ecosystem from the perspective of electronic waste disposal. Using gelatin made from fish scales (*Labeo Rohita sp.*), we successfully created a biodegradable, transient, transparent electrical substrate using the solution casting method at room temperature. The produced substrate displayed high transparency (90% transmittance), a low surface roughness of 1.91 nm, and good morphological characteristics. The bio-polymer substrate (BPS) demonstrated enough mechanical strength to be employed as an electronic device substrate. Additionally, reusable electronics have an advantage due to the substrate's renewability. The Al/BSA/Pt/BPS organic capacitor demonstrated electrical properties that were comparable to those of the previously reported MIM structures, demonstrating the viability of the substrate as a device. This study

investigates a waste product utilized to create a viable substrate for electronic devices, which helps manage aquatic waste materials and adds value to aquatic resources. Commercially accessible ITO-coated glass substrates may be replaced by metal-coated BPS. The substrate's flexural strength of 8.33 MPa and tensile strength of 4 MPa indicate that it is reasonably brittle.

7.2 Suggestions for Future Work

For 'Proteotronic' gadgets to replace their inorganic equivalents, more research is needed to ensure their incomprehensibility in today's electronic world. To create very transparent device architectures, ITO can be deposited as the top electrode contact. It is also difficult to further minimize the distance between the IDE electrodes' fingers by using alternate methods without increasing the device's dissipation factor. Reducing spin speed can further reduce the thickness of the protein layer, but doing so may accentuate film defects. The layer-by-layer protein-deposition process might increase the capacitance density and make it suitable for radio-frequency device applications, but there is a challenge in further reducing the roughness and thickness of active layers without raising the dissipation factor. Future flexibility tests utilizing the repetitive bending approach will be necessary to investigate the device's mechanical stability and its effects on its electrical properties. Therefore, it is necessary to tailor the material's mechanical characteristics so that it can be employed as a viable material for flexible electronics in the future. There is a trade-off between the device's performance and its transience, so it's important to find the right balance. As, because transient materials are hydrophilic and susceptible to water dissolution, special care must be taken during the production process.

However, there are still a number of significant issues that need to be resolved, including the reproducible processing of these nanomaterials in proteotronic devices, controlling the formation of nanostructures on substrates, understanding the connection between the morphology and electrical characteristics of protein nanostructures, and boosting productivity for long-term viability in ionic and biological media.

List of Publications

Patents

- L Vandana A Dash, U Dey, S Mahata, **S Guhathakurata**, S Mallik, G Ahmad, C S Kumar, C Jachob "METHOD FOR PRODUCTION OF TEXTURED FLEXIBLE SOLAR CELLS AND SOLAR CELLS ATTAINED THEREOF", Application no: 202331013288, International Patent Classification: awaiting, The Patent Office Journal, (2023).

- S Mallik, R. Roy, G Ahmad, A Raja, S. H Raheman, Ajit Dash, P. Panigrahi, P. K. Singh, **S. Guhathakurata**, N. B. Manik, P. Das and S. S Mahato, "AN AUTOMATED PROBING SYSTEM FOR MEASURING ELECTRICAL CHARACTERISTICS OF ON-WAFER DEVICES ANDA METHOD THEREOF"; Application No. 202031041107, International Patent Classification H01L 33/00, The Patent Office Journal, 42 (2020), 53611.

Peer Reviewed Journals

- **S. Guhathakurata**, S. Mallik, M. K. Hota, A. Bag, C. Mukherjee, N. B. Manik and C. K. Maiti, "Electroforming Free Bipolar Resistive Switching Characteristics Observed in Plant Protein Papain". (communicated)

- **S. Guhathakurata**, D.Pal, B Sambi Reddy, N. B. Manik, S. Mallik, "Fabrication of Highly Transparent Substrate from Waste Material for Green Electronics", under review in ACS Applied Electronic Materials.

- P. Kumar*, **S. Guhathakurata***, A. Choudhury, A. Sharma, A. R.Tripathy, S. S. Kumar, P. P. Pancham, P. Das, S.S.Mahato, S.Mahata, S. Mallik, "Flexible BSA MIM Capacitor with Negative Voltage Coefficient for RF Applications"Appl. Phys. Lett. 116, 171904 (2020); [Q1, SCI, impact Factor: 3.52, https://doi.org/10.1063/1.5139494] (*equal contribution)

- S. Mohanty, A. Arya, D. Jena, **S. Guhathakurata**, N. B. Manik, G. Ahmad and S. Mallik, "Potential Soluble Substrates for Transient Electronics

Applications: A Review", AIP Avdavces, Vol. 12, p. 050701, 2022, [Q2, SCIE, impact factor: 1.53, doi: 10.1063/5.0066174].

- S. Mohanty, D. Panda, A. Dash, S. S. Kumar, R. R. Padhi, **S. Guhathakurata** and S. Mallik, "A Review on Borophene: A Potential 2D Adsorbent Material for Gas Sensing Applications", *Journal of Electronic Materials*. Vol. 14, p.33403, 2023 [Q2, SCIE, impact factor: 1.9, doi: 10.1007/s11467-019-0884-5].

- D. Deo, S. P. Singh, S. Mohanty, **S. Guhathakurata**, D. Pal and S. Mallik, "Biomimicking of Phyto-based Superhydrophobic Surfaces towards Prospective Applications: A Review", *J Mater Sci Vol.* 57, p.8569, 2022 [Q1, SCIE, impact factor: 4.2, doi: 10.1007/s10853-022-07172-1].

- P. Maiti, Ajit Dash, **S. Guhathakurata**, S Das, A. Bag, T P Dash, G. Ahmed, C. K. Maiti and S. Mallik, "Experimental and Simulation Study of Charge Transport Mechanism in HfTiOx High-k Gate Dielectric on SiGe Heterolayers", Bull. Mat. Res Vol. 45, p. 1, 2022, [Q3, SCIE, impact factor: 1.7, doi: 10.1007/s12034-021-02622-z,].

Book Chapters

- **S Guhathakurata**, N B Manik, S Mohanty, D Jena, S Satapathy, D Panda, A Dash, R Mahato, G Ahmad, P K Singh, S Mallik, "Charge Storage Mechanism in Proteotronic Capacitors", chapter published in "Cutting-Edge Research on Low-Dimensional Nanoelectronic Devices: Physics and Material Science Aspects" by Apple Academic Press, 2020 [ISBN: 9781774638668] Pub Date: January 2022.

- G Ahmad, **S. Guhathakurata**, S. Mohanty, P. Singh, S Mallik, "Thin-film Photovoltaic Devices with Asymmetric Heterocontact Geometries" chapter published in "Cutting-Edge Research on Low-Dimensional Nanoelectronic Devices: Physics and Material Science Aspects" by Apple Academic Press, 2020 [ISBN: 9781774638668] Pub Date: January 2022.

- S. Mallik, P. Singh, G. Ahmad, **S. Guhathakurata**, S. S. Mahato and N. B. Manik, "High Sensitive Terahertz Biosensors" chapter published in "Advanced Materials for Future Terahertz Devices, Circuits and Systems" by Springer, ISBN 978-981-334-488-4 (due on February 16, 2020).

Conferences Proceedings

- **S. Guhathakurata**, N. B. Manik, and S. Mallik, "A biodegradable transparent substrate from waste materials towards flexible and transient electronics applications", International Conference on Advancements in Smart Electronics, Materials and Communication Technologies (ICASEMCT), SKIT Jaipur, 2023., [ISBN no. 978-81-954233-1-6].

- **S. Guhathakurata**, N. B. Manik, S. Mallik, "Electrical Performance of Protein-based Flexible MIM Structure Fabricated at Room Temperature for Proteotronic Applications", Proceedings in XXI International Workshop on Physics of Semiconductor Devices (IWPSD), IIT Delhi, 2021.

- S. Mallik, **S. Guhathakurata**, S. S.Mahato, S. S. Kumar, P. P.Pancham, S. Panda, A.Bebarta, S.K.Sahu, A. Bag, and M.Palit, "Dependency of Pore Formation on Mechanical Structure for Different Forms of Aluminum", International Seminar Cum Research Colloquium on MEMS based Sensors and Smart Nanostructured Devices (MSSND), Jadavpur University, Kolkata, 2019.